CHARACTERIZATION OF THE STRESS AND REFRACTIVE-INDEX DISTRIBUTIONS IN OPTICAL FIBERS AND FIBER-BASED DEVICES

A Thesis
Presented to
The Academic Faculty

by

Michael R. Hutsel

In Partial Fulfillment
of the Requirements for the Degree
Doctor of Philosophy in the
School of Electrical and Computer Engineering

Georgia Institute of Technology
December 2011

CHARACTERIZATION OF THE STRESS AND REFRACTIVE-INDEX DISTRIBUTIONS IN OPTICAL FIBERS AND FIBER-BASED DEVICES

Approved by:

Professor Thomas K. Gaylord,
Advisor, Committee Chair
School of Electrical and Computer Engineering
Georgia Institute of Technology

Professor Linda S. Milor
School of Electrical and Computer Engineering
Georgia Institute of Technology

Professor John A. Buck
School of Electrical and Computer Engineering
Georgia Institute of Technology

Dr. Michael E. Knotts
Signature Technology Laboratory
Georgia Tech Research Institute

Dr. Donald D. Davis
School of Electrical and Computer Engineering
Georgia Institute of Technology

Date Approved: 3 November 2011

ACKNOWLEDGEMENTS

Trust in the Lord with all your heart,
and do not lean on your own understanding.
In all your ways acknowledge him,
and he will make straight your paths.
– Proverbs 3:5-6 (ESV)

I thank God for His grace, His unmerited kindness, that He's shown me throughout my life and especially during my time at Georgia Tech. This is especially evident in the loving and supportive family, friends, and colleagues that He's brought into my life and allowed me to work alongside.

My wife, Laura, made the completion of this degree possible with her unconditional love demonstrated daily with encouraging words and in special ways like bringing a homemade dinner to the office on nights I worked late. Her daily support never declined, though she worked full time as a dedicated speech-language pathologist and most recently as a full-time, wonderful mother of our daughter, Katherine. Her commitment to me and to our family is my greatest motivation.

My parents, Ross and Pat, enabled me to pursue and complete this degree in more ways than I'll ever know. Early in my life they fostered my engineering interests by allowing my brother, Brian, and me to dump gallons of Lego pieces across the living room floor and spend all day constructing whatever we could imagine. As I grew older, they continued to support my sometimes questionable technical pursuits like removing all of the seats, interior panels, consoles, and carpeting from my car to run wires to speakers that occupied nearly the entire trunk.

It has been a privilege to have Dr. Tom Gaylord as an advisor. The work reported in this thesis is a direct result of his constant positive attitude and support at the deepest technical level. He is an example of a great leader in the Optics Lab, a thoughtful and thorough researcher, and a considerate gentleman.

My committee members, Dr. John Buck, Dr. Don Davis, Dr. Linda Milor, and Dr. Michael Knotts helped me to refine this work and this thesis to a level that I could not achieve on my own. I am grateful for the interest they showed in this work and the time they took to discuss it in great detail.

I am grateful for the students in the Optics Lab with whom I've been able to collaborate. My work is only a building block on top of the excellent work performed by Dr. Brent Bachim and Dr. Carole Montarou. Dr. Justin Stay, Jon Maikisch, Dr. Chien-I Lin, Matt Burrow, Matthieu Leibovici, and Micah Jenkins sacrificed great amounts of time and effort to work through difficult concepts, troubleshoot lab equipment and procedures, and help refine my writing and presentations in great detail. Gatherings of the Optics All Stars helped me remain balanced; Optics Lab cook-offs kept me well fed.

I am also grateful for the assistance of Louis Boulanger in the machine shop and Rajib Acharya for computer support. The measurement apparatus developed as part of this work would not have been possible without Mr. Boulanger's excellent, careful work and Mr. Acharya's ability to solve the most obscure problems.

I thank God for all of these family, friends, and colleagues and for many others that I have not acknowledged here. He has set straight my path, drawing me closer to Himself, through all of you. For that I am eternally thankful.

Michael R. Hutsel

Georgia Institute of Technology

November 2011

TABLE OF CONTENTS

LIST OF TABLES

LIST OF FIGURES

LIST OF ABBREVIATIONS

AFM Atomic Force Microscopy

BKC Brace-Köhler Compensator

CO_2 Carbon Dioxide

DIC Differential Interference Contrast

FBG Fiber Bragg Grating

FOV Field of View

FTIR Fourier Transform Infrared (Spectroscopy)

FWHM Full Width at Half Maximum

LPFG Long-Period Fiber Grating

MIOPT Microinterferometric Optical Phase Tomography

NA Numerical Aperture

PMD Polarization-Mode Dispersion

PSI Phase-Shifting Interferometry

QPM Quantitative-Phase Microscopy

QWP Quarter-Wave Plate

RID Refractive-Index Distribution

RIP Refractive-Index Profile

RMS Root Mean Squared

RSD Residual-Stress Distribution

SPR Surface Plasmon Resonance

TIE Transport of Intensity Equation

TWC Two-Waveplate Compensator

UV Ultraviolet

WDM Wavelength-Division Multiplexing

SUMMARY

Optical fiber technology continues to advance rapidly as a result of the increasing demands on communication systems and the expanding use of fiber-based sensing. New optical fiber types and fiber-based communications components are required to permit higher data rates, an increased number of channels, and more flexible installation requirements. Fiber-based sensors are continually being developed for a broad range of sensing applications, including environmental, medical, structural, industrial, and military.

As optical fibers and fiber-based devices continue to advance, the need to understand their fundamental physical properties increases. The residual-stress distribution (RSD) and the refractive-index distribution (RID) play fundamental roles in the operation and performance of optical fibers. Custom RIDs are used to tailor the transmission properties of fibers used for long-distance transmission and to enable fiber-based devices such as long-period fiber gratings (LPFGs). The introduction and modification of RSDs enable specialty fibers, such as polarization-maintaining fiber, and contribute to the operation of fiber-based devices. Furthermore, the RSD and the RID are inherently linked through the photoelastic effect. Therefore, both the RSD and the RID need to be characterized because these fundamental properties are coupled and affect the fabrication, operation, and performance of fibers and fiber-based devices.

To characterize effectively the physical properties of optical fibers, the RSD and the RID must be measured without perturbing or destroying the optical fiber. Furthermore, the techniques used must not be limited in detecting small variations and asymmetries in all directions through the fiber. Finally, the RSD and the RID must

be characterized concurrently without moving the fiber to enable the analysis of the relationship between the RSD and the RID. Although many techniques exist for characterizing the residual stress and the refractive index in optical fibers, there is no existing methodology that meets all of these requirements. Therefore, the primary objective of the research presented in this thesis was to provide a methodology that is capable of characterizing concurrently the three-dimensional RSD and RID in optical fibers and fiber-based devices. This research represents a detailed study of the requirements for characterizing optical fibers and how these requirements are met through appropriate data analysis and experimental apparatus design and implementation.

To validate the developed methodology, the secondary objective of this research was to characterize both unperturbed and modified optical fibers. The RSD and the RID were measured in a standard telecommunications-grade optical fiber, Corning SMF-28. The effects of cleaving this fiber were also analyzed and the longitudinal variations that result from cleaving were explored for the first time. The fabrication of carbon-dioxide-laser-induced (CO_2-laser-induced) LPFGs was also examined. These devices provide many of the functionalities required for fiber-based communications components as well as fiber-based sensors, and they offer relaxed fabrication requirements when compared to LPFGs fabricated by other methods.

The developed methodology was used to perform the first measurements of the changes that occur in the RSD and the RID during LPFG fabrication. The analysis of these measurements ties together many of the existing theories of CO_2-laser-induced LPFG fabrication to present a more coherent understanding of the processes that occur. In addition, new evidence provides detailed information on the functional form of the RSD and the RID in LPFGs. This information is crucial for the modeling of LPFG behavior, for the design of LPFGs for specific applications, for the tailoring of fabrication parameters to meet design requirements, and for understanding the limitations of LPFG fabrication in commercial optical fibers. Future areas of research

concerning the improvement of the developed methodology, the need to characterize other fibers and fiber-based devices, and the characterization of CO_2-laser-induced LPFGs are identified and discussed.

CHAPTER 1

INTRODUCTION

This introductory chapter provides a review of the motivation, background, and existing techniques for the characterization of the residual-stress distribution (RSD) and the refractive-index distribution (RID) in optical fibers and fiber-based devices. Also discussed is the characterization of carbon-dioxide-laser-induced long-period fiber gratings (CO_2-laser-induced LPFGs). Although much of this thesis is devoted to the RSD and RID in these devices, the characterization techniques developed are widely applicable and capable of measuring these fundamental properties in other fibers and fiber-based devices.

1.1 Motivation

Optical fiber technology continues to advance rapidly as a result of the increasing demands on communication systems and the expanding use of fiber-based sensing. New optical fiber types to control loss, dispersion, and non-linear effects are required to permit higher data rates, an increased number of channels in wavelength-division multiplexing (WDM) systems, and more flexible installation requirements to bring optical signals closer to the end user [1, 2]. Fiber-based communication components enable crucial signal manipulation capabilities, including coupling, filtering, and amplification [3]. Fiber-based sensors are continually being developed for a broad range of sensing applications, including environmental, medical, structural, industrial, and military. Sensors that use the intrinsic properties of the fiber as a sensing mechanism, referred to as intrinsic fiber-based sensors, possess the inherent advantages of optical fibers. They are small in size, immune to electromagnetic interference, resistant to many hazardous chemicals, and capable of remote monitoring. Furthermore, fibers

are readily available because of the vast extent of the telecommunications industry.

The characterization of the properties of fibers and fiber-based devices is crucial for their design, fabrication, and deployment. The properties can be split into two broad categories: transmission properties and physical properties. The transmission properties, such as loss, gain, spectral response, dispersion, polarization-mode dispersion, and intensity distribution, are important for determining light-guiding and signal-propagation behaviors. The physical properties, such as size, RID, and RSD, are important for modeling, design, and evaluation.

Techniques for the measurement of transmission properties have been developed thoroughly and the equipment required to perform the measurements is readily available. However, techniques and equipment for the measurement of physical properties remain limited in their use and availability. As a consequence, new fibers and fiber-based devices are characterized primarily by their transmission properties. Although these properties determine the applicability of fibers and fiber-based devices, they provide little insight into the underlying physical properties that determine their operation and performance.

As optical fibers and fiber-based devices continue to advance, the need to understand their fundamental physical properties simultaneously increases. An understanding of their transmission properties alone is no longer sufficient for the design and optimization of emerging novel fiber types, communication components, and fiber-based sensors. Fiber and fiber-based device development must include a complete understanding of their physical properties to move beyond the limited capability of exclusively demonstrating their signal and sensing behaviors to modeling and optimizing their designs for specific applications.

To characterize effectively the physical properties of optical fibers, the RSD and the RID must be measured without perturbing or destroying the optical fiber. Furthermore, the techniques used must be capable of detecting small variations and

asymmetries in all directions through the fiber. Finally, the RSD and the RID must be characterized concurrently without moving the fiber between separate pieces of equipment to enable the establishment of the relationship between the RSD and the RID. Although many techniques exist for characterizing the residual stress and the refractive index in optical fibers, there is no existing methodology that meets all of these requirements.

These requirements must be met to provide a more complete understanding of the physical properties of optical fibers and fiber-based devices. Therefore, the primary objective of the research presented in this thesis is to provide a methodology that is capable of characterizing concurrently the three-dimensional RSD and RID in optical fibers and fiber-based devices. To validate the developed methodology, the secondary objective of this research is to characterize both unperturbed and modified optical fibers, including CO_2-laser-induced LPFGs. These devices provide many of the functionalities required for fiber-based communications components as well as fiber-based sensors, and they offer relaxed fabrication requirements when compared to LPFGs fabricated by other methods.

To better understand what is required to achieve these objectives, the origins and effects of residual stresses and RIDs in optical fibers are discussed in Sec. 1.2 and the existing characterization techniques are discussed in Sec. 1.3. An overview of the unique features, advantages, and potential applications of CO_2-laser-induced LPFGs is presented in Sec. 1.4. The existing efforts to characterize these devices is also briefly reviewed. The objectives of this research are discussed in more detail and the accomplishments are outlined in Sec. 1.5. Finally, an overview of this thesis is presented in Sec. 1.6.

1.2 Background

1.2.1 Residual Stress in Optical Fibers

Stresses are induced in optical fibers during manufacturing because of variations in two properties of the glass: the coefficient of thermal expansion and the viscosity [4]. The stresses that are induced by differences in the coefficient of thermal expansion are typically referred to as thermally induced stresses. The stresses that are induced by differences in the viscosity are typically referred to as draw-induced or mechanically induced stresses. In combination, these stresses are referred to as frozen-in or residual stresses. These residual stresses remain in the fiber after it is drawn (manufactured) and without the presence of externally applied forces [5].

Residual stresses are known to affect both the transmission properties and the physical properties of optical fibers [5–8]. The presence of residual stresses can be detrimental in many applications. However, the careful addition or modification of residual stresses can enable numerous new applications. The presence of residual tensile stresses near the surface of an optical fiber can lead to cracking and a decreased lifetime [9, 10]. Crack formation can be reduced, however, if compressive stresses are frozen in near the surface of the fiber [11]. Stress-induced birefringence in optical fibers is detrimental to systems that require low polarization sensitivity [12] or low polarization-mode dispersion [13–16]. However, residual stresses are necessary to create the high birefringence required for certain types of polarization-maintaining fibers [13, 17]. The relaxation of residual stresses that results from cleaving a fiber can cause unexpected changes in performance [18].

The controlled modification of residual stresses enables the fabrication of several types of fiber-based devices. Changes in the RSD in various fiber types have been observed in fiber Bragg gratings (FBGs) [19–21] and LPFGs [22–26] fabricated by various techniques. RSD modification is also hypothesized to contribute to the RID changes necessary for beam expansion in high-power connectors [27].

1.2.2 Refractive-Index Distribution in Optical Fibers

The RID in an optical fiber or fiber-based device is fundamental in determining its transmission properties. In fibers with azimuthally symmetric RIDs, the step-index profile provides the simplest design. However, graded-index designs are necessary to minimize the differential group delay in multimode fibers. In single-mode fibers, graded-index, multi-step, triangular-core, and trapezoidal-core designs are used to minimize loss, control mode-field distributions, and control dispersion [13]. New fiber types with larger mode-field areas allow for increased input powers while maintaining sufficiently low intensities to avoid nonlinear effects [1]. RIDs with low-index trenches in the cladding greatly reduce bending losses to permit relaxed installation requirements for applications such as fiber-to-the-home [2]. Azimuthally asymmetric RIDs, such as elliptical-core designs, are used to make polarization-maintaining fibers.

The RID is also important in fiber-based communication components and sensors. The custom design of RIDs can provide gain-flattened, broadband Raman amplifiers without the need for multiple pumps [28]. The azimuthally asymmetric perturbations to the RID in CO_2-laser-induced LPFGs enable wavelength tuning and attenuation tuning by varying the bend radius and the azimuthal orientation of the bend direction [29–32]. Asymmetric perturbations also allow for directional bend- and load-sensing behaviors [33, 34].

1.3 Existing Characterization Techniques

1.3.1 Residual-Stress Characterization

The photoelastic effect enables the nondestructive characterization of the residual stresses present in optical fibers. The residual stresses create stress-induced birefringence in the fiber. The retardation induced in a beam of polarized light propagating through the birefringent fiber can be determined using photoelastic measurement techniques. Illumination of the fiber normal to the longitudinal axis, or transverse

illumination, eliminates the need to cut, polish, or otherwise perturb the fiber. Therefore, the RSD in the fiber can be determined nondestructively by using transverse illumination and measuring the retardation.

In a fiber with an azimuthally symmetric RSD, a single radial profile characterizes fully the RSD. In this case, a measurement of the radial variation of the retardation permits the calculation of the radial variation in the stress via the inverse Abel transform [35]. For fibers with azimuthally asymmetric RSDs, a cross-sectional distribution is required to characterize the RSD. Computed tomography principles enable the determination of cross-sectional RSDs from a sequence of retardation measurements made over various rotational angles of the fiber [36]. For both symmetric and asymmetric fibers, the retardation measurement must be suitably accurate to determine the RSD with sufficient accuracy and resolution. The techniques that exist for measuring the retardation produced by the birefringence in optical fibers are discussed in the remainder of this section.

1.3.1.1 Photoelasticity Techniques

Several techniques use photoelasticity to determine the retardation produced by the birefringence in optical fibers. Polarization-digital-holographic microscopy enables the determination of the retardation from a single intensity pattern produced by the interference of two reference beams and a beam passing through the optical fiber [37]. This technique, however, requires several beamsplitting prisms, waveplates, and polarizers to control the directions and the polarizations of the three beams of light. Phase-stepping or phase-shifting photoelasticity enables the determination of the retardation from several intensity patterns recorded for predetermined orientations of waveplates and polarizers in the beam path [38, 39]. This technique requires only one beam path, but can require multiple waveplates to generate a sufficient number of intensity patterns. Phase modulation techniques enable the determination of

the retardation from several intensity patterns recorded as the orientation of a well-calibrated phase modulator is changed sequentially [40]. This requires the use of a custom phase modulator rather than commercially available waveplates. Furthermore, all these techniques rely on the measurement of relative-intensity distributions, which is generally not as accurate as detecting a minimum or a null of intensity.

1.3.1.2 Compensator Techniques

To avoid the need to measure relative intensities, phase compensation techniques are often used to enable the detection of minima or nulls of intensity. Chu and Whitbread reported on the first phase compensation technique for the characterization of fibers [35]. They described the use of a polariscope and the Sénarmont compensator technique. A polariscope requires a single beam path, a waveplate, and two polarizers. The fiber is placed at 45 deg from extinction between crossed polarizers and is imaged by a camera. A quarter-wave plate (QWP) is placed after the fiber and is oriented at extinction. In this configuration, the incident, linearly polarized light is converted to elliptically polarized light by the fiber and then back to linearly polarized light by the QWP. The second polarizer, typically referred to as the analyzer, is then rotated until it blocks the linearly polarized light from the QWP, resulting in a null in the transmitted intensity observed by the camera. The retardation induced by the fiber is determined point-by-point throughout the field of view (FOV) from the angular orientation of the analyzer that produces the null of intensity.

Several improvements to this technique have been made to increase the accuracy of the polariscope. Raine *et al.* introduced a diffuser following the He-Ne laser source to avoid interference effects from the diffraction of the coherent laser light [41]. Park *et al.* enabled higher accuracy with a high-magnification imaging system by rearranging the optical components [42, 43]. The previous arrangements of the polariscope placed the fixed polarizer before the fiber and the QWP and analyzer after the fiber.

To avoid wavefront distortions at the QWP resulting from the high-magnification imaging optics, Park *et al.* reversed the placement of the polariscope components, placing the QWP before the imaging optics.

Despite these improvements, it was shown recently that the Sénarmont compensator technique is generally not suitable to measure the low retardations produced by typical optical fibers [44,45]. Reported measurements made with visible light sources on silica-based fibers indicate that they produce wavelength retardations of the order of several nanometers [14,35,42,45,46]. In a study of several compensator techniques by Montarou *et al.*, waveplates were combined to produce known retardations similar to the small values produced by optical fibers [45]. With a visible source wavelength of 632.8 nm and a sample retardation of 3.09 nm, the average error of 30 Sénarmont measurements was 34.6%. For a sample retardation of 1.04 nm, the average error of 20 Sénarmont measurements increased to 48.1%. A more accurate technique is needed to permit the use of phase compensation for the characterization of the RSD present in optical fibers.

Recently, the two-waveplate compensator (TWC) technique was developed to meet the need to measure accurately the small retardations induced by optical fibers [45, 46]. This technique, like the Sénarmont technique, uses a polariscope arrangement. However, the waveplate used is a mica waveplate with a low retardation, typically $\lambda/10$ or $\lambda/30$. In this configuration, the mica waveplate must be rotated to achieve the conversion of the elliptically polarized light emerging from the fiber into linearly polarized light. The retardation induced by the fiber is determined point-by-point throughout the FOV from the angular orientation of the waveplate.

The determination the waveplate orientation that results in a linearly polarized output requires the rotation of the analyzer until the combination of the waveplate and the analyzer orientations is achieved that results in a null in the transmitted intensity. This technique has been shown to be theoretically and experimentally more

accurate than the Sénarmont technique for the measurement of small retardations [45]. However, the increase in accuracy requires an increase in the measurement duration. The rotation of both the compensator and the analyzer requires more time than the rotation of only the compensator. This problem is multiplied when a sequence of retardation measurements must be taken over various rotational angles of the fiber for the characterization of cross-sectional RSDs.

Also investigated for the accurate measurement of small retardations was the Brace-Köhler compensator (BKC) technique [45]. This technique uses the same low-retardation mica waveplate as the TWC technique, but uses the rotation of only the compensator. The compensator is rotated to produce an output polarization with a minimized component along the transmission direction of the analyzer. This results in a minimum in the transmitted intensity. With this configuration, the retardation induced by the fiber can be determined point-by-point throughout the FOV from the angular orientation of the compensator. A small-retardation approximation is typically used to simplify the determination of the retardation induced by the fiber [47]. However, an exact expression for the determination of the retardation can also be derived [44].

Compared with the TWC technique, the BKC technique is theoretically less accurate because of the detection of a minimum in the transmitted intensity rather than a null. However, in the study of several compensator techniques by Montarou *et al.*, the BKC technique performed better than the TWC technique for the sample with a retardation of 3.09 nm, and it had an error that was less than 1% higher for the sample with a retardation of 1.04 nm [45]. Additionally, the accuracy of these techniques has also been investigated for performing full-field measurements in which the spatially varying retardation of a sample is determined throughout the entire FOV of the measurement apparatus [48]. The full-field accuracy of each technique was determined by measuring the retardation of a commercially available mica waveplate.

An Olympus compensator model U-CBR1 ($\lambda/10$ mica waveplate) was used as the rotating compensator to measure the retardation of an Olympus compensator model U-CBR2 ($\lambda/30$ mica waveplate). The retardations of these waveplates as given by the manufacturer are 59.66 nm and 21.54 nm respectively at a wavelength of 546 nm. A summary of the error in the full-field measurements of the U-CBR2 waveplate retardation is shown in Table 1.1. The error was determined by comparing the measured retardation to the manufacturer-specified retardation. The BKC technique proves to be slightly more accurate than the TWC. The BKC technique achieves an error of less than 2% over 98.53% of the FOV compared with 58.47% of the FOV for the TWC technique. The BKC technique therefore permits (1) the measurement of small retardations with an accuracy similar to the TWC technique and (2) reduces the measurement duration by requiring the rotation of only the compensator.

Table 1.1: Error analysis of TWC and BKC full-field retardation measurements [48].

Error (%)	Percent of FOV with specified error	
	Two-waveplate compensator	Brace-Köhler compensator
≤ 5	99.69	99.75
≤ 4	99.56	99.69
≤ 3	94.33	99.67
≤ 2	58.47	98.53
≤ 1	6.86	53.01

1.3.1.3 Summary

The techniques available for the nondestructive characterization of the RSD in optical fibers are listed in Table 1.2, along with the requirements for the accurate characterization of cross-sectional RSDs. The available photoelasticity techniques require the measurement of relative intensity distributions. This is generally not as accurate as

the measurement of minima or nulls of intensity provided by the compensator techniques. While the Sénarmont compensator technique enables the measurement of nulls of intensity, it has been shown to be unsuitable for the measurement of the low retardations (on the order of $\lambda/100$) produced by typical optical fibers [44, 45]. The TWC technique and the BKC technique have been shown to provide the accuracy required to measure the small retardations produced by optical fibers, but only the BKC technique provides a workable measurement duration for the characterization of cross-sectional RSDs. The BKC technique also uses a standard microscope-based configuration, which is crucial for the integration of an RID characterization technique.

Table 1.2: Optical fiber cross-sectional residual-stress distribution measurement techniques.

Measurement Technique [example reference]	Requirements			
	Minimum-Intensity-Based Measurement	Accurate for Small Retardations	Workable Measurement Duration	Standard Microscope-Based Configuration
Polarization digital holographic microscopy [37]	No	No	Yes	No
Phase-stepping photoelasticity [38]	No	No	Yes	No
Phase modulation [40]	No	No	Yes	No
Sénarmont compensator [35]	Yes	No	Yes	Yes
Two-waveplate compensator [45]	Yes	Yes	No	Yes
Brace-Köhler compensator [45]	Yes	Yes	Yes	Yes

1.3.2 Refractive-Index Characterization

Many techniques have been developed for the characterization of the RID in optical fibers. The techniques can be divided into two broad categories: axial and transverse.

Axial techniques require access to the end-face of the optical fiber and operate in some manner parallel, or nearly parallel, to the longitudinal axis of the fiber. For suitable techniques, this enables the direct measurement of a cross section of the RID. Furthermore, the interaction of the light with a planar end-face makes for straightforward illumination and observation. However, the cleaving and the polishing necessary to prepare the end-face make the axial techniques inherently destructive. Cleaving and polishing also modify the properties of the fiber and prohibit the characterization of unperturbed fibers and fiber-based devices.

Transverse techniques operate by observing light that travels perpendicular to the longitudinal axis of the fiber. This allows for the non-destructive characterization of the fiber and a potentially high resolution in the axial direction. However, the light interaction with the cylindrical outer surface of the fiber is less straightforward than the planar end-face. The use of an index-matching oil is often required to minimize the refraction at the outer cladding surface. Furthermore, as with the characterization of RSDs, a sequence of measurements taken over various rotational angles of the fiber and computed tomography principles are required to characterize cross-sectional RIDs.

1.3.2.1 Axial Techniques

The refracted near-field technique uses light launched into the end-face at angles greater than the acceptance angle of the fiber. The radial profile of the RID is determined from measurements of the spatial distribution of the light refracted out of the fiber [49]. Refinements to this technique have led to the development of a commercial profiler (Photon Kinetics S14 Refractive-Index Profiler) and an apparatus for the measurement of azimuthally asymmetric cross-sectional RIDs [50]. However, calibration with several known samples is required to provide accurate values of the absolute refractive index. Furthermore, it must be assumed that there are no axial

variations in the RID near the end-face where the refraction occurs [49].

The reflection method enables the determination of a cross-sectional RID from a measurement of the reflectivity of the fiber end-face [51–53]. Because light is not refracted through the fiber, a high transverse spatial resolution is possible for the characterization of micro-structured fibers, such as photonic crystal fibers [53]. However, a high sensitivity is required to detect the variations in the weak reflections from a typical silica-based fiber. The weak reflections also make the technique very sensitive to dust or contamination on the end-face of the fiber.

Chemical etching combined with atomic force microscopy (AFM) has been demonstrated as a non-optical means of characterizing the cross-sectional RID in optical fibers [54, 55]. This technique is capable of the nanometer-scale spatial resolution of AFM, however, the refractive index must be determined from the etch depth and the etch rate of the etching chemical. This requires careful calibration with well-characterized samples and chemicals to enable quantitative refractive-index measurements.

Axial interferometry is one of several interferometric techniques. These techniques, four of which are classified as transverse techniques, use interference microscopy to determine the phase shift induced by the fiber. The phase shift is defined as the difference in the phase accumulated by the light transmitted through the fiber and the phase accumulated by the light transmitted through the medium surrounding the fiber. The relative RID, defined as the difference between the RID of the fiber and the refractive index of the surrounding medium, is then determined from the phase-shift measurement. The absolute RID of the fiber can be determined if the refractive index of the surrounding medium is known.

Axial interferometry uses a monochromatic source and a Mach-Zehnder interferometer [56, 57]. The interfering beams are aligned to intersect at an angle greater than zero to generate parallel interference fringes. The fiber sample, which must be

prepared as a thin disk of known thickness, is then inserted into one arm of the interferometer, resulting in a displacement of the interference fringes. The interference-fringe displacement is proportional to the phase shift induced by the fiber sample. The refractive index can be calculated from the phase shift and the sample thickness. This technique allows for the straightforward calculation of the cross-sectional RID, however, great care must be taken to prepare the sample. Any variations in the thickness must be characterized. Furthermore, a trade-off exists between the transverse spatial resolution of the RID and the accuracy and resolution of the fringe-displacement measurement. An increased fringe separation enhances the accuracy of determining the fringe displacements, and thus it enhances the accuracy of the determined RID. However, the transverse spatial resolution is decreased as adjacent fringes occupy larger areas of the sample.

1.3.2.2 Transverse Techniques

Transverse interferometry, like axial interferometry, uses the measurement of the displacement of interference fringes [58, 59]. The measurement apparatus is identical to the one used for axial interferometry, but the fiber sample is illuminated transversally. This avoids the need to prepare thin slices of the fiber, but limits the technique to the characterization of azimuthally symmetric RIDs. Furthermore, the cylindrical shape of the fiber requires the use of the inverse Abel transform to calculate the refractive-index profile (RIP) from the phase shift.

Microinterferometric optical phase tomography (MIOPT) was developed recently as an extension to transverse interferometry. MIOPT combines transverse interferometry and tomographic principles to determine the cross-sectional RID from a sequence of phase-shift measurements taken over various rotational angles of the fiber [60, 61]. This enables the characterization of fibers with azimuthally asymmetric RIDs. Like axial interferometry, MIOPT requires a trade-off between the spatial resolution and

the accuracy and resolution of the fringe-displacement measurements. With MIOPT, the interference fringes are aligned perpendicular to the longitudinal axis of the fiber. An increased fringe separation enhances the accuracy of determining the fringe displacements, but results in adjacent fringes occupying larger distances along the fiber axis. This limits the axial resolution of the technique. For fiber-based devices with rapid axial changes in the RID, MIOPT can only provide an average cross-sectional RID over the axial distance spanned by adjacent fringes.

Phase-shifting interferometry (PSI) has also been demonstrated as an interferometric technique to determine the RID in optical fibers [62]. This technique uses a monochromatic source, but unlike the previous interferometric techniques, the interfering beams are aligned to be collinear, resulting in a homogeneous FOV. When placed in the sample arm, the fiber creates a spatially varying intensity pattern. The phase shift induced by the fiber can be determined from four unique intensity patterns that are generated by producing four predetermined phase shifts in the reference beam. This technique eliminates the need to analyze fringe displacements and is therefore limited in axial resolution only by the imaging optics. However, four intensity patterns, rather than one fringe pattern, are required to determine the phase shift. Although not yet demonstrated on fibers, computed tomography principles can be used with this technique to determine azimuthally asymmetric RIDs from a sequence of phase-shift measurements taken over various rotational angles of the fiber.

A recently developed technique uses dispersive Fourier-transform spectroscopy to characterize the spectral dependence of the RID [63]. This technique uses a broadband source and a translating wedge to produce a variable phase shift in the reference beam of the interferometer. An interferogram is recorded for each observable point in the fiber by recording the intensity as the phase shift in the reference arm is varied continuously. The relative phase shift induced by the optical fiber can be determined from the phase of the Fourier transform of the interferograms [64]. Like PSI, this

technique uses collinear interfering beams to eliminate the need for fringe analysis and is therefore limited in axial resolution by only the imaging optics. However, because the interferograms are a function of the reference-arm phase shift, numerous measurements must be taken as the wedge is translated. As with MIOPT and PSI, computed tomography principles can be used with this technique to determine azimuthally asymmetric RIDs.

Quantitative-phase microscopy (QPM) is a non-interferometric technique that enables the determination of the phase shift produced by the fiber [65]. This technique uses a standard microscope-based configuration to obtain an in-focus image of the fiber and two slightly defocused images on either side of the in-focus position. The phase shift induced by fiber can be determined by (1) using the defocused images to estimate the derivative of the intensity in the beam-propagation direction (longitudinal intensity derivative) and then (2) solving numerically the transport of intensity equation (TIE) [66]. Computed tomography principles have been used with this technique to determine azimuthally asymmetric RIDs [67]. This technique is limited in axial resolution only by the imaging optics and permits the use of a standard microscope.

The QPM technique has also been used characterize residual stresses by measuring directly the phase retardation produced by an optical fiber [68, 69]. This requires a polarizer on the light source to characterize independently the phase shifts produced by the fast and slow indices of the fiber. However, the QPM technique requires the measurement of the relative-intensity distribution of the in-focus image and the two defocused images of the fiber. This is similar to the relative-intensity requirement for the non-compensator-based retardation measurements, and thus the measurement is not as accurate as detecting a minimum of intensity. It has been shown that this technique is limited to detecting retardations on the order of $\lambda/10$, which is an order of magnitude higher than the low retardations (on the order of $\lambda/100$) produced by

typical optical fibers [69].

1.3.2.3 Summary

The techniques available for the characterization of the cross-sectional RIDs in optical fibers are listed in Table 1.3, along with the requirements for the techniques to be applicable to fibers and fiber-based devices. The axial techniques are inherently destructive because they require cleaving and polishing to prepare the end-face of the fiber. The interferometric techniques require the use of an interferometer and cannot be carried out on the same equipment as the RSD characterization techniques. QPM provides a technique capable of characterizing cross-sectional RIDs without perturbing the fiber or fiber-based device. QPM can also be performed on the same equipment as the RSD characterization techniques because it uses a standard microscope-based configuration. This enables the simultaneous characterization of the RSD and the RID with one measurement apparatus.

Table 1.3: Optical fiber cross-sectional refractive-index distribution measurement techniques.

Measurement Technique [example reference]	Requirements		
	Non-Destructive	High Axial Spatial Resolution	Standard Microscope-Based Configuration
Refracted near-field [49]	No	No	No
Reflection [51]	No	No	Yes
Etching and AFM [54]	No	No	No
Axial interferometry [56]	No	No	No
MIOPT [60]	Yes	No	No
Phase-shifting interferometry [62]	Yes	Yes	No
Fourier-transform spectroscopy [63]	Yes	Yes	No
Quantitative-phase microscopy [65]	Yes	Yes	Yes

1.4 CO_2-Laser-Induced LPFGs

The need to develop a more complete understanding of the physical properties of fiber-based devices is highlighted in the development of fiber gratings. Fiber gratings enable many important fiber-based devices for communications and sensing. FBGs and LPFGs consist of a periodic perturbation to the RID of the fiber. FBGs have a periodic spacing on the order of hundreds of nanometers and couple forward-propagating, core-guided modes into backward-propagating, core-guided modes. LPFGs have a much longer periodic spacing, on the order of hundreds of micrometers, and couple forward-propagating, core-guided modes into forward-propagating, cladding-guided modes.

LPFGs eliminate the production of reflected light and provide the ability to manipulate transmitted light. These characteristics enable the development of in-line, LPFG-based components for communications. In addition, the coupling of light into and out of the cladding allows for the coupling of light between LPFGs in separate fibers. LPFGs have been used for band-pass filtering, gain equalization, dispersion compensation, power monitoring, and wavelength-selective coupling [70–74]. The response of LPFGs to the manipulation of the grating and to changes in the medium surrounding the fiber enable the development of intrinsic fiber-based sensors for numerous applications [75].

The periodic perturbation to the RID that is necessary to form an LPFG is typically produced by exposing a photosensitive fiber to ultraviolet (UV) laser light [70]. The fabrication of LPFGs has also been demonstrated by exposing the fiber to carbon-dioxide (CO_2) laser light [76]. This method enables the inexpensive fabrication of LPFGs in standard optical-network fibers using readily available CO_2 lasers. Furthermore, CO_2-laser-induced LPFGs are permanent and stable at very high temperatures [77].

1.4.1 Potential Applications

Sensing applications and tunable versions of the communication components listed previously have been demonstrated [30–33, 78]. The chemical and biological sensing attributes of CO_2-laser-induced LPFGs fabricated by Bachim [79] have been investigated and indicate improved performance over other types of CO_2-laser-induced LPFGs. The changes in the transmission response with changes in the surrounding refractive index, n_{sri}, were measured for one of these LPFGs [80]. The transmission responses for the grating surrounded by air and surrounded by an index-matching oil are shown in Fig. 1.1(a). The resonant wavelength, λ_{res}, near 1550 nm can be seen to shift approximately 50 nm when surrounded by the oil. The relationship between the resonant wavelength of the grating and the surrounding refractive index is shown in Fig. 1.1(b). The resonant wavelength sensitivity, $d\lambda_{res}/dn_{sri}$, is greater than 2 nm per one one-hundredth change in refractive index units in the biologically and chemically relevant range of indices between 1.40 and 1.45.

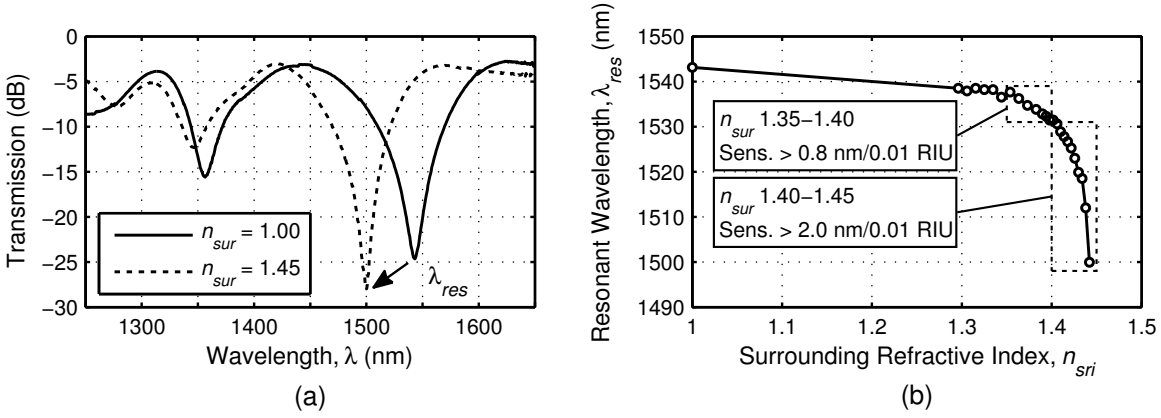

Figure 1.1: Response of a CO_2-laser-induced LPFG to changes in the surrounding refractive index: (a) transmission response of the LPFG when surrounded by air (solid line) and surrounded by an index-matching oil (dashed line); and (b) relationship between the resonant wavelength, λ_{res}, and the surrounding refractive index, n_{sri}. The resonant wavelength sensitivity is indicated for two regions of n_{sri}.

The LPFG fabricated by Bachim has a higher sensitivity to the surrounding refractive index than other reported CO_2-laser-induced LPFGs. The resonant wavelength shift for three CO_2-laser-induced LPFGs is shown in Fig. 1.2. The resonant wavelength shift is calculated as the difference from the resonant wavelength at $n_{sri} = 1.33$. This is done to facilitate the comparison of the three gratings with different resonant wavelengths. The gratings reported by Zhu *et al.*, labeled as LPFG 1 and LPFG 2, are referred to as a conventional LPFG and an edge-written LPFG respectively [78]. The fabrication parameters for the conventional LPFG (LPFG 1) were not reported. The edge-written LPFG (LPFG 2) was fabricated using focused pulses from a high-frequency (10 kHz) CO_2 laser that is reported to change the index of the cladding within only 15 µm from the cladding edge. The grating fabricated by Bachim used focused pulses from a continuous CO_2 laser. The more rapid change in the resonant wavelength with the surrounding refractive index indicates that these gratings can be used to develop chemical and biological sensors.

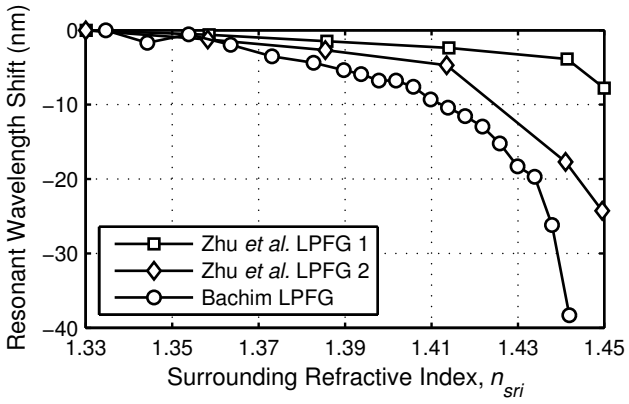

Figure 1.2: Resonant wavelength shift for three CO_2-laser-induced LPFGs. The resonant wavelength shift is calculated as the difference from the resonant wavelength at $n_{sri} = 1.33$. The gratings fabricated by Zhu *et al.* are reported in [78]. The resonant wavelength of the LPFG fabricated by Bachim has the highest sensitivity to changes in the surrounding refractive index.

In addition to showing a higher sensitivity to the surrounding refractive index, these CO_2-laser-induced LPFGs have also been used to fabricate an end-of-fiber

LPFG, which is required to develop compact, probe-type sensors [81]. The end-of-fiber LPFG was fabricated by cleaving a traditional LPFG and mirroring the resulting end-face. The mirror on the end-face was fabricated by dipping the fiber into a molten, low-melting-point metal alloy. This fabrication process and the performance of the resulting mirrors is described in Appendix A.

An image of the mirror and the two LPFG periods closest to the mirror was obtained using reflected-light, differential-interference-contrast (DIC) microscopy and is shown in Fig. 1.3(a). DIC microscopy allows the index modulation in the LPFG to be visualized. The response of the end-of-fiber LPFG before mirroring (dashed line) and after mirroring (solid line) are shown in Fig. 1.3(b). Also shown for reference with the dotted line is the transmission response of the LPFG before it was cleaved. The end-of-fiber LPFG features the band-rejection characteristics of a traditional LPFG and has the potential to enable compact, probe-type sensors. This end-of-fiber LPFG is described in more detail in Appendix A.

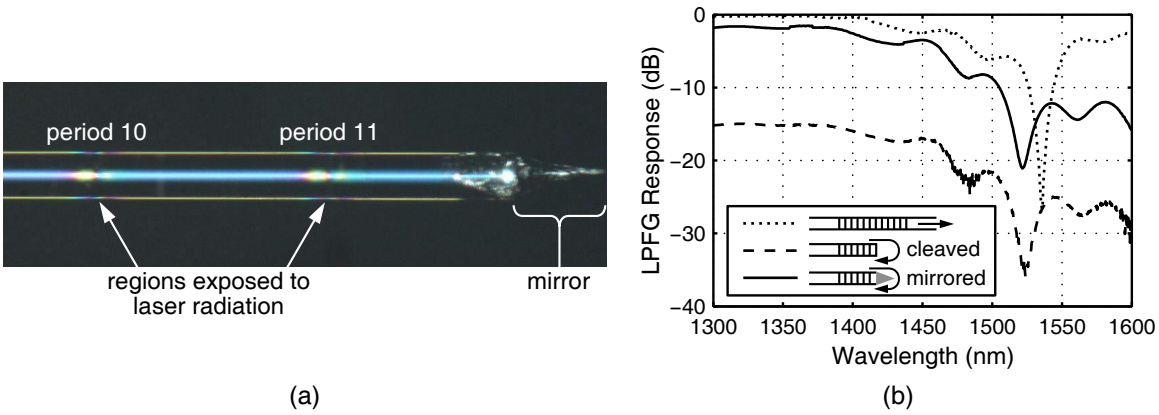

Figure 1.3: End-of-fiber LPFG: (a) DIC microscopy image of the mirror and the two LPFG periods closest to the mirror; and (b) transmission response of the original LPFG (dotted line), the cleaved end-of-fiber LPFG (dashed line), and the mirrored end-of-fiber LPFG (solid line). The end-of-fiber LPFG features the band-rejection characteristics of a traditional LPFG.

1.4.2 Characterization Efforts

Many of the transmission properties of CO_2-laser-induced LPFGs have been measured, including transmission spectra, core-mode to cladding-mode coupling, polarization-mode dispersion, and polarization-dependent loss [82–84]. The commercial equipment necessary to make these measurements is readily available. These properties have also been studied with various perturbations to the LPFG [29, 34]. Despite this extensive understanding of their transmission properties, the development of CO_2-laser-induced LPFGs for use as communication components and sensors has yet to move beyond basic demonstrations of the necessary signal-manipulation and sensing behaviors. The physical properties of CO_2-laser-induced LPFGs must be understood at a fundamental level to enable the modeling and optimizing of their designs for specific communications and sensing applications.

The need to understand the physical properties of CO_2-laser-induced LPFGs has led to several investigations of these properties. A few reports provide an estimate of the change in the RID resulting from the exposure to CO_2-laser radiation, but they do not provide a direct measurement of the RID [23, 85, 86]. Direct measurements of the RID [76, 79] and the RSD [22, 24] have also been performed. However, several of these investigations used custom-fabricated optical fibers that were exposed to levels of CO_2-laser radiation that could not be used for grating fabrication. While these investigations provide insight into the effects of the CO_2-laser radiation, they do not characterize LPFGs fabricated in standard optical-network fiber for commercially competitive applications. Furthermore, the techniques used for these measurements are limited in their accuracy for the characterization of optical fibers and require restrictive assumptions about the functional form of the physical properties. The techniques also require separate equipment to measure the RID and the RSD, making the direct comparison of these properties difficult.

These investigations provide some insight into the physical properties and the fabrication of CO_2-laser-induced LPFGs. However, the required assumptions and measurement limitations result in an incomplete understanding. In addition, no methodology is available to characterize the RID and the RSD with one piece of equipment, leaving the relationship between the exposure to laser radiation, the changes in the RID, and the changes in the RSD unclear. A need exists for techniques that can characterize accurately the RID and the RSD in CO_2-laser-induced LPFGs without the need for assumptions about the functional forms of these properties. The development of a methodology to perform these techniques on the same fiber in one piece of equipment is necessary to understand how the RID and the RSD are related and affected by the exposure to CO_2-laser radiation.

1.5 Research Objectives and Accomplishments

Of the existing techniques that can be used to characterize the RSD and the RID in optical fibers, only the BKC technique and the QPM technique meet the requirements to characterize the RSD and the RID concurrently. Previous research led to the development of the concepts behind each of these techniques. This thesis reports the significant work required to combine the techniques and make them capable of characterizing fibers and fiber-based devices. The realization of a concurrent measurement technique that can be performed in a single experimental apparatus requires identifying and overcoming the challenges of performing microscopic, tomographic measurements on optical fibers. The primary objective of this research is to provide a methodology that is capable of characterizing concurrently the three-dimensional RSD and RID in optical fibers and fiber-based devices.

To validate the developed methodology, the secondary objective of this research is to characterize both unperturbed and modified optical fibers, including fibers with CO_2-laser-induced LPFGs. It is evident from the overview of the existing efforts

to characterize CO_2-laser-induced LPFGs that the techniques used provided useful but limited information about the changes in the RSD and the RID. These LPFGs require a concurrent measurement technique that is fully capable of detecting the three-dimensional spatial variations in the RSD and the RID.

The concurrent measurement methodology developed in this thesis and the characterization performed on CO_2-laser-induced LPFGs and other optical fibers resulted in the following accomplishments:

1. The extension of the BKC technique to provide retardation measurements without the need to use a small-retardation approximation [87].

2. The development of a measurement procedure for obtaining the data necessary to characterize cross-sectional RSDs using the BKC technique and computed tomography [88, 89].

3. The determination of the most appropriate algorithm and associated parameters for calculating the RIP of an optical fiber from a measurement of the phase shift [90].

4. The development of a measurement apparatus that enables the tomographic measurement of optical fibers and fiber-based devices [87–89].

5. The development of custom components and controlling software to enable partial automation of the developed measurement procedure and apparatus [87,89].

6. The development of the first methodology and apparatus capable of performing concurrent measurements of the RSD and the RID of optical fibers and fiber-based devices [87].

7. The first measurement of the cross-sectional RSDs of a cleaved optical fiber [88].

8. The first analysis of the longitudinal variations in the stress that result from cleaving an optical fiber [88].

9. The determination of the optimal experimental parameters for using the QPM technique to characterize optical fibers [87].

10. The first measurements to characterize the dynamic changes in the three-dimensional RSD and RID that occur during the fabrication of CO_2-laser-induced LPFGs [91].

11. The first direct measurement of the three-dimensional functional form of the index modulation present in CO_2-laser-induced LPFGs [91].

12. The unification of several existing reports with the new measurements to present a more coherent and detailed picture of the stress relaxation and densification processes that occur during LPFG fabrication [91].

13. The fabrication of efficient, inexpensive optical fiber end-face mirrors by dipping the fiber into a small puddle of molten metal to achieve reliable, reproducible adhesion of the metal to the fiber end-face [92].

Future long-term goals of this research are that the transmission properties (loss, dispersion, polarization-dependent performance, etc.) of optical fibers and fiber-based devices will be predictable in terms of (1) the physical properties (RSD, RID, etc.) and (2) the fabrication/processing properties (preform characteristics, draw parameters, grating fabrication parameters, etc.).

1.6 Thesis Overview

The research objectives and accomplishments described in the previous section are examined in detail in the following chapters.

The BKC technique for the characterization of RSDs is discussed in Chapter 2 and the QPM technique for the characterization of RIDs is is discussed in Chapter 3. The theory behind the techniques and the procedures for obtaining and analyzing the

data necessary to characterize cross-sectional distributions are examined. Specific measurement issues that impact the ability to perform tomographic measurements and how they are overcome are also discussed. A study of algorithms and associated parameters for calculating the RIP of an optical fiber from a measurement of the phase shift is presented in Chapter 3 and the most appropriate algorithm is determined. Although this study pertains to RIPs, the results are also applicable to calculating the residual-stress profile of an optical fiber from a measurement of the retardation.

The measurement apparatus is described in Chapter 4, including the custom components that enable the tomographic measurement of optical fibers and partial automation. Elements of the apparatus and issues that are specific to the BKC technique and the QPM technique separately are also considered.

Preliminary measurements are presented in Chapter 5. The characterization of an unperturbed Corning SMF-28 fiber is reported and the performance of the techniques is analyzed. Also presented is the first measurement of the cross-sectional RSDs in a cleaved optical fiber and the first analysis of the optimal experimental parameters for using the QPM technique to characterize optical fibers.

The first concurrent measurements of the RSD and the RID in fibers exposed to CO_2 laser radiation are presented in Chapter 6. RSDs and RIDs in regions of a fiber exposed to focused CO_2 laser pulses with incrementally increasing durations are reported and compared. The results are used to analyze the dynamic changes that occur during the fabrication of CO_2-laser-induced LPFGs and to investigate of the relationship between the changes in the RSD and the RID.

Chapter 7 summarizes the research presented in the thesis. Potential future research areas are discussed.

Appendix A provides a detailed description of the optical fiber end-face mirror fabrication process. The performance of the resulting mirrors is discussed and a detailed description of end-of-fiber LPFG is presented.

CHAPTER 2

RESIDUAL-STRESS CHARACTERIZATION

The Brace-Köhler compensator (BKC) technique meets the demands for measuring the low-levels of retardation induced by optical fibers. This chapter describes the efforts to extend this technique to enable the numerous retardation measurements necessary to characterize cross-sectional residual-stress distributions (RSDs). The underlying theory of the BKC technique and the measurement procedure and data analysis required to perform the numerous full-field measurements are described in Sec. 2.1. The underlying theory for the determination of cross-sectional RSDs from a sequence of retardation measurements and the procedures to process the measurements are described in Sec. 2.2. A procedure for detecting and removing background retardations that cannot be accounted for with a background measurement is described in Sec. 2.3.

2.1 Retardation Measurement with the BKC Technique

2.1.1 Theory

A polarization microscope equipped with a BKC is used to determine the retardation of the fiber. A diagram of the relevant optical components is shown in Fig. 2.1. A measurement consists of first placing the fiber sample in the microscope for transverse illumination; the direction of the propagation of the illuminating beam, z_m, is normal to the longitudinal axis of the fiber. The fiber is oriented in the $x_m y_m$ plane at 45 deg from extinction between crossed polarizers, labeled as the polarizer and the analyzer in Fig. 2.1. The principal axes of the fiber are defined as the longitudinal axis and the radial axis.

Next, the compensator is inserted into the optical path with its slow axis in the

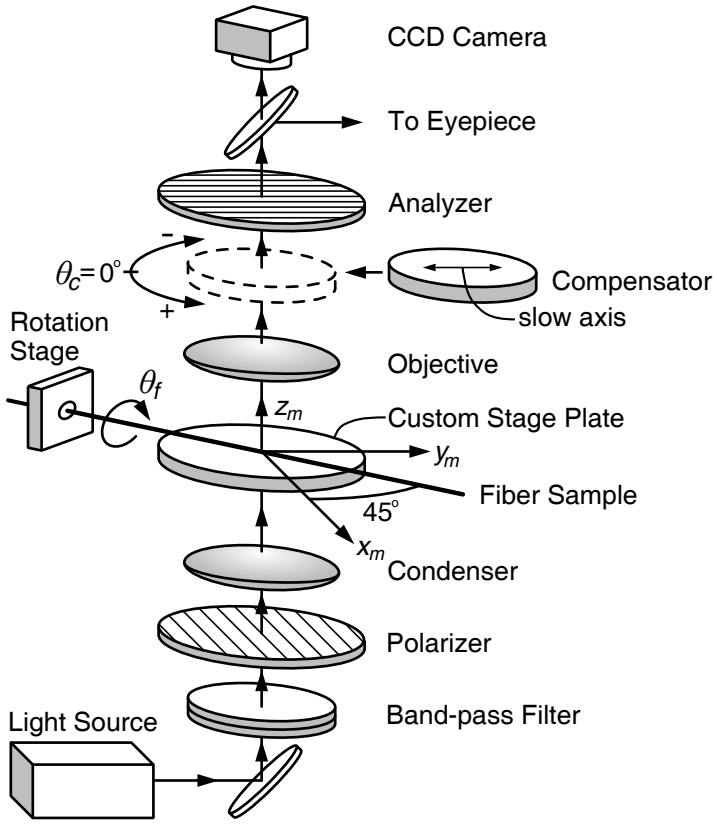

Figure 2.1: Configuration of the optical components of the polarization microscope and a fiber sample used for the determination of the fiber retardation. Rotation of the compensator during a full-field measurement is indicated by θ_c. Axial rotation of the fiber between full-field measurements is indicated by θ_f.

y_m direction. The relative intensity transmitted to the eyepiece or the CCD can be found by considering the fiber sample and the compensator as birefringent waveplates in a two-waveplate system [44]. Using this analysis, the relative transmitted intensity at any point, or pixel, is

$$I = \sin^2 2\theta_c \cos\phi_s \sin^2 \frac{\phi_c}{2} + \sin^2 \frac{\phi_s}{2} \pm \frac{1}{2} \sin 2\theta_c \sin\phi_s \sin\phi_c, \tag{2.1}$$

where ϕ_s and ϕ_c are the phase retardations of the fiber sample and compensator respectively, and θ_c is the angular rotation of the compensator from extinction. The use of the positive sign (+) or the negative sign (−) on the last term depends on the relative orientation of the slow axes of the fiber sample and the compensator. If the slow axis of the fiber sample is aligned at +45 deg from the slow axis of the compensator, then the positive sign is used. However, if this alignment is at −45 deg, then the negative sign is used. The latter relative orientation is shown in Fig. 2.1.

Rotating the compensator will result in a variation in the transmitted intensity as indicated by Eq. (2.1). Minima in the transmitted intensity can be obtained when the compensator is rotated to produce an output polarization with a minimized component along the transmission direction of the analyzer. These minima allow the derivation of an expression that relates the retardation produced by the fiber sample to the angular rotation of the compensator that minimizes the intensity, $\theta_{c,min}$.

The derivative of the relative transmitted intensity, I, with respect to the angular rotation of the compensator, θ_c is

$$\frac{\partial I}{\partial \theta_c} = \cos 2\theta_c \left[2 \sin 2\theta_c \cos\phi_s (1 - \cos\phi_c) \pm \sin\phi_s \sin\phi_c\right]. \tag{2.2}$$

The locations of extrema in the intensity are determined when $\partial I/\partial\theta_c = 0$. The extrema that occur when the second factor (in brackets) equals zero are the intensity minima that are observed when the compensator is oriented at $\theta_{c,min}$ [44]. This factor equals zero when

$$R_s = \frac{\lambda}{2\pi}\phi_s = \frac{\lambda}{2\pi} \arctan\left(\mp \frac{2 \sin 2\theta_{c,min}(1 - \cos\phi_c)}{\sin\phi_c}\right), \tag{2.3}$$

where the retardation of the fiber sample is now expressed in meters and λ is the wavelength of the illuminating light. Therefore, the retardation of the fiber sample, R_s, at a single point is determined by rotating the compensator to determine $\theta_{c,min}$ and solving Eq. (2.3). The use of the positive sign (+) or the negative sign (−) on Eq. (2.3) is reversed from the description given previously for Eq. (2.1). If the slow axis of the fiber sample is aligned at +45 deg from the slow axis of the compensator, then the negative sign on Eq. (2.3) used. If this alignment is at −45 deg, then the positive sign is used. The use of Eq. (2.3) requires that the retardation of the fiber sample is less than the retardation of the compensator. This is satisfied for optical fibers, which have relatively low levels of birefringence and induce much smaller retardations than those produced by commercial compensators.

2.1.2 Measurement Procedure

2.1.2.1 Full-Field Retardation Measurement

The spatially varying birefringence in optical fibers induces a non-uniform retardation over the field of view (FOV) of the microscope. Thus, the compensator angle that produces a minimum of intensity will vary for each resolvable spot, or pixel, within the FOV. A full-field measurement technique similar to the one used with the two-waveplate compensator enables the rapid determination of the retardation over the entire FOV [45]. The full-field technique consists of acquiring images of the FOV for various compensator angles, θ_c. A range of compensator angles, θ_1 to θ_N, is chosen such that for $\theta_1 < \theta_c < \theta_N$, a minimum of intensity is observed for every pixel in the captured image. The compensator is rotated sequentially from θ_1 to θ_N in small increments, typically 0.5−1 deg, and an image is captured at each increment and stored for later processing. The dashed enclosed portion of the flow chart in Fig. 2.2 represents the full-field measurement.

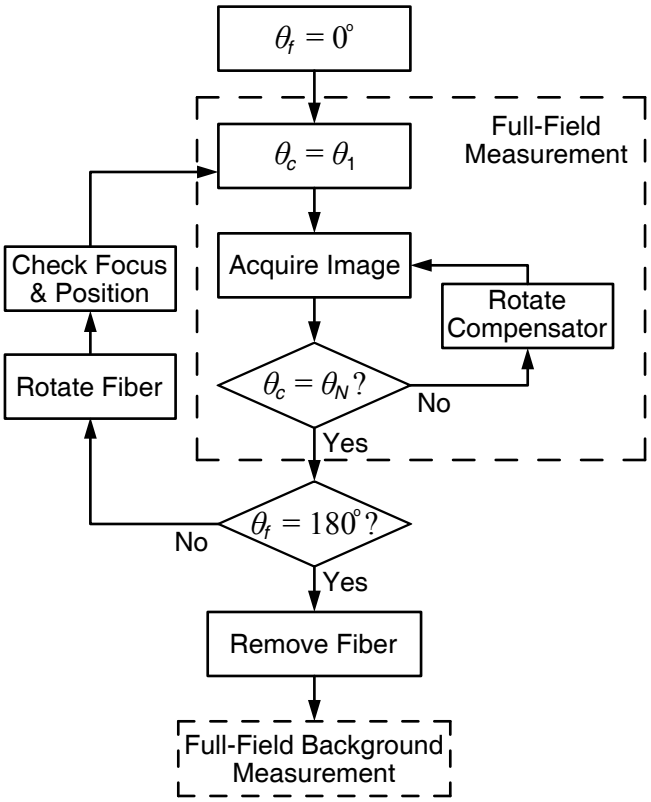

Figure 2.2: Flow chart of the measurement process for obtaining the images necessary for the determination of cross-sectional RSDs. The large dashed-enclosed portion represents the image acquisition process for a full-field measurement. This image acquisition process is repeated once with the fiber removed from the FOV for the background measurement.

2.1.2.2 Tomographic Measurement

The determination of cross-sectional RSDs requires retardation measurements spanning $0 \leq \theta_f < 180$ deg. The measurements are made at various angles by rotating the fiber about its longitudinal axis within the microscope. After the first full-field retardation measurement at $\theta_f = 0$, the fiber is rotated by a small amount. The focus and the positioning of the fiber are checked; occasionally radial runout requires the fiber to be re-focused and/or re-centered within the FOV. A full-field retardation measurement is then performed at the new rotation angle. The process of rotating the fiber and performing a full-field retardation measurement is repeated until the fiber has been rotated 180 deg. The fiber is rotated in increments of 2 deg, which corresponds to 89 full-field retardation measurements. When the fiber reaches 180 deg, it is removed from the FOV and a full-field background measurement is performed to characterize the presence of birefringence and other effects in the imaging system. The entire flow chart in Fig. 2.2 represents the full procedure for obtaining the set of full-field retardation measurements necessary to determine the cross-sectional RSD.

2.1.2.3 Checking the Focus of the Fiber

The focus of the fiber is checked between full-field measurements by viewing the fiber with the analyzer removed from the optical path. Removing the analyzer provides significantly more light to the CCD and enables the real-time monitoring of the focus and the position of the fiber. Furthermore, with the analyzer removed, the fiber appears transparent except at the boundaries between regions with different indices of refraction. The observation of the effects of refraction and diffraction at these boundaries enables the rapid, qualitative determination of the focus of the fiber. These boundary effects are shown in Fig. 2.3. The images of the fiber in Fig. 2.3(a) reveal that the strong boundary effects present when the fiber is defocused are minimized when the fiber is in focus. Also shown in Fig. 2.3(b) are the average vertical profiles

for each image. Averaging the vertical profiles reduces the noise present in the images to isolate the boundary effects. A real-time average vertical profile is displayed on a custom LabVIEW virtual instrument to enable the rapid and accurate determination of the position of best focus of the fiber [93]. The analyzer must be reinserted manually into the optical path before performing the next full-field measurement.

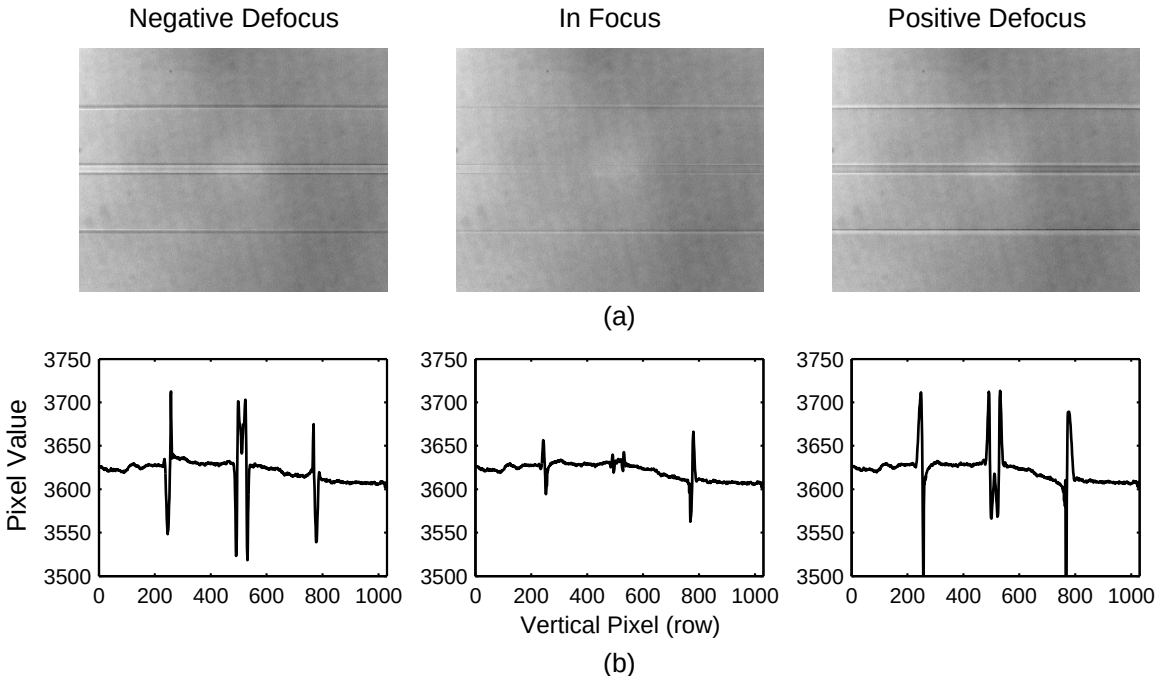

Figure 2.3: Effects of defocusing an optical fiber: (a) images of the fiber at a negative defocus, the in-focus position, and a positive defocus; and (b) average vertical profile corresponding to the image above.

2.1.2.4 Measurement Automation

The entire measurement procedure with the exception of checking the focus and position of the fiber is automated using a custom LabVIEW virtual instrument [93]. The images obtained during each full-field measurement are stored with the filename convention `image_thetaf_N`, where `image` is used as a common prefix, `thetaf` is the angular orientation of the fiber, and `N` corresponds to the sequential number of the compensator angle, θ_N. Images are stored in a lossless format such as the Portable

Network Graphics (PNG) format or the Tagged Image File (TIF) format. The use of a lossless format ensures that the relative transmitted intensity recorded by the CCD is stored accurately without the lossy encoding effects present in standard JPEG images. It is recommended that images are stored in the PNG format for reasons that are discussed in Chapter 3. Also stored with the images is a text file, `BKangle.txt`, which contains a list of the actual compensator angular orientations θ_1 through θ_N, in deg.

2.1.3 Image Analysis

The determination of the retardation of the fiber requires three primary steps: (1) the analysis of the images captured at each angular orientation of the fiber, (2) the analysis of the images captured with the fiber removed from the FOV, and (3) the calculation of the retardation using a two-dimensional form of Eq. (2.3). The image analysis procedures required for steps (1) and (2) are identical. The sequence of images captured for each full-field measurement records the variation in the intensity with changing compensator angle, θ_c. For each pixel, $\theta_{c,min}$ is determined. Interpolation of the variation in the intensity with θ_c increases the accuracy of determining $\theta_{c,min}$. The interpolation is performed by fitting the variation in the intensity with a quadratic polynomial. This procedure is shown for an arbitrary θ_f in Fig. 2.4.

The interpolation is performed on one sequence of images at a time for the measurements performed at each angular orientation of the fiber. This results in a two-dimensional map of the compensator angle that produces a minimum of intensity, $\theta_{c,min}^{samp}(z, x', \theta_f)$, for each angular orientation of the fiber, θ_f. The pixels along the longitudinal and the radial directions of the fiber are represented by z and x' respectively. The procedure is also performed on the sequence of images with the fiber removed from the FOV, resulting in $\theta_{c,min}^{back}(z, x')$. This enables the removal of the effects of the background retardation. The nonuniform background in the map of

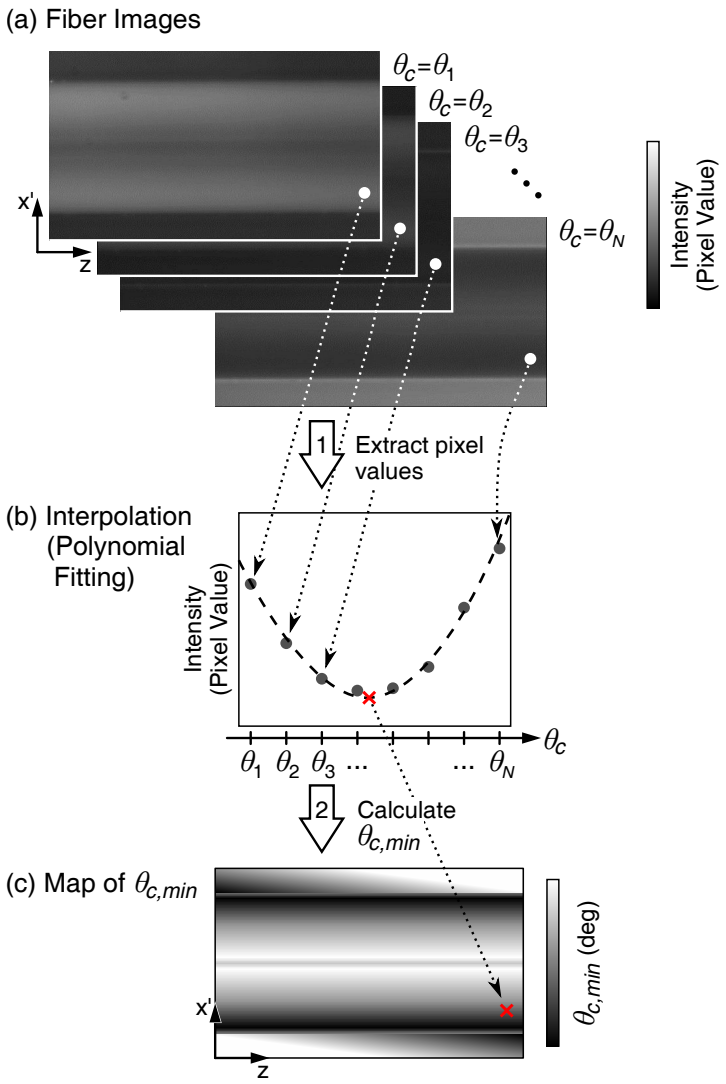

Figure 2.4: Procedure for analyzing images to determine the compensator angles, θ_c, that produce minima of intensity, $\theta_{c,min}$. Step 1: the values of a common pixel are extracted from the fiber images (a) to determine the variation in the intensity with θ_c (b). Step 2: the variation in the intensity is fit with a quadratic polynomial (dashed line) and the location of the minimum is calculated to determine $\theta_{c,min}$ (c).

$\theta_{c,min}$ in Fig. 2.4(c) illustrates the effects that need to be removed by subtracting the background measurement.

Finally, two-dimensional maps of the magnitude of the retardation of the fiber sample (retardation maps), $R_s(z, x', \theta_f)$, are determined for each angular orientation of the fiber using a two-dimensional form of Eq. (2.3),

$$R_s(z, x', \theta_f) = \frac{\lambda}{2\pi} \arctan\left(\mp \frac{2\sin[2\theta_{c,min}^{samp} - 2\theta_{c,min}^{back}](1 - \cos\phi_c)}{\sin\phi_c} \right). \tag{2.4}$$

2.1.3.1 Interpolation by Polynomial Fitting

Previously, higher-order polynomials, typically of degree 5 or 6, were used to fit the variation in the intensity with θ_c [48,88,89]. The degree of the polynomial was chosen based on a qualitative assessment of the polynomial fit and the standard deviation between the fit and the experimental data. However, in the present work it was determined that a higher-order polynomial fit results in a larger level of noise in the calculated R_s. This is caused by the higher-order polynomial fitting to experimental noise in the variation in the intensity with θ_c. The measurement performed on an unperturbed, standard Corning SMF-28 fiber reported in [88] and [89] was analyzed again using a quadratic polynomial fit. The standard deviation of the retardation in the region surrounding the fiber (surrounding-region retardation), which indicates the noise in the measured retardation, decreased from 0.058 nm to 0.028 nm (at $\lambda = 546$ nm). This is a 52% decrease and indicates that the interpolation of the variation in the intensity with θ_c is better performed using a quadratic polynomial fit.

2.2 Residual-Stress Characterization

2.2.1 Relationship Between the Retardation and the Stress

In the absence of external forces, the stress-optic relations describe the relationship between the residual stress and the resulting birefringence induced in the fiber [94].

In general, the residual stress, σ (in $\mathrm{Pa} \equiv \mathrm{N/m^2}$), can be decomposed into normal stress components, σ_x, σ_y, and σ_z, along the three principal orthogonal directions indicated in Fig. 2.5. The stresses induce changes in the normally isotropic refractive index of the materials used in the fiber, n_0, giving rise to unique principal indices of refraction, n_x, n_y, and n_z. The anisotropic, principal refractive indices are related to the isotropic refractive index by

$$\begin{aligned} n_x &= n_0 + C_1\sigma_x + C_2(\sigma_y + \sigma_z), \\ n_y &= n_0 + C_1\sigma_y + C_2(\sigma_x + \sigma_z), \\ n_z &= n_0 + C_1\sigma_z + C_2(\sigma_x + \sigma_y), \end{aligned} \tag{2.5}$$

where C_1 and C_2 are the stress-optic or photoelastic constants of the extraordinary wave and the ordinary wave respectively (in $\mathrm{Pa^{-1}}$). The stresses and the refractive indices are all functions of the spatial position in the fiber. Solving for the difference between any two principal indices of refraction, in this case n_z and n_x, yields the stress-optic law

$$n_z - n_x = C(\sigma_z - \sigma_x), \tag{2.6}$$

where $C = C_1 - C_2$ is also commonly referred to as the stress-optic or photoelastic constant (in $\mathrm{Pa^{-1}}$).

Light that propagates normal to the fiber axis, z, and is linearly polarized at 45 deg relative to the fiber axis, can be decomposed into linearly polarized waves of equal amplitudes in the axial and transverse directions. Illumination in this manner is illustrated in Fig. 2.5. Birefringence between the axial and transverse indices of refraction will result in a path difference, or a retardation, between the axial and transverse polarizations. By inspection of Fig. 2.5 and by application of the stress-optic law, the retardation of a beam passing at an angle θ_f through the fiber can be written as

$$R(x', \theta_f) = C \int_{-\infty}^{\infty} [\sigma_z(x', y') - \sigma_{x'}(x', y')] \, \mathrm{d}y'. \tag{2.7}$$

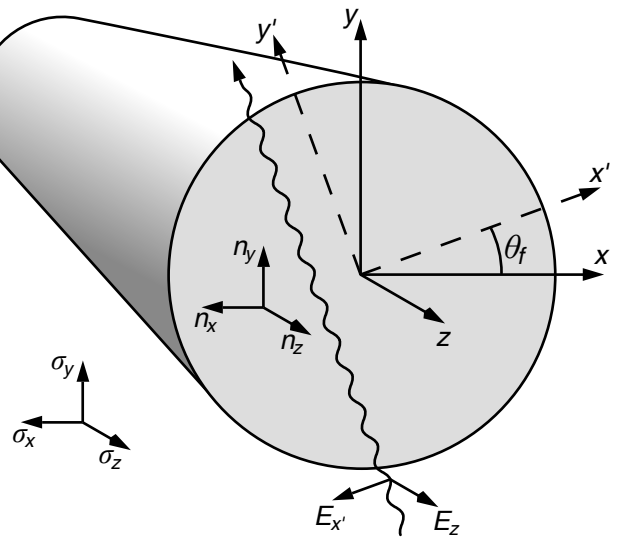

Figure 2.5: Configuration of fiber illumination for birefringence measurements.

In the absence of external forces, the net stress on the $y'z$ plane of the optical fiber must be equal to zero. This requires the line integral of $\sigma_{x'}$ in the y' direction to be equal to zero [94]. Thus, Eq. (2.7) simplifies to

$$R(x', \theta_f) = C \int_{-\infty}^{\infty} \sigma_z(x', y') \, \mathrm{d}y'. \tag{2.8}$$

Equation (2.8) relates the retardation profile of a beam passing at an angle θ_f through the fiber to the axial component of the residual stresses present in the fiber.

2.2.2 Computed Tomography for the Determination of RSDs

For an azimuthally symmetric fiber, the retardation profile is independent of θ_f, and the axial component of the residual-stress profile is obtained from the inverse Abel transform of a single retardation profile [35]. For azimuthally asymmetric fibers, computed tomography principles enable the determination of the axial component of the cross-sectional RSD from a sequence of retardation profiles obtained over 180 deg of rotation of the optical fiber [36].

The Fourier slice theorem provides an equality that enables the axial stress to be determined from the measured retardation. This theorem is shown conceptually in Fig. 2.6. The cross-sectional axial-stress distribution of an optical fiber and transverse

illumination at an angle θ_f are shown in Fig. 2.6(a). The resulting retardation profile is shown in Fig. 2.6(b) and the two-dimensional Fourier transform of the axial-stress distribution is shown in Fig. 2.6(c). For each rotation angle of the fiber, θ_f, the Fourier slice theorem states that the one-dimensional Fourier transform of the retardation profile, $\widetilde{R}$, (b)$\rightarrow$(d), is equal to a radial slice of the two-dimensional Fourier transform of the axial component of the cross-sectional RSD multiplied by C, $C\widetilde{\sigma}_z$, (c)$\rightarrow$(d). Defining s as the spatial angular frequency, this theorem is expressed as

$$\widetilde{R}(s, \theta_f) = C\widetilde{\sigma}_z(s\cos\theta_f, s\sin\theta_f), \tag{2.9}$$

where the coordinates $(s\cos\theta_f, s\sin\theta_f)$ define a slice at an angle θ_f through the spatial angular frequency domain as shown in Fig. 2.6(c).

With retardation profiles spanning $0 \leq \theta_f < 180$ deg, the cross-sectional RSD can be determined using this theorem. However, the direct implementation of Eq. (2.9) requires the retardation profiles, which are obtained in polar coordinates, to be mapped to rectangular coordinates. This can be visualized by tracing from (b)$\rightarrow$(d)$\rightarrow$(c) in Fig. 2.6 with retardation profiles at various angular orientations. This process requires interpolation in the spatial angular frequency domain. The interpolation of spatial angular frequencies will affect all points in the real spatial domain, leading to interpolation errors across the entire RSD. To avoid frequency-domain interpolation, the filtered-backprojection algorithm can be used to implement the Fourier slice theorem [95].

By taking the inverse two-dimensional Fourier transform of Eq. (2.9) and by recognizing that retardation profiles taken 180 deg apart are mirror images, the axial component of the RSD can be expressed as

$$\sigma_z(x', y') = \frac{1}{C}\int_0^{\pi}\left[\int_{-\infty}^{\infty}\widetilde{R}(s, \theta_f)\,|s|\,e^{i2\pi s x'}\,\mathrm{d}s\right]\mathrm{d}\theta. \tag{2.10}$$

The quantity $\widetilde{R}(s, \theta_f)\,|s|$ is the Fourier transform of a measured retardation profile multiplied by a ramp in the spatial angular frequency domain. The ramp serves

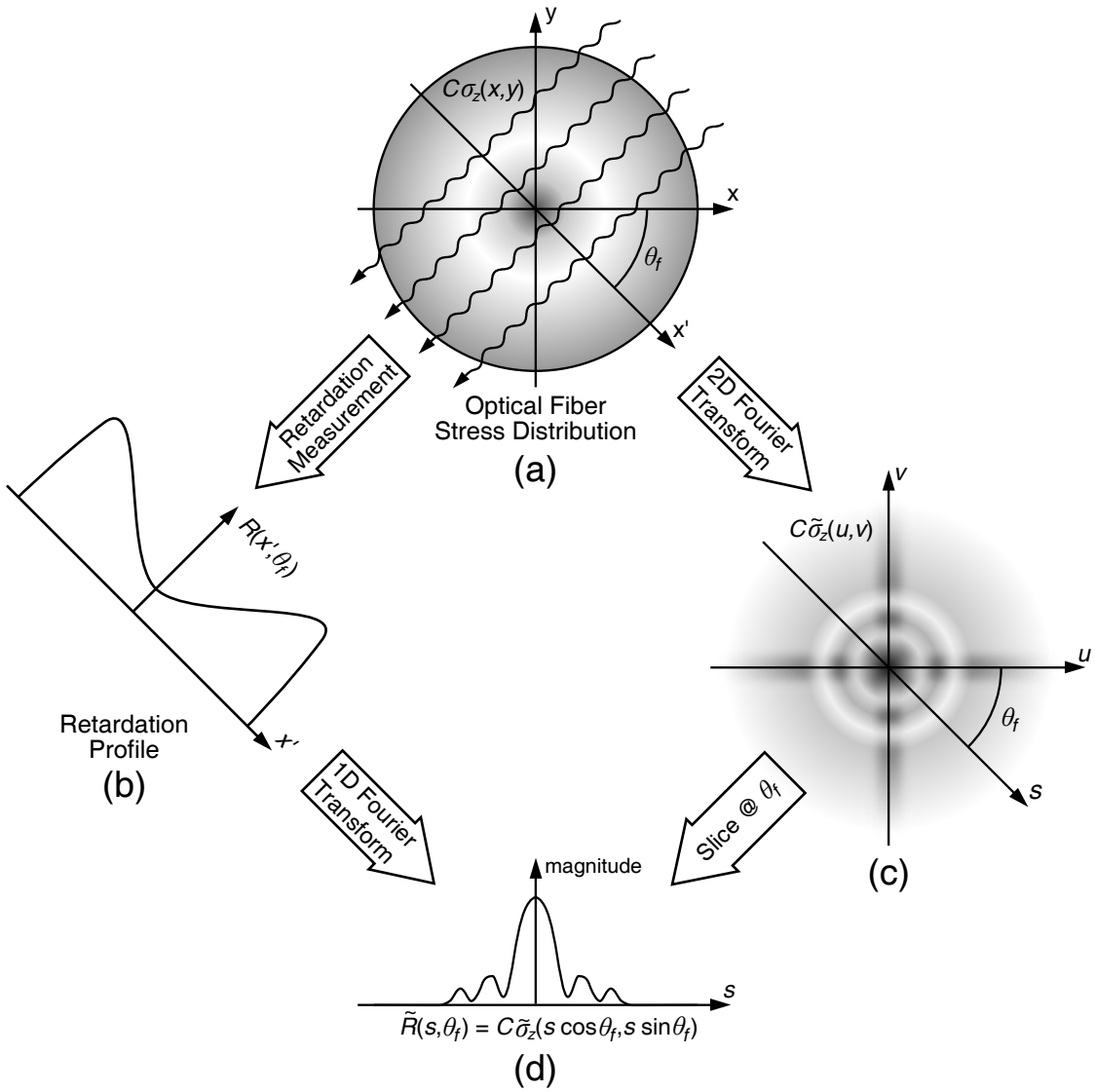

Figure 2.6: Fourier slice theorem applied to the relationship between the measured retardation and the axial stress distribution: (a) cross-sectional axial-stress distribution of an optical fiber and transverse illumination at an angle θ_f, (b) resulting retardation profile, (c) two-dimensional Fourier transform of the axial-stress distribution, and (d) equality of the retardation profile and a slice of the two-dimensional Fourier transform of the stress.

to filter the retardation profile. In practice, the ramp filter may be modified for better performance with noisy data. Equation (2.10) is a form of the inverse Radon transform and permits the determination of the cross-sectional RSD from retardation profiles.

The determination of the axial component of a cross-sectional RSD from the retardation maps requires three primary steps: (1) the extraction of a single radial profile of the retardation from each map, (2) the alignment of the profiles, and (3) the calculation of the axial component of the RSD. These steps are shown in Fig. 2.7.

Each cross-sectional RSD requires only a single radial profile of the retardation at each angular orientation of the fiber. In step 1, the same radial profile, or column of pixels, is extracted from each retardation map (a), resulting in a retardation sinogram (b). In step 2, the alignment of the retardation profiles is performed by detecting and aligning the edges of each profile, resulting in an aligned retardation sinogram (c). The precise alignment and the centering of the retardation profiles are crucial to the accuracy of the RSD. The profiles occasionally require manual alignment in addition to automatic, edge-detection alignment. Finally, in step 3, Eq. (2.10) is used to calculate the axial component of the RSD (d). The quantity $\widetilde{R}(s, \theta_f)$ in Eq. (2.10) is the two-dimensional Fourier transform of the retardation sinogram.

Equation (2.10) is a form of the inverse Radon transform. It is solved numerically using the built-in `iradon` function in MATLAB [96]. This function uses the filtered-backprojection algorithm. The standard ramp-type reconstruction filter is multiplied by a Hann window for the suppression of experimental noise. This enhances the accuracy of the reconstructed RSD in the fiber and smooths out edges and sharp transitions [95, 97].

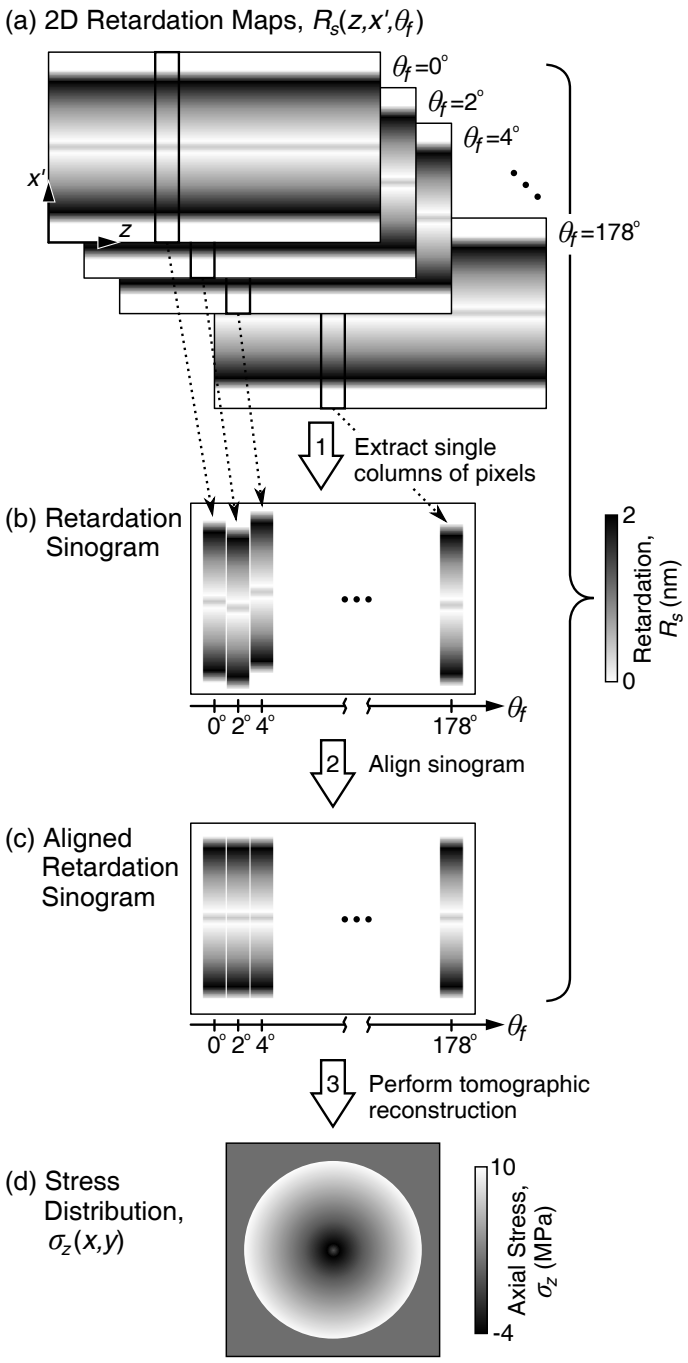

Figure 2.7: Computed tomography principles for determining the axial stress. Step 1: the same column of pixels is extracted from each map (a) to generate the retardation sinogram (b). Step 2: the edges of the fiber are aligned and the sinogram is centered to generate the aligned retardation sinogram (c). Step 3: the filtered-backprojection algorithm is used to calculate the RSD (d).

2.3 Measurement Issues

2.3.1 Background Retardation Removal

Ideally, a background measurement, or a measurement performed without the fiber sample, would be performed at each angular orientation of the fiber. However, as indicated Sec. 2.1.2 and in the flow chart in Fig. 2.2, the background measurement is performed after all the measurements with the fiber have been completed. This is necessary to avoid moving the fiber in and out of the FOV between each angular orientation. This single background measurement cannot account for any drift in the background retardation that occurs during the several hours required to perform the measurements with the fiber.

To investigate the presence of drift, the retardation in the region surrounding the fiber (surrounding-region retardation) was analyzed for measurements performed on an unperturbed, standard Corning SMF-28 fiber. Measurements were made on the fiber for $0^\circ \leq \theta_f \leq 178^\circ$ in angular orientation increments of 2 deg, resulting in a total of 89 measurements and taking 7.1 hours to complete. The background measurement was performed after all the measurements with the fiber were complete. The plot in Fig. 2.8 shows the mean, μ_R, and standard deviation, σ_R, of the surrounding-region retardation at each angular orientation of the fiber plotted as a function of elapsed measurement time.

The standard deviation (dashed line) remains relatively constant, indicating that the background noise remains constant during the time required to perform the measurements. The mean (solid line) increases from a minimum at $t_m = 0$ to approximately zero for the final measurements near $t_m = 7.1$ hours. The measurements with a mean that is not equal to zero indicate that the background retardation was not fully removed by the background measurement, and thus that the retardation map has an overall bias. The resulting bias is removed from each retardation map by subtracting from it the mean of the surrounding-region retardation. The increasing

trend in the mean of the surrounding-region retardation affirms that the background retardation drifts during the time required to perform the measurements. The drift is likely due to small variations in the birefringence of the optical components of the microscope as they gradually approach thermal equilibrium.

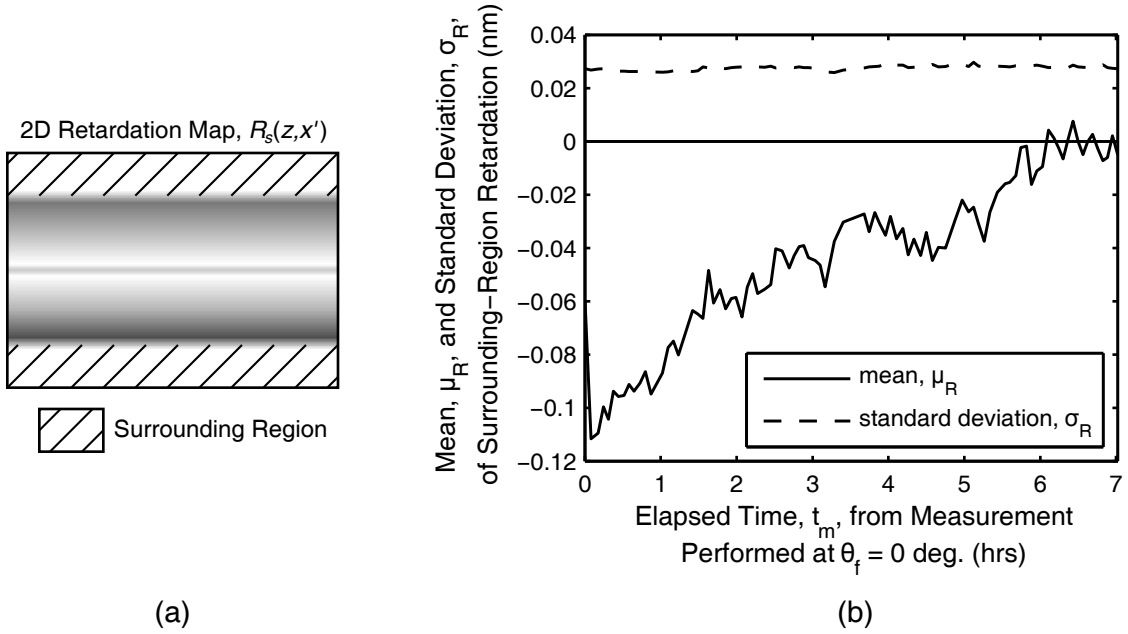

Figure 2.8: Surrounding region: (a) definition for one angular orientation, θ_f, and (b) plot of mean (solid line) and standard deviation (dashed line) of the surrounding-region retardation at each angular orientation of the fiber. The x-axis indicates the elapsed measurement time, t_m, in hours. The measurement at $t_m = 0$ corresponds to $\theta_f = 0$ deg.

CHAPTER 3

REFRACTIVE-INDEX CHARACTERIZATION

The quantitative-phase microscopy (QPM) technique meets the demands for performing the phase-shift measurements necessary to characterize the cross-sectional refractive-index distributions (RIDs) in optical fibers. This chapter describes the efforts to implement this technique alongside the Brace-Köhler compensator (BKC) technique for the concurrent characterization of RIDs. The underlying theory of the QPM technique and the measurement procedure and data analysis required to perform the numerous phase-shift measurements are described in Sec. 3.1. The determination of refractive-index profiles from a single phase-shift measurement and the determination of cross-sectional RIDs from a sequence of phase-shift measurements are discussed in Sec. 3.2. A study of algorithms and associated parameters for calculating the RIP of an optical fiber is presented in this section and the most appropriate algorithm is determined. Procedures for (1) minimizing temperature-induced variations in the phase shift and (2) detecting and removing background retardations that cannot be accounted for with a background measurement are described in Sec. 3.3.

3.1 Phase-Shift Measurement with the QPM Technique

3.1.1 Theory

The microscope used with the BKC technique to determine the retardation of the fiber is also used with the QPM technique to determine the phase shift induced by the fiber. However, the compensator and analyzer are removed from the optical path and other components are added or adjusted. A diagram of the relevant components is shown in Fig. 3.1.

By assuming that refraction is minimal, the intensity distribution, I, and the

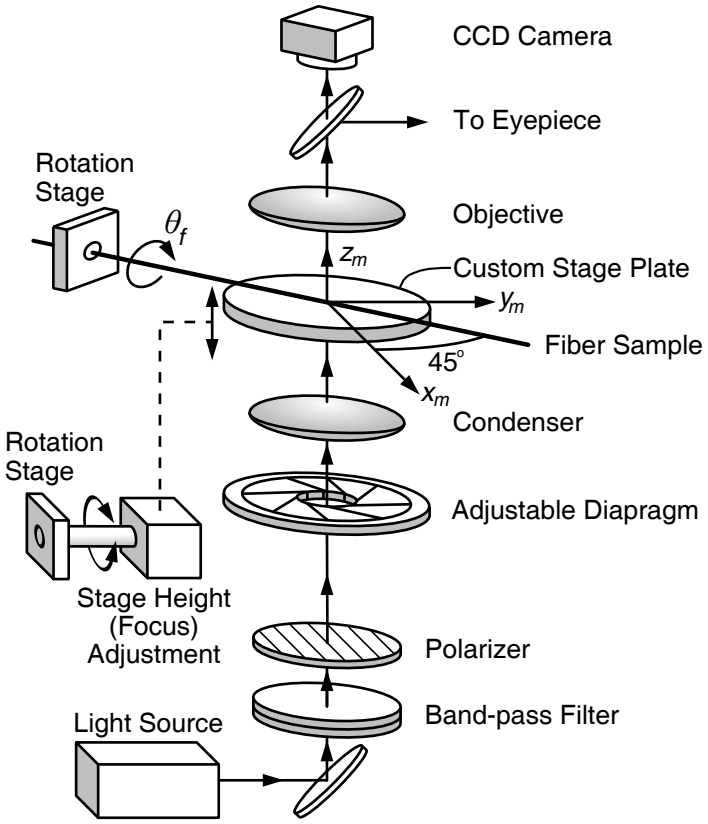

Figure 3.1: Configuration of the components of the microscope and a fiber sample used for the determination of the phase shift produced by the fiber. Axial rotation of the fiber between measurements is indicated by θ_f. Focusing and defocusing of the fiber is achieved by moving the stage plate of the microscope in the vertical direction, z_m.

phase-shift distribution, φ, of the light transmitted through the fiber are related by the transport of intensity equation (TIE)

$$-\frac{2\pi}{\bar{\lambda}}\frac{\partial I}{\partial z_m} = \nabla_\perp \cdot (I \nabla_\perp \varphi), \tag{3.1}$$

where $\bar{\lambda}$ is the mean wavelength of the light source and $\nabla_\perp = \frac{\partial}{\partial x_m} + \frac{\partial}{\partial y_m}$ [65, 67, 98]. The phase shift, φ, is defined as the difference in the phase accumulated by the light transmitted through the fiber and the phase accumulated by the light transmitted through the medium surrounding the fiber. The intensity and phase-shift distributions are in the transverse plane of the fiber, or the $x_m y_m$ plane as indicated in Fig. 3.1. Therefore, the intensity is observed through the eyepiece or by the CCD when the fiber is in focus and the longitudinal derivative of the intensity, $\partial I/\partial z_m$, is observed by defocusing the fiber. Here longitudinal refers to the direction of propagation of the illuminating beam in the microscope, z_m. Defocusing is achieved by moving the stage plate of the microscope in the vertical direction (z_m) as indicated in Fig. 3.1.

The in-focus intensity distribution is obtained by capturing an image of the fiber. The longitudinal derivative of the intensity is approximated using the central difference formula

$$\frac{\partial I}{\partial z_m} \approx \frac{I(z_{m0} + \delta z_m) - I(z_{m0} - \delta z_m)}{2\,\delta z + m}, \tag{3.2}$$

where z_{m0} is microscope stage height when the fiber is in focus and δz_m is the displacement of the stage to defocus the fiber. Thus, the intensity derivative is obtained by capturing images of the fiber when it is defocused above and below the position of best focus.

With this information, the TIE, Eq. (3.1), can be solved for the phase-shift distribution

$$\varphi = \nabla_\perp^{-2}\left[\nabla_\perp \cdot \left(\frac{1}{I}\nabla_\perp\left[\nabla_\perp^{-2}\left(-\frac{2\pi}{\bar{\lambda}}\frac{\partial I}{\partial z_m}\right)\right]\right)\right], \tag{3.3}$$

where $\nabla_\perp^{-2}$ is the inverse Laplacian [98]. This equation can be solved numerically by evaluating $\nabla_\perp$ and $\nabla_\perp^{-2}$ using fast Fourier transforms [99]. Thus, the phase shift

induced by the fiber can be determined by obtaining an in-focus image of the fiber, obtaining two defocused images, and then solving Eq. (3.3).

3.1.2 Measurement Procedure

3.1.2.1 Full-Field Phase-Shift Measurement

The in-focus and defocused images capture the entire field of view (FOV), and the process to solve Eq. (3.3) for the phase shift operates pixel-by-pixel on the images. Therefore, the QPM technique is inherently a full-field measurement technique. The microscope stage plate is moved sequentially through the positive defocus, in-focus, and negative defocus positions. An image is captured at each position.

3.1.2.2 Tomographic Measurement

The determination of cross-sectional RIDs requires phase-shift measurements spanning $0 \leq \theta_f < 180$ deg. The measurements are made at various angles by rotating the fiber about its longitudinal axis within the microscope. After the first phase-shift measurement at $\theta_f = 0$, the fiber is rotated by a small amount. The focus and the positioning of the fiber are checked; occasionally radial runout requires the fiber to be re-focused and/or re-centered within the FOV. A phase-shift measurement is then performed at the new rotation angle. The process of rotating the fiber and performing a measurement is repeated until the fiber has been rotated 180 deg. The fiber is rotated in increments of 2 deg, which corresponds to 89 phase-shift measurements.

3.1.2.3 Checking the Focus of the Fiber

The focus of the fiber is checked between full-field measurements using the same procedure as described in Sec. 2.1.2.3.

3.1.2.4 Measurement Automation

The entire measurement procedure with the exception of checking the focus and position of the fiber is automated using a custom LabVIEW virtual instrument [93].

The three images obtained during each full-field measurement are stored with the filename convention `image_thetaf_#a`, `image_thetaf_0a`, `image_thetaf_#b`, where `image` is used as a common prefix, `thetaf` is the angular orientation of the fiber, and `#` corresponds to the defocus distance, δz_m. Images are saved using the lossless Portable Network Graphics (PNG) format.

The PNG format is chosen over the Tagged Image File (TIF) format because of the convention used by LabVIEW in saving 16-bit image files. The CCD camera currently being used captures 12-bit images, which must be saved in a 16-bit image file. LabVIEW adds a bias of 2^{15} to the captured pixel values when saving the 12-bit image data to a 16-bit TIF file. This bias is equivalent to adding a constant value to each intensity in Eq. (3.2) and Eq. (3.3). While adding a constant to the intensities in Eq. (3.2) has no effect on $\partial I/\partial z_m$, adding the constant to the $\frac{1}{I}$ term in Eq. (3.3) scales the calculated phase shift.

3.1.3 Image Analysis

There are three requirements that must be met by the in-focus and defocused images to ensure the accurate determination of the phase shift: (1) the images must be accurately aligned, (2) the magnification of the images must be equal, and (3) the intensities in each image must have the same normalization [99]. The use of a commercial microscope ensures that the images are aligned and have the same magnification. The exposure duration of the CCD camera is held constant to ensure that the intensities in each image have the same normalization. Therefore, no additional processing of the images is required to use them with Eq. (3.2) and Eq. (3.3) to determine the phase shift.

3.2 Refractive-Index Characterization

3.2.1 Relationship Between the Phase Shift and the Refractive Index

Light that propagates normal to the fiber axis, z, will accumulate a phase that is dependent on the cross-sectional RID of the fiber, $n(x, y)$, and the refractive index of the medium that surrounds the fiber, which is typically an index-matching oil, n_{oil}. Illumination in this manner is illustrated in Fig. 3.2. The phase shift induced by the fiber is defined as the difference between the phase accumulated by the light passing through the fiber and the phase accumulated by the light passing through index-matching oil.

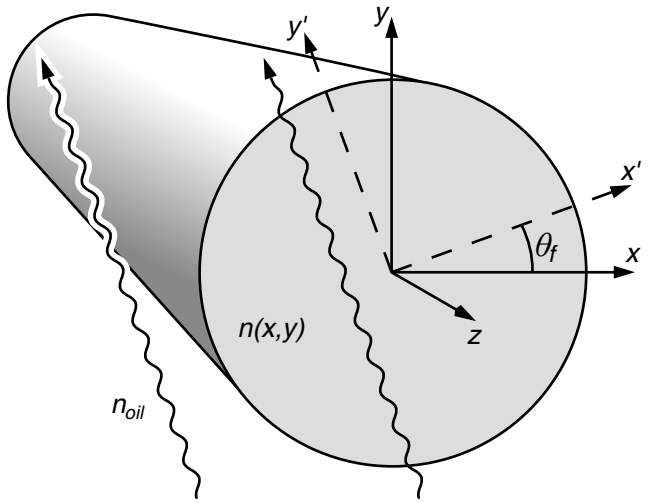

Figure 3.2: Configuration of fiber illumination for phase-shift measurements.

By inspection of Fig. 3.2, the phase shift of a beam passing at an angle θ_f through the fiber can be written as

$$\varphi(x', \theta_f) = \frac{2\pi}{\lambda} \int_{-\infty}^{\infty} \Delta n(x', y') \, \mathrm{d}y', \tag{3.4}$$

where λ is the wavelength of the light source and

$$\Delta n(x', y') = n(x', y') - n_{oil} \tag{3.5}$$

is the relative refractive index. For an azimuthally symmetric fiber, the phase shift profile is independent of θ_f, and the RIP is obtained from the inverse Abel transform of

a single phase-shift profile. For azimuthally asymmetric fibers, computed tomography principles enable the determination of the RID from a sequence of phase-shift profiles obtained over 180 deg of rotation of the optical fiber.

3.2.2 Inverse Abel Transform for the Determination of RIPs

For an azimuthally symmetric fiber, the refractive index varies as a function of radius, r, only. Assuming azimuthal symmetry, Eq. (3.4) can be rewritten as

$$\varphi(x) = \frac{2\pi}{\lambda} \int_{-\infty}^{\infty} \Delta n(x, y)\, \mathrm{d}y, \tag{3.6}$$

where φ, x, and y are independent of θ_f. Transforming Δn and the integral into cylindrical coordinates gives

$$\varphi(x) = \frac{4\pi}{\lambda} \int_{x}^{\infty} \Delta n(r)\, \frac{r}{\sqrt{r^2 - x^2}}\, \mathrm{d}r, \tag{3.7}$$

where x and r both correspond to the radial distance from the longitudinal fiber axis. The use of two separate symbols is necessary for mathematical and experimental reasons. Mathematically, the two symbols are used for distinction. Experimentally, x is used for the optical measurement and r is used for the calculated physical property. Equation (3.7) is a form of the Abel transform. Therefore, the relative refractive index is given by the inverse Abel transform of the measured phase shift

$$\Delta n(r) = -\frac{\lambda}{2\pi^2} \int_{r}^{\infty} \frac{\partial \varphi(x)}{\partial x}\, \frac{1}{\sqrt{x^2 - r^2}}\, \mathrm{d}x. \tag{3.8}$$

In practice, the upper integration limit is set to the maximum radius of the region of interest. This is typically the core radius or the cladding radius when characterizing optical fibers.

Several algorithms are available to compute the RIP via the inverse Abel transform. Direct numerical computation of the transform requires differentiation. However, with noisy measurement data, this can lead to large errors in the calculated RIP [100]. Many early algorithms to compute the transform can be characterized

by the use of curve fitting techniques to smooth out the noisy data, thus allowing for analytic differentiation. See [100] and [101] for a thorough review. Other algorithms were developed that manipulated the inverse Abel transform to remove the derivative [102, 103]. However, it was shown that manipulating the transform did not always remove the errors inherent in numerically differentiating the noisy data [104].

Two algorithms based on Fourier theory (Fourier algorithms) were developed that represent the measured data as a Fourier cosine series [105, 106]. While these algorithms showed improvements over previous algorithms when used with noiseless data, their performance with noisy data was not reported. An iterative algorithm was developed that uses a scaled version of the noisy data as a first approximation of the calculated data and then iteratively improves the calculated data using further manipulated versions of the noisy data [107]. This algorithm showed improvements over previous algorithms when used with noisy data.

In this section, the performance of a direct differentiation algorithm, the iterative algorithm [107], and the more recent of the two Fourier algorithms [106] for the computation of the RIP of optical fibers via the inverse Abel transform is analyzed [90]. The direct differentiation algorithm is chosen because it uses common numerical methods to solve directly the inverse Abel transform. The iterative algorithm is chosen for its demonstrated performance on noisy data. The Fourier algorithm is chosen because it was used with several of the RID and RSD characterization techniques mentioned in Chapter 1 [46, 68, 108].

3.2.2.1 Comparison of the Inverse Abel Transform Algorithms

To evaluate the performance of an inverse Abel transform algorithm, five main steps were as follows:

1. A mathematical model was chosen for the model relative RIP.

2. A model phase-shift profile was calculated analytically using the forward Abel

transform, Eq. (3.7), of the model RIP.

3. Noise was added to the model phase-shift to simulate an experimentally measured, noisy phase-shift profile.

4. The relative RIP was numerically calculated from the noisy phase shift using the inverse Abel transform algorithm.

5. The performance of the algorithm was quantified by calculating the root mean square (RMS) error between the calculated RIP and the model RIP.

A model of a fiber core with a power-law profile featuring a central dip was chosen as the model RIP [105]. Mathematically, this profile is expressed as

$$\Delta n(r) = \delta n(1 - r^2) - \delta n D\Big(\frac{1}{1 + r^2/W^2} - \frac{1}{1 + 1/W^2}\Big), \tag{3.9}$$

where r is the radial distance from the longitudinal fiber axis and D and W correspond to the depth and width of the central dip. The radial distance, r, is normalized to the fiber core radius. For a profile with no central dip ($D = 0$), the parameter δn corresponds to the maximum refractive-index difference between the core and the cladding. For the results presented in the following sections, a profile with a moderate central dip ($D = 0.5$, $W = 0.1$, and $\delta n = 1$) was chosen. This model RIP is shown in Fig. 3.3.

The model phase-shift profile corresponding to the RIP of Eq. (3.9) was calculated analytically using the forward Abel transform. The model phase-shift profile resulting from the RIP with a moderate central dip is shown with the solid line in Fig. 3.4. The radial distance from the longitudinal fiber axis, x, is normalized to the fiber core radius.

Noise was added to the model phase-shift profile to simulate an experimental measurement. In practice, the phase-shift profile is extracted from digitally captured images of the fiber. The resolution of the imaging system determines the number of

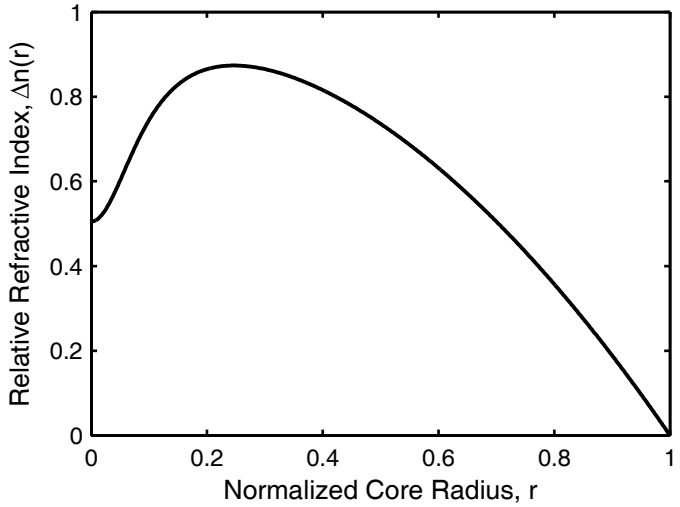

Figure 3.3: Model relative RIP featuring a moderate central dip ($D = 0.5$, $W = 0.1$, $\delta n = 1$).

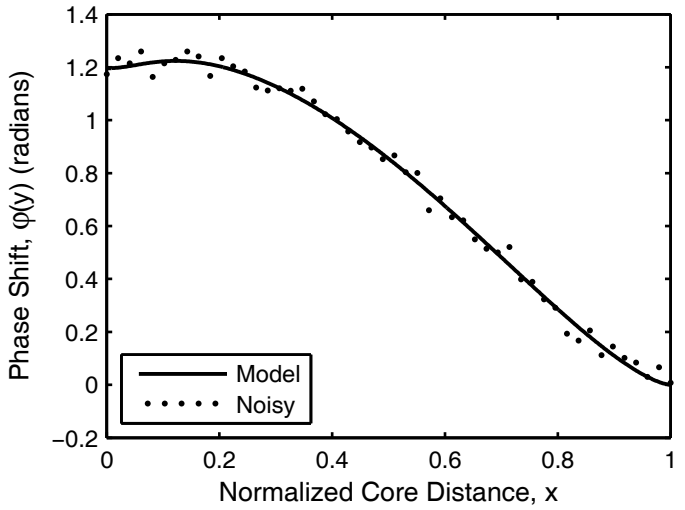

Figure 3.4: Model (solid line) and noisy (dots) phase-shift profiles. The noisy phase shift has an RMS error of 0.03 radians (1.72 deg) when compared with the model phase shift.

points in the measured phase shift along the fiber core radius, between $r = 0$ and $r = 1$. For the noisy phase-shift profile, 50 points were chosen along the fiber core radius. This corresponds to a transverse image of the fiber that captures the radial profile of the phase shift with 50 pixels. To simulate experimental measurements, Gaussian-distributed random noise was added to each point of the model phase shift. The mean of the Gaussian-distributed noise was zero and the standard deviation was chosen to yield a noisy phase shift with an RMS error of 0.03 radians (1.72 deg) when compared with the model phase shift. This level of noise was chosen to match the noise levels observed in phase-shift measurements made using the microinterferometric optical phase tomography (MIOPT) technique [61]. A typical noisy phase-shift profile is shown with the dots in Fig. 3.4.

The calculation of the RIP from the noisy phase shift was performed by using a direct differentiation algorithm, the iterative algorithm [107], and a Fourier algorithm [106]. Each algorithm featured one or more variable parameters that were sequentially varied to determine their optimal values. In the direct differentiation algorithm, both the differentiation and the integration in the inverse Abel transform were performed numerically. The differentiation was performed by using a combination of forward-, central-, and backward-difference approximations. The integration was performed by using a trapezoidal approximation. The performance of each approximation, and therefore the algorithm, was affected by the spacing between the noisy phase-shift data points. This spacing was varied by using linear interpolation to change the number of points along the fiber core radius, N, for the noisy phase shift.

The iterative algorithm, described in [107], requires numerical integration to be performed over the fiber core radius. Thus, N is a parameter in this algorithm. The iterative algorithm also requires the iterative improvement of an initial approximation of the relative RIP. The RIP is first approximated by a scaled version of the noisy phase shift and then iteratively improved by adding to it further manipulated versions

of the noisy phase shift. Therefore, the number of iterations, m, is a second parameter.

The Fourier algorithm, described in [106], uses a Fourier cosine series to represent the noisy phase-shift data. Therefore, the first parameter is the number of Fourier harmonics, k. The algorithm also requires the numerical integration of the Fourier cosine series. Therefore, the step size used for this integration, defined as dt, is a second parameter. The parameter N is also included because of the dependence of the Fourier cosine series on the number of points along the fiber core radius.

For each algorithm, the parameters were sequentially varied over a range that contained the values that gave the best algorithm performance. For each value of the parameters, the RMS error between the calculated RIP and the model RIP was determined. Each algorithm was tested with 100 noisy phase-shift profiles to determine the average performance. The average RMS error between all 100 calculated RIPs and the model RIP was used to assess the overall performance of an algorithm and to determine the optimal values of the parameters.

The determined optimal values for the parameters are not absolute, but rather provide an indication of a small range of the parameters that can be used to analyze qualitatively the calculated RIPs. The values given are also for the specific RIP and simulated noise discussed previously. To provide more general results, two steps were taken: (1) a RIP with a deeper, more narrow central dip ($D = 1$, $W = 0.05$) was tested to determine the effect of a more rapidly varying RIP and (2) noisy phase-shift profiles with 100 points along the fiber core radius were tested for both RIPs. The effects of changing the RIP and the number of points used when adding noise are discussed for each algorithm.

3.2.2.2 Direct Differentiation Algorithm Performance

The average RMS error in the RIPs calculated with the direct differentiation algorithm is shown in Fig. 3.5. Also shown is the standard deviation of the RMS error. At

the minimum in the average RMS error, the standard deviation is 0.015. Two important features are illustrated in Fig. 3.5. First, there is a minimum in the average RMS error followed by a steady increase as N is increased. The effect of increasing N is to decrease the spacing between the points in the approximation of the derivative. With noiseless data, a decreased spacing would lead to a more accurate result. With noisy data however, a smaller spacing results in more noise being added to the result [100].

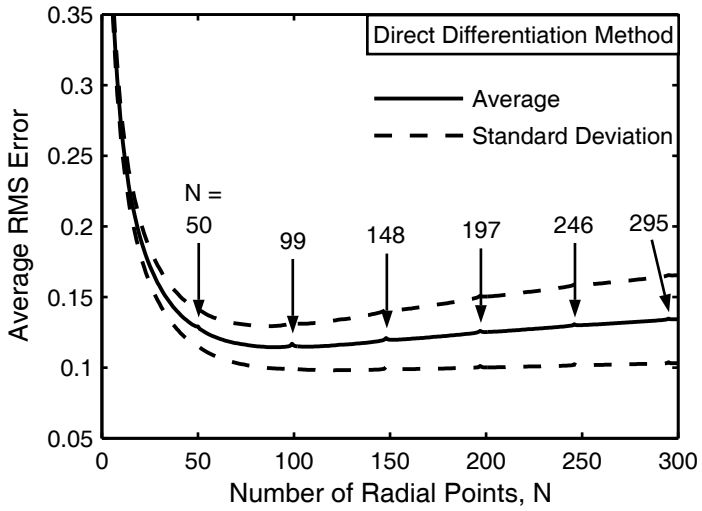

Figure 3.5: Average RMS error in the RIPs calculated with the direct differentiation algorithm. The minimum average RMS error is 0.11 and occurs for $N = 91$. Values of N with small spikes in the error because of interpolation effects are indicated.

Second, there is a small increase (spike) in the average RMS error when N is near a multiple of 50. In general, the interpolated data will exactly represent the original noise added if

$$N = (N_0 - 1)i + 1, \tag{3.10}$$

where N_0 is the original number of points in the noisy phase shift and i is a positive integer. For the results shown in Fig. 3.5, $N_0 = 50$, and thus the interpolated data exactly represents the original noise for the values of N indicated in the figure. However, when N is not given by Eq. (3.10), the interpolated data points will not match with the original noise. This leads to a smoothing of the original noise and

a decrease in the RMS error in the calculated RIP. These features indicate that the optimal value of N is $50 < N < 100$, or in general $N_0 < N < 2N_0$.

Qualitatively, the direct differentiation algorithm produced the lowest-quality calculated RIPs. The error in the calculated RIPs was often large in some regions and small in others. This is due to the random distribution of noise in the phase-shift profiles and the point-by-point operation of the numerical differentiation; the regions with larger amounts of noise in the phase shift resulted in regions with larger error in the RIP. Furthermore, the calculated RIPs often underestimated the model RIPs. A typical calculated RIP with these characteristics is shown by the dots in Fig. 3.6.

The performance of the direct differentiation algorithm was similar for the RIP with the deeper, more narrow central dip. For profiles with a noisy phase shift with $N_0 = 100$, the minimum average RMS error occurred for values of N around 150. This further supports the general rule of $N_0 < N < 2N_0$.

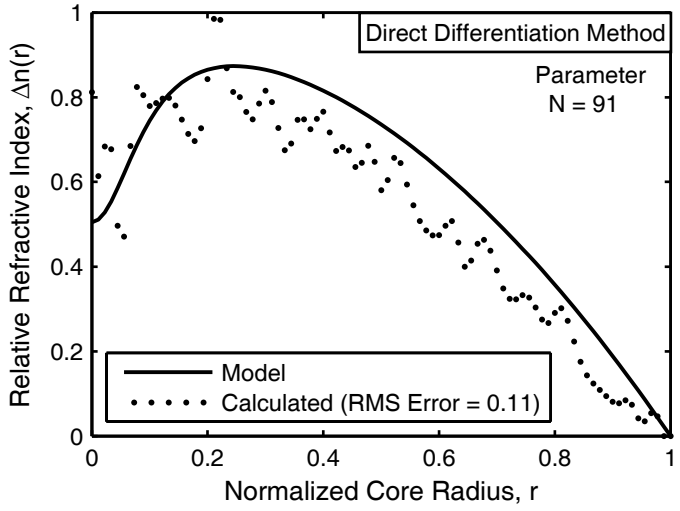

Figure 3.6: Typical relative RIP calculated with the direct differentiation algorithm (dots). Shown for reference is the model RIP (solid line). The calculated RIP illustrates the nonuniform distribution of the error and the underestimation of the model RIP.

3.2.2.3 Iterative Algorithm Performance

The average RMS error in the RIPs calculated with the iterative algorithm is shown in Fig. 3.7. Although the standard deviation in the RMS error is not shown, it follows a trend similar to the trend in the direct differentiation algorithm. For small values of N and m, the standard deviation is low; as N and m increase, the standard deviation increases monotonically. At the minimum in the average RMS error, the standard deviation is 0.014.

Two important features are illustrated in Fig. 3.7. First, for a constant m, there is an increase (spike) in the average RMS error when N is near a multiple of 50. This feature is similar to the small increases in the error seen with the direct differentiation algorithm and can be explained in the same manner. Second, the minimum in the error occurs near $N = 20$ for most values of m. Qualitatively, this small value of N is too few points to represent the central dip of the RIP. However, the error remains relatively constant for $N \geq 40$. This suggest that the optimal value of N is near, but below the original number of points used in the noisy phase shift. In general, N should be near, but below N_0.

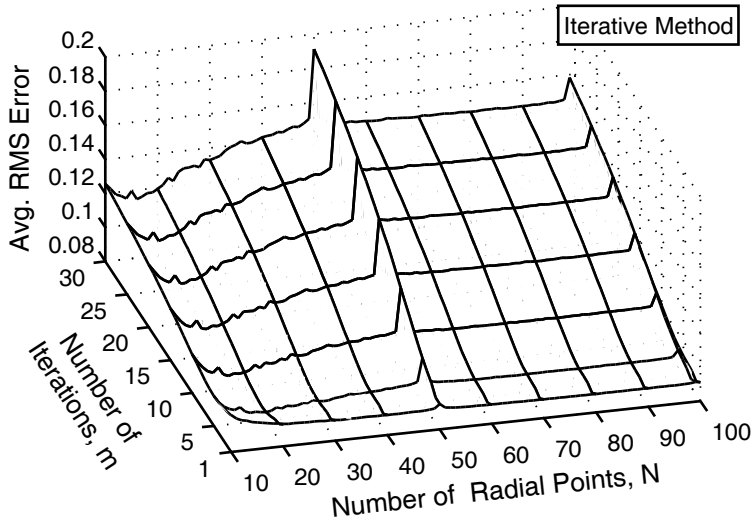

Figure 3.7: Average RMS error in the RIPs calculated with the iterative algorithm. The minimum average RMS error is 0.08 and occurs for $N = 20$ and $m = 6$.

The minimum in the average RMS error for values of N near the optimal value (40 to 49) occurs for $m = 2$. This feature suggests that very few iterations should be performed for data with noise levels similar to those in the simulated noisy phase shifts. However, qualitative analysis of the calculated RIPs reveals that the depth of the central dip was underestimated for small values of m. A value of $m > 8$ was typically required to reproduce the depth of the central dip. Therefore, a tradeoff exists between the RMS error in the entire profile, which is lower for small values of m, and the accurate representation of the central dip, which is better for larger values of m. The error with larger values of m is uniformly distributed, indicating that averaging or filtering may be used to improve the accuracy of the calculated profile. A typical calculated RIP illustrating these characteristics is shown by the dots in Fig. 3.8.

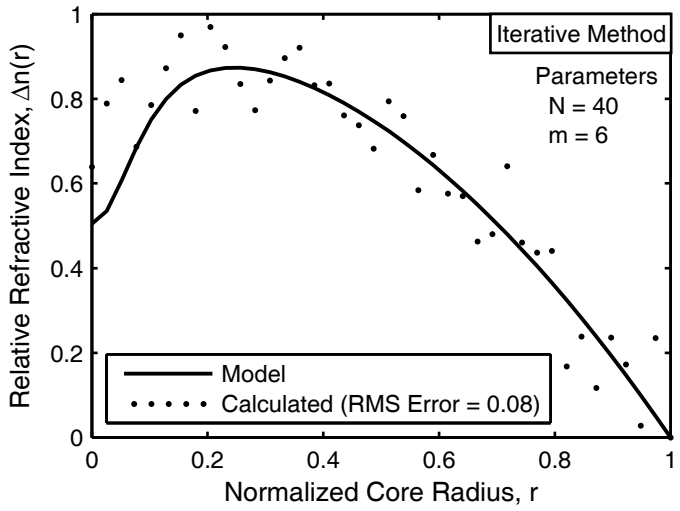

Figure 3.8: Typical relative RIP calculated with the iterative algorithm (dots). Shown for reference is the model RIP (solid line). The calculated RIP illustrates the underestimation of the central dip depth and the uniform distribution of the error.

The need for many iterations to represent accurately the central dip results in poor performance when the iterative algorithm is used with the RIP with a deeper, more narrow central dip. Any accuracy gained in the central dip was overshadowed by large errors throughout the RIP. For the moderate-dip profiles with the noisy phase

shifts with $N_0 = 100$ points along the fiber core radius, the general rule for selecting N and the tradeoff with m remained as given previously.

3.2.2.4 Fourier Algorithm Performance

The average RMS error in the RIPs calculated with the Fourier algorithm is shown in Fig. 3.9. Although the standard deviation in the RMS error is not shown, it follows a trend similar to the trends in the previous two algorithms. For small values of N and k, the standard deviation is low; as N and k increase, the standard deviation increases monotonically. At the minimum in the average RMS error, the standard deviation is 0.011.

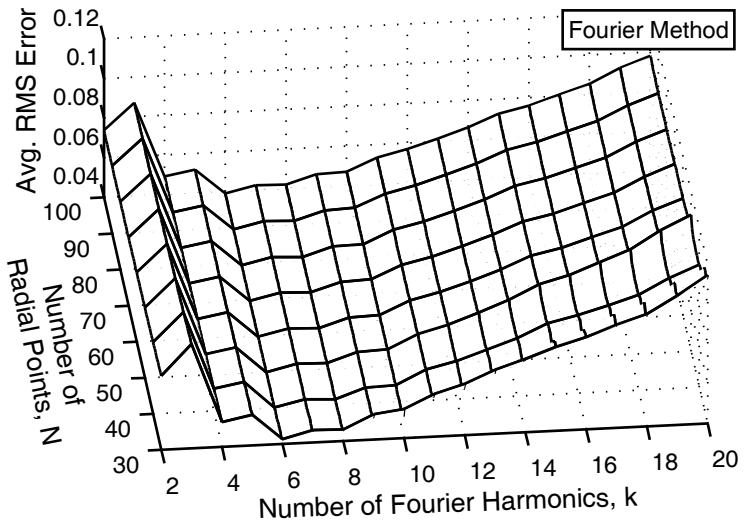

Figure 3.9: Average RMS error in the RIPs calculated with the Fourier algorithm. The minimum average RMS error is 0.04 and occurs for $N = 81$ and $k = 6$.

Two important features are illustrated in Fig. 3.9. First, the RMS error is highly dependent on the choice of k. For a constant N, there is a clear minimum in the RMS error for $k = 6$, followed by a steady increase as k is increased. Furthermore, even values of k generally give better results than odd values. Second, the RMS error is affected very little by N. Slightly visible for large values of k is a small increase in the error with $N = 50$. This is consistent with the interpolation effects discussed

with the previous two algorithms. However, for values of k near the optimal value, this effect is not seen. For $k = 6$, the difference in the average RMS error at $N = 50$ and the absolute minimum RMS error is less than 10^{-3}. Therefore, as long as k is near the optimal value, there is no need to use interpolation to change the value of N.

The average RMS error in the calculated RIPs was found to be large when a large integration step size, dt, was used. However for $dt \leq 10^{-2}$, the error was practically independent of the step size. The integration is performed over a variable that is a transformation of y and r. Therefore, the integration step size should be chosen relative to the range covered by y and r. In the cases presented here, y and r each ranged from 0 to 1. In general, dt should be chosen to be at least one one-hundredth of the range covered by y and r.

Qualitatively, the Fourier algorithm produced the highest quality calculated RIPs. However, a common characteristic observed in the calculated RIPs can be misleading. The relatively small number of Fourier harmonics causes the calculated RIP to vary slowly about the model RIP, as is commonly seen with finite Fourier series representations. While this produces RIPs with evidently little noise, the slow variations could be mistaken for features in the actual RIP. This characteristic is illustrated by the calculated RIP shown by the dots in Fig. 3.10.

The performance of the Fourier algorithm remained independent of N and dt for the RIP with a deeper, more narrow central dip. However, the optimal value of k approximately doubled to around 14 for the more rapidly varying profile. The average RMS error remained independent of N for profiles with noisy phase shifts with $N_0 = 100$ points along the fiber core radius. This further supports the elimination of the interpolation.

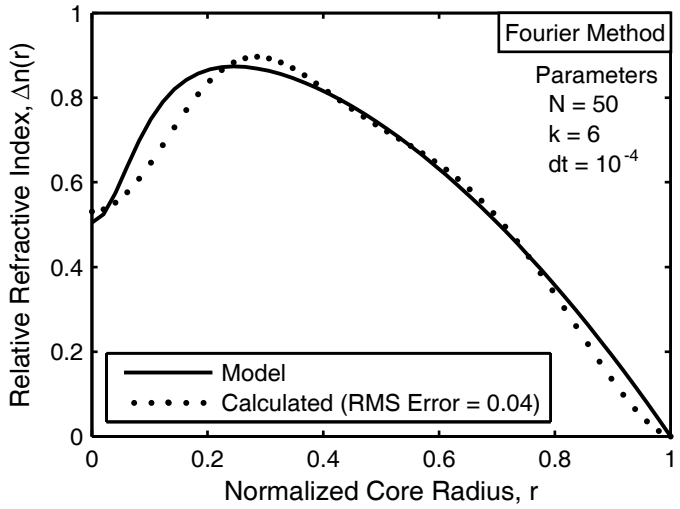

Figure 3.10: Typical relative RIP calculated with the Fourier algorithm (dots). Shown for reference is the model RIP (solid line). The calculated RIP illustrates the slow variations that could be mistaken for actual RIP features.

3.2.2.5 Summary

Of the three algorithms studied, the Fourier algorithm provided the overall best results. The minimum average RMS error for the Fourier algorithm was twice as small as the iterative algorithm and almost three times smaller than the direct differentiation algorithm. The disadvantage of the Fourier algorithm was the presence of slowly varying features in the calculated RIP. This effect may be reduced, with a tradeoff of increased RMS error, by increasing the number of Fourier harmonics. In practice, this decision will require a qualitative analysis of the calculated RIPs.

3.2.3 Computed Tomography for the Determination of RIDs

For azimuthally asymmetric fibers, computed tomography principles enable the determination of the cross-sectional RID from a sequence of phase-shift profiles obtained over 180 deg of rotation of the optical fiber. The relationship between the phase shift and the refractive index expressed in Eq. (3.4) is analogous to the relationship between the retardation and the stress described in Sec. 2.2 and Eq. (2.8). Therefore, following Sec. 2.2.2, the Fourier slice theorem relates the one-dimensional Fourier transform of

the phase-shift profile, $\widetilde{\Phi}$, to a radial slice of the two-dimensional Fourier transform of the cross-sectional RID (multiplied by $\frac{2\pi}{\lambda}$), $\frac{2\pi}{\lambda}\,\Delta\widetilde{N}$. This theorem is expressed as

$$\widetilde{\Phi}(s,\theta_f) = \frac{2\pi}{\lambda}\,\Delta\widetilde{N}(s\cos\theta_f, s\sin\theta_f), \tag{3.11}$$

where the coordinates $(s\cos\theta_f, s\sin\theta_f)$ define a slice at an angle θ_f through the spatial angular frequency domain.

With phase-shift profiles spanning $0 \leq \theta_f < 180$ deg, the entire cross-sectional RID can be determined using Eq. (3.11). However, as described previously, filtered backprojection must be used to avoid the frequency-domain interpolation that is required to use Eq. (3.11). By taking the inverse two-dimensional Fourier transform of Eq. (3.11) and by recognizing that phase-shift profiles taken 180 deg apart are mirror images, the relative RID can be expressed as

$$\Delta n(x',y') = \frac{\lambda}{2\pi}\int_0^{\pi}\left[\int_{-\infty}^{\infty}\widetilde{\Phi}(s,\theta_f)\,|s|\,e^{i2\pi s x'}\,\mathrm{d}s\right]\mathrm{d}\theta. \tag{3.12}$$

The quantity $\widetilde{\Phi}(s,\theta_f)\,|s|$ is the Fourier transform of an original phase-shift profile multiplied by a ramp in the spatial angular frequency domain. In practice, the ramp filter may be modified for better performance with noisy data. Equation (3.12) is a form of the inverse Radon transform and permits the determination of the cross-sectional RID from phase-shift profiles.

The determination of a cross-sectional RID from the phase-shift maps requires three primary steps: (1) the extraction of a single radial profile of the phase-shift from each map, (2) the alignment of the profiles, and (3) the calculation of the RID. These steps are analogous to the steps required for the determination of RSDs. The procedures are identical to those discussed in Sec. 2.2 and shown in Fig. 2.7, except for now using Eq. (3.12) to calculate the RID. The quantity $\widetilde{\Phi}(s,\theta_f)$ in Eq. (3.12) is the two-dimensional Fourier transform of the phase-shift sinogram.

3.3 Measurement Issues

3.3.1 Temperature Sensitivity

Fluctuations in temperature affect the refractive index of the fiber and the medium surrounding the fiber (index-matching oil). Temperature-induced variations in the refractive indices result in variations in the phase shift through the fiber. The phase shift is affected primarily from changes in the refractive index of the index-matching oil. The oil has a much larger temperature coefficient, dn/dT, than the optical fiber. For example, the Cargille Labs index-matching oil typically used for the measurements presented in this thesis has a temperature coefficient of $dn/dT = -3.88 \times 10^{-4}\ (^{\circ}C)^{-1}$. This is approximately 40 times larger than the temperature coefficient of fused silica, which is less than $1 \times 10^{-5}\ (^{\circ}C)^{-1}$ in the visible spectrum [109].

Fluctuations in the temperature during the time required to perform the phase shift measurements must be minimized. The effect of temperature fluctuations on the measured phase shift is shown in Fig. 3.11. The plot shows the change in the maximum measured phase shift in the core of an unperturbed Corning SMF-28 fiber for two different measurements. The change in the phase shift is determined by calculating the difference between the phase shift at $\theta_f > 0$ and the phase shift at $\theta_f = 0$. In an unperturbed fiber, there should be no change in the phase shift as the measurement progresses.

The measurement labeled Meas. No. 1 in Fig. 3.11 was started one hour after the light source of the microscope was turned on. This is the typical time recommended to allow the light source to warm up and stabilize. However, the progressively larger phase shifts as the measurement progressed indicate a steady decrease in the refractive index of the index-matching oil. The measurement labeled Meas. No. 2 was started eight hours after the light source was turned on. The relative change in the phase shift remains much closer to zero than Meas. No. 1. This indicates that the refractive index of the index-matching oil, and thus the temperature, has stabilized.

Other measurements indicate that eight hours is not required for the temperature to stabilize. In general, if the retardation measurements are performed first using the BKC technique, which takes three to four hours, then the temperature will remain relatively stable for the phase shift measurement.

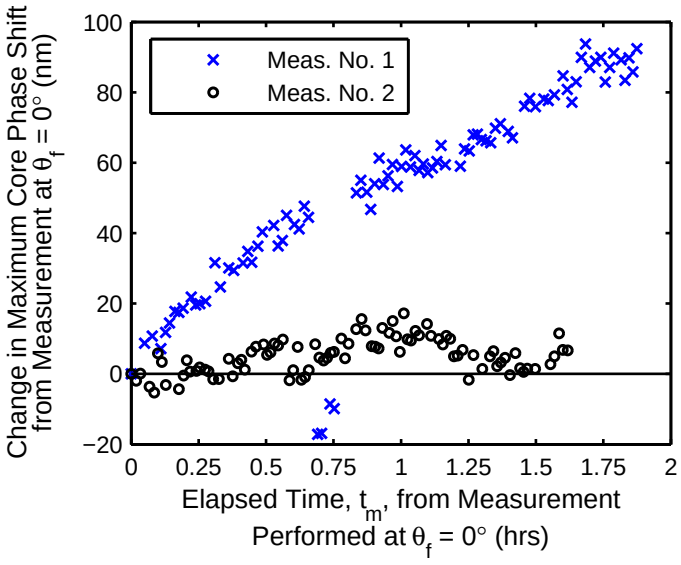

Figure 3.11: Change in the maximum core phase shift from the initial value measured at $\theta_f = 0$ deg for two measurements of an unperturbed Corning SMF-28 fiber. The x-axis indicates the elapsed measurement time, t_m, in hours. The measurement at $t_m = 0$ corresponds to $\theta_f = 0$ deg.

3.3.2 Background Measurement

There are two sources of background phase shifts. First, there are actual variations and imperfections in the imaging system that produce real background phase shifts. Second, it has been shown that noise in the images used to calculate the phase shift will produce noise-induced artifacts in the phase shift (artificial phase shifts) [110]. The real background phase shifts are characterized by performing background measurements with the fiber removed from the FOV: one before the initial fiber measurement at $\theta_f = 0$ and one after all measurements with the fiber are complete. These two background measurements are averaged and subtracted from the measurements with

the fiber to remove the real background phase shifts. Two background measurements are made to characterize better any changes that occur during the time required to make the measurements with the fiber.

The artificial phase shifts, however, vary randomly from image to image because of the random nature of image noise and they cannot be accounted for with the background measurements. The artificial phase shifts are also of low spatial frequency and cannot be filtered without simultaneously filtering the low-spatial-frequency content in the measured phase shift. Therefore, efforts must be made to reduce the image noise.

A reduction in the image noise is most readily achieved by averaging multiple frames captured by the CCD camera to create an image. The presence of the noise-induced, artificial phase shifts and the ineffectiveness of background measurements alone to remove them is shown in Fig. 3.12. On the left are phase-shift distributions calculated from images created from one frame of the CCD camera. On the right, images created from the average of 25 frames were used. The presence of background phase shifts can be seen in the measurements of the fiber (before subtracting the background measurement) in Fig. 3.12(a). The background measurement is shown in Fig. 3.12(b). After subtracting the background measurement, visible perturbations in the phase shift remained when only one frame of the CCD camera was used (left side of Fig. 3.12(c)). This indicates the presence of noise-induced, artificial phase shifts that were not characterized with the background measurement, and therefore not removed. However, when 25 frames were averaged, a more uniform phase shift was achieved after subtracting the background measurement (right side of Fig. 3.12(c)).

The relationship between the noise-induced artificial phase shifts and the number of CCD frames averaged to create an image was investigated to determine how many frames to average. The standard deviation of the phase shift in the region surrounding the fiber (surrounding-region phase shift), which indicates the uniformity, was

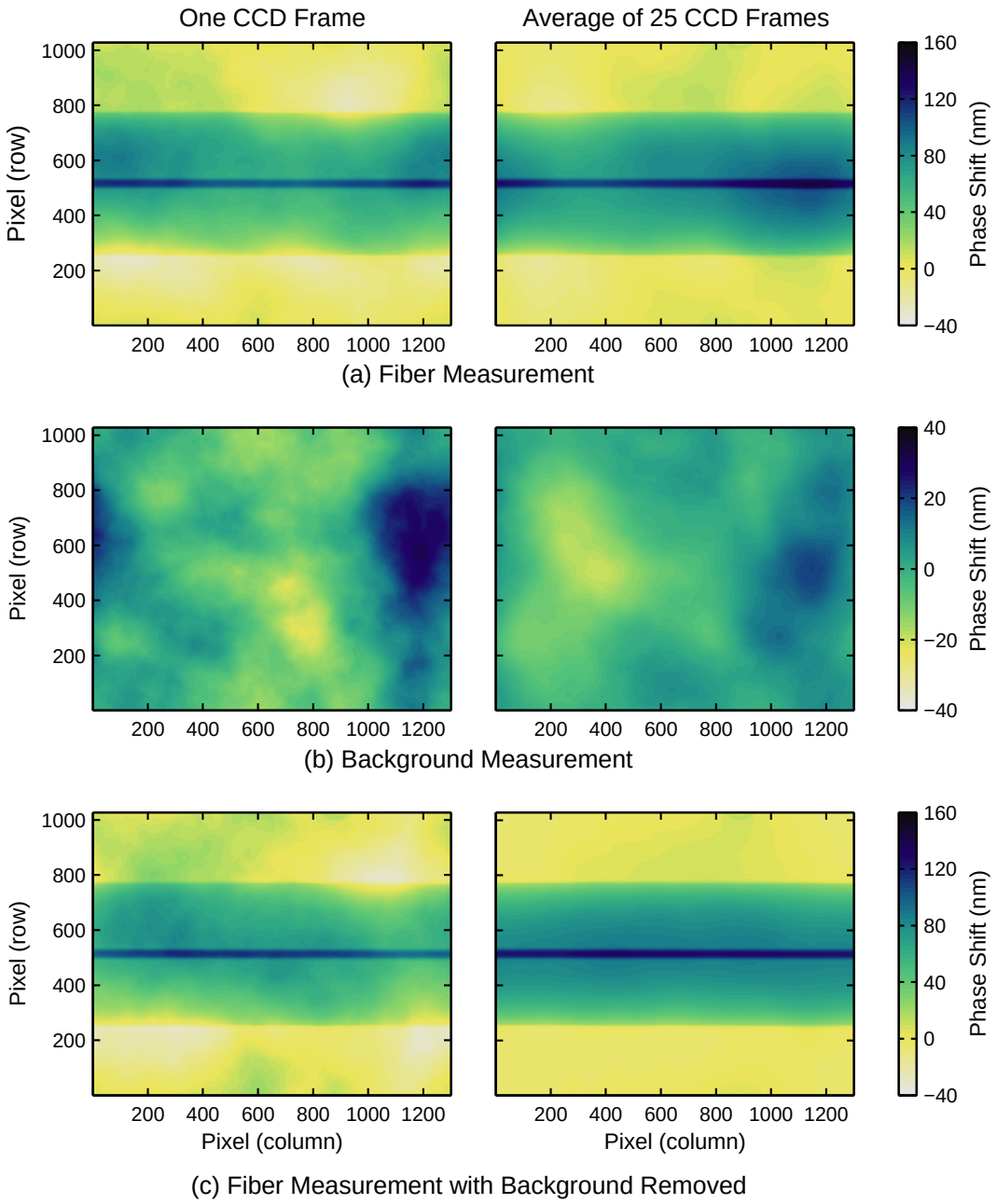

Figure 3.12: The effect of noise-induced, low-spatial-frequency artifacts on the calculated phase shift for (a) the fiber only, (b) the background measurement, and (c) the fiber with the background removed. The phase-shift distributions in the left column were calculated from images created from one frame of the CCD camera. The right column distributions were calculated from images created from the average of 25 frames. In (c), the presence of artifacts that were not characterized with the background measurement are clearly seen with only one frame, but they are greatly reduced by averaging 25 frames.

calculated for measurements made with various numbers of CCD frames averaged. Table 3.1 lists the standard deviation of the surrounding-region phase shift for various numbers of CCD frames averaged. Averaging 50 frames achieved the lowest standard deviation, and thus the most uniform surrounding-region phase shift. However, averaging more frames requires more time. The reason for the increase in the standard deviation with 100 frames averaged is unclear, however, perturbations during the time required to average 100 frames with the current CCD camera (approximately 10 seconds) may contribute to this. This tradeoff between the noise reduction and the increased time required must be analyzed for future improvements to the CCD camera. For the measurements presented in this thesis, 25 frames were averaged to create an image.

Table 3.1: Standard deviation of the surrounding-region phase shift for various numbers of CCD frames averaged.

Number of CCD Frames Averaged	Standard Deviation of the Surrounding-Region Phase Shift (nm) (at $\lambda = 546$ nm)
1	13.00
5	12.22
10	5.90
25	4.04
50	3.40
100	6.62

CHAPTER 4

MEASUREMENT APPARATUS

The measurement apparatus to implement concurrently the Brace-Köhler compensator (BKC) technique and the quantitative-phase microscopy (QPM) technique is built upon an Olympus BX60 microscope fitted with polarization microscopy components and custom components. The relevant optical components and custom components to enable partial automation and tomographic measurements of optical fibers are shown in Fig. 4.1.

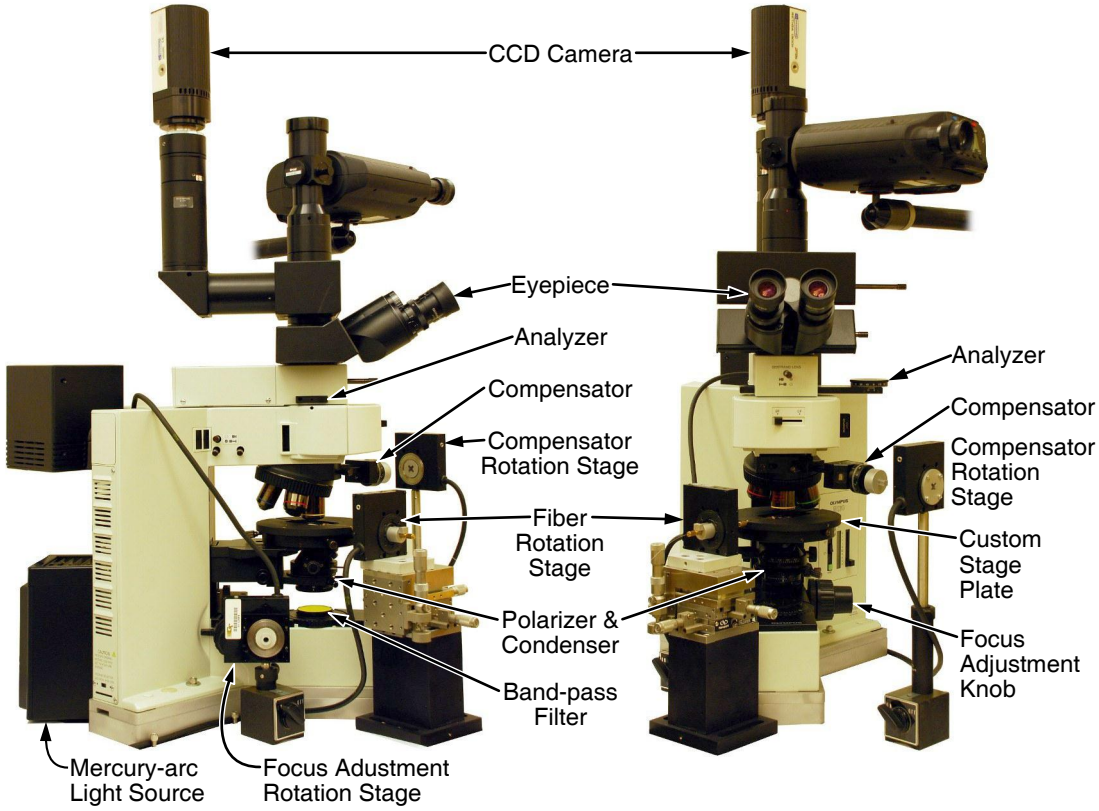

Figure 4.1: Customized Olympus BX60 Microscope.

4.1 Common Elements

4.1.1 Light Source, Polarizer and Condenser

The light source is a mercury-arc lamp mounted for transmitted-light microscopy. The mercury-arc source provides strong emission at 546 nm and is combined with a 546 nm band-pass filter (10 nm FWHM). The use of a narrow-band source with a wavelength-dependent compensator results in a broadening of the intensity dependence on the compensator angle when performing a retardation measurement. However, the retardation of the fiber is also dependent on the wavelength. The inherent canceling of the compensator-based measurement will therefore result in negligible broadening. The theoretical change in $\theta_{c,min}$ for wavelengths of 546±5 nm is less than 10^{-3} deg for typical values of the maximum retardation induced by optical fibers.

The polarizer and a strain-free condenser are integrated into one housing, enabling the precise alignment of both optical components. The adjustable numerical aperture (NA) of the condenser is set to 0.6 (80% of the objective NA) to ensure high-quality Köhler illumination when performing the retardation measurements. The NA of the condenser is set to 0.4 when performing the phase-shift measurements. This value has been determined to be optimal for the current measurement apparatus and is discussed further in Sec. 5.2.1.

4.1.2 Microscope Stage Plate

A custom microscope stage plate was designed and fabricated as part of this work to enable measurements at various angular orientations of the fiber [89]. The custom stage plate allows for the precise placement of the fiber, the index-matching oil, a microscope slide, and a coverslip within the field of view (FOV). The custom stage plate configuration is shown in Fig. 4.2. Slots in the plate allow for the placement of fiber chucks (Newport model FPH-J) on either side of the FOV. The fiber chucks are milled flat on one side to provide secure seating of the chuck into the plate and

to align the fiber. The chucks are tightened to limit the radial runout of the fiber during rotation, but they are not clamped onto the fiber to allow for smooth rotation and longitudinal motion.

Depressions in the center of the plate hold a modified 25.4-mm-square microscope slide (1 mm thick) below the fiber. Two opposing corners of the slide are trimmed as shown in Fig. 4.2 to minimize the length of the fiber that passes through the index-matching oil. Two small pieces of coated (250-µm-diameter) fiber are placed on either side of the fiber sample and a 12.5-mm-square coverslip (0.16 mm thick) is placed on top. The two small pieces of coated fiber ensure that the 125-µm-diameter fiber sample passes freely through the slide and the coverslip without making contact.

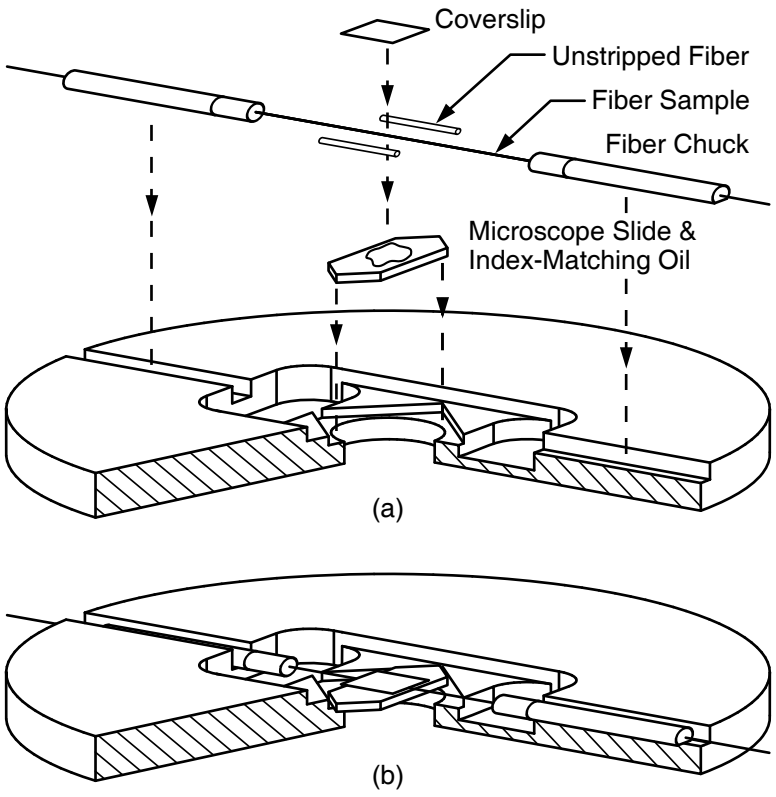

Figure 4.2: Custom microscope stage plate configuration: (a) expanded view showing the placement of the coverslip, fiber sample, coated fiber spacers, index-matching oil, and microscope slide; and (b) assembled view showing the arrangement of the components within the stage plate.

Index-matching oil is placed between the slide and the coverslip to minimize refraction from the cladding boundary. Light mineral oil (Suave-brand baby oil) provides an index of refraction between the core and the cladding indices of a Corning SMF-28 fiber. Index-matching oil from Cargille Laboratories specified to have $n_D = 1.4580$ provides an index of refraction that is approximately 1×10^{-3} below the cladding index of a Corning SMF-28 fiber at the wavelength of the filtered mercury-arc light source. Both oils are used for the measurements presented in this thesis.

4.1.3 Fiber Rotation Apparatus

The fiber sample is rotated with a computer-controlled rotation stage (Newport model SR50PP) mounted next to the microscope. The fiber is held securely in the rotation stage with a fiber chuck and a custom chuck holder as described by Bachim and Gaylord and shown in Fig. 4.3 [111]. A length of at least 15 cm of excess fiber on one side of the region to be characterized is required to secure the fiber into the rotation stage. There is no maximum or minimum length restriction on the fiber on the side opposite the rotation stage.

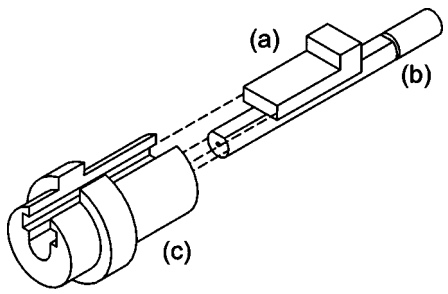

Figure 4.3: Optical fiber holder for rotation apparatus: (a) key; (b) optical fiber chuck with milled flat; and (c) chuck holder. The assembled device is inserted into the rotation stage [111].

4.1.4 Objective

A strain-free, infinity-corrected 40× (NA = 0.75) objective provides high-magnification imaging that minimizes wavefront distortion. The spatial resolution, or lateral

resolving power, of the objective combined with a condenser NA of 0.6 is 0.49 µm.

4.1.5 CCD Camera

Digital images are captured using a QImaging Retiga 1300R CCD camera configured to capture 12-bit gray-scale images. The lateral spatial resolution of the captured images is about 0.245 µm. The image resolution is smaller than the 0.49 µm spatial resolution of the imaging optics. This results in a small amount of oversampling in each pixel, however, this is permissible because the BKC technique and the QPM technique both rely on detecting relative intensities rather than absolute intensities.

Binning, or combining blocks of pixels, can be used to reduce the noise in the captured images. However, binning also increases the spatial resolution. Because of this tradeoff, the CCD camera is set to capture images at its full resolution of 1300×1030 pixels. This provides the most detailed image data available and binning can be performed later when the images are analyzed. To determine whether or not to perform binning while analyzing the images, the standard deviation of the retardation and the phase shift in the region surrounding the fiber (surrounding-region retardation and phase shift) was determined for measurements performed on an unperturbed Corning SMF-28 fiber. The surrounding-region retardation and phase shift indicate the level of noise in the measurement and provide an estimate of the resolution.

The standard deviation in the surrounding-region retardation decreased from 0.025 nm when no binning was performed to 0.013 nm (at $\lambda = 546$ nm) when two-by-two blocks of pixels were combined. This 48% improvement indicates that the retardation resolution is improved by binning the images. The surrounding region phase shift however was not affected by binning. This indicates that either (1) the noise reduction obtained by averaging 25 frames from the CCD camera is not noticeably improved by binning or (2) the noise-induced phase-shift artifacts are negligible

compared to background phase shifts that are not characterized and removed by the background measurement. Because of the improvement in the retardation measurements, the residual-stress distributions and the refractive-index distributions reported in this thesis were determined by binning two-by-two blocks of pixels. In addition to improving the noise in the retardation, binning matches the spatial resolution of the images to the theoretical spatial resolution of the imaging optics.

4.2 Elements and Issues Specific to the BKC Technique

4.2.1 Polarizer and Analyzer

The analyzer must be inserted and crossed with the polarizer while images are being captured. However, as discussed in Sec. 2.1.2.3, checking the focus of the fiber is more efficiently done with the analyzer removed from the FOV. Removing the analyzer provides significantly more light to the CCD and enables the real-time monitoring of the focus and the position of the fiber. Furthermore, with the analyzer removed, the fiber appears transparent except at the boundaries between regions with different indices of refraction. The observation of the effects of refraction and diffraction at these boundaries enables the rapid, qualitative determination of the focus of the fiber. The analyzer is therefore removed from the optical path between measurements to check the focus and the position of the fiber. The compensator remains in the optical path while checking the focus and has no noticeable effect.

4.2.2 Compensator

An Olympus U-CBR2 compensator with a retardation of 21.54 nm at the wavelength of the filtered mercury-arc source (546 nm) is used for the measurements performed on optical fibers. A custom coupling device was designed and fabricated as part of this work to enable the automated rotation of the compensator with a computer-controlled rotation stage (Newport model SR50PP) [89]. The coupling device, shown in Fig. 4.4, mates the rotation stage to the compensator rotation dial and features a sliding fit

between the square peg and the square hole to allow for a slight misalignment between the rotation axis of the stage and the rotation axis of the dial. This ensures that minimal stresses are applied to the compensator housing.

A backlash between the rotation stage and the actual compensator angular orientation is created by: (1) the loose fit of the coupling device and (2) the internal compensator rotation mechanism. To achieve accurate positioning of the compensator during full-field measurements, the compensator is always rotated in the counter-clockwise direction (positive direction as indicated in Fig. 2.1) from θ_1 to θ_N. The compensator is then reset between measurements using a clockwise (negative) rotation to an angle less than θ_1 followed by a counter-clockwise (positive) rotation to θ_1. A negative rotation of 1 deg beyond θ_1 will ensure that the backlash is compensated for.

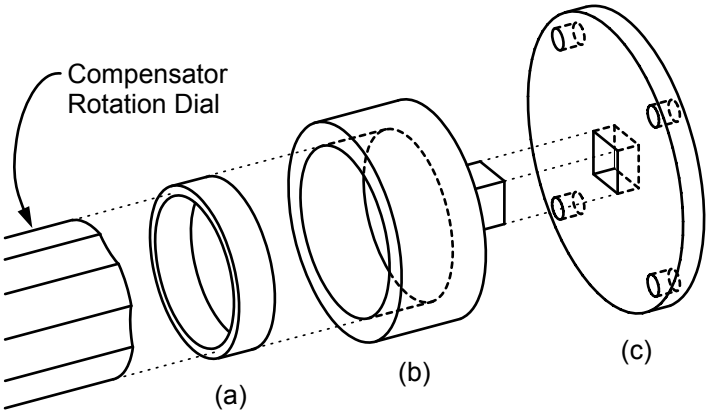

Figure 4.4: Coupling device: (a) 1.5-mm-thick rubber annular ring; (b) compensator-dial gripping cup with square peg; and (c) rotation-stage mount with square hole. Also shown for reference is the compensator rotation dial. The rubber annular ring (a) lines the inside of the gripping cup (b). The rotation-stage mount (c) bolts to the rotating barrel of the stage. The square peg on (b) and the square hole in (c) allow for the coupling of the stage to the dial.

4.3 Elements and Issues Specific to the QPM Technique

4.3.1 Polarizer

The polarizer transmission direction is oriented at 45 deg relative to the longitudinal axis of the fiber as shown in Fig. 2.1. Therefore, the light transmitted through the birefringent fiber is split between the transverse and longitudinal indices. The accuracy of the QPM technique is not sufficient to detect the difference in the phase shift induced by the two orthogonal polarizations. Therefore, a combination of the transverse and longitudinal indices is detected.

4.3.2 Defocusing Apparatus

Automated focusing and defocusing of the fiber is achieved by rotating the fine focus knob on the microscope with a computer-controlled rotation stage (Newport model SR50PP) and a custom coupling device to mate the rotation stage to the focus knob. The coupling device consists of a rotating drum mounted directly to the rotating barrel of the stage. The rotation axis of the stage and the longitudinal axis of the drum are collinear. The cylindrical surface of the drum is coupled to the cylindrical surface of the compliant rubber cover of the focus knob by friction. This is similar to the coupling of two parallel gears. To avoid backlash-induced errors, the microscope stage is moved in one direction from the negative defocus position ($z_{m0} - \delta z_m$) to the in-focus position (z_{m0}) to the positive defocus position ($z_{m0} + \delta z_m$).

CHAPTER 5

PRELIMINARY MEASUREMENTS AND PERFORMANCE

5.1 Residual-Stress Characterization

5.1.1 Unperturbed Fiber

The measurement procedure and the apparatus for the Brace-Köhler compensator (BKC) technique were updated after the initial results were reported in [88] and [89]. Therefore, an unperturbed Corning SMF-28 fiber was characterized again to verify the initial measurements and to quantify the improvements.

The axial component of the residual-stress distribution (RSD) in an unperturbed Corning SMF-28 fiber was characterized with the procedure and apparatus described in Chapters 2 and 4. A typical cross-sectional RSD is shown in Fig. 5.1. Positive values of the axial stress indicate tension and negative values indicate compression.

The distribution is azimuthally symmetric as expected. Relatively high tensile stresses exist around the exterior of the cladding with an azimuthally averaged peak value of +10.2 MPa. These tensile stresses decrease monotonically approaching the core of the fiber and become compressive at approximately 25 µm from the center of the fiber. Peaks of maximum compressive stress (minimum overall stress) with an azimuthally averaged value of −5.2 MPa are visible around the core of the fiber at the boundary between the core and the cladding (core-cladding boundary). This result agrees well with the initial measurement reported in [88] and [89] and other published radial profiles of the axial stress [41, 46, 112] and cross-sectional RSDs [14] in the same type of fiber.

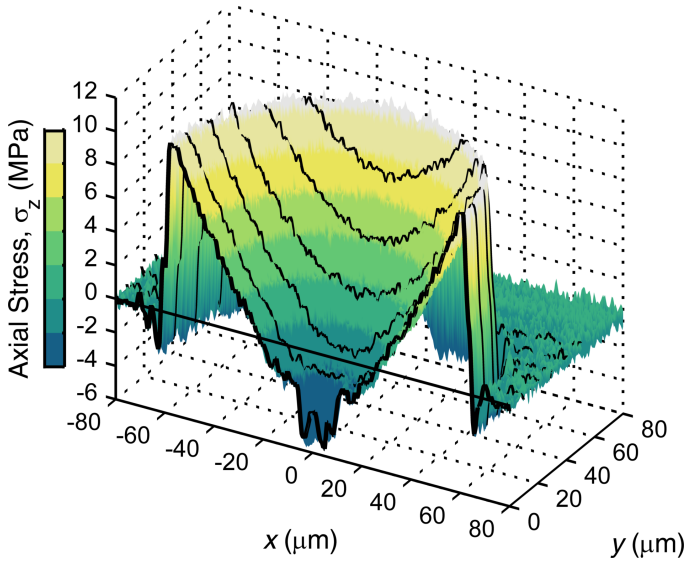

Figure 5.1: Plot of a typical cross-sectional axial stress distribution in an unperturbed Corning SMF-28 fiber. Line profiles are shown for $x = 0$, 10, 20, 30, 40, and 50 μm.

The total residual stress in the fiber is composed of thermally induced (thermal) stresses and mechanically induced (mechanical) stresses [5]. The relative contributions of these two types of stress are shown in Fig. 5.2. The thermal stresses result from the cooling of the fiber during the drawing (manufacturing) process combined with spatial differences in the viscosity and the thermal expansion coefficient within the fiber. In a conventional (germanium-doped core, pure-silica cladding) telecommunications fiber, the cladding has a higher viscosity (thicker) and solidifies at a higher temperature than the core. As the fiber cools, the cladding solidifies before the core. The core, however, has a higher thermal expansion coefficient because of the germanium doping. Therefore, large tensile stresses form in the core as it cools but is restricted from contracting because of bonding to the surrounding solidified cladding. A representative thermal stress profile is shown in Fig. 5.2(a).

Mechanical stresses result from the forces placed on the fiber during the drawing process combined with spatial differences in the viscosity. In a conventional fiber, the draw tension is primarily sustained in the high-viscosity (thick) molten glass of

the pure-silica cladding as it solidifies. The low-viscosity (thin) molten glass in the germanium-doped core solidifies after the cladding, and thus it receives relatively small amounts of the draw tension. When the drawing tension is removed from the fiber and mechanical equilibrium is established, the tensile stresses in the cladding partially relax and the stresses in and around the core of the fiber become compressive. A representative mechanical stress profile is shown in Fig. 5.2(b).

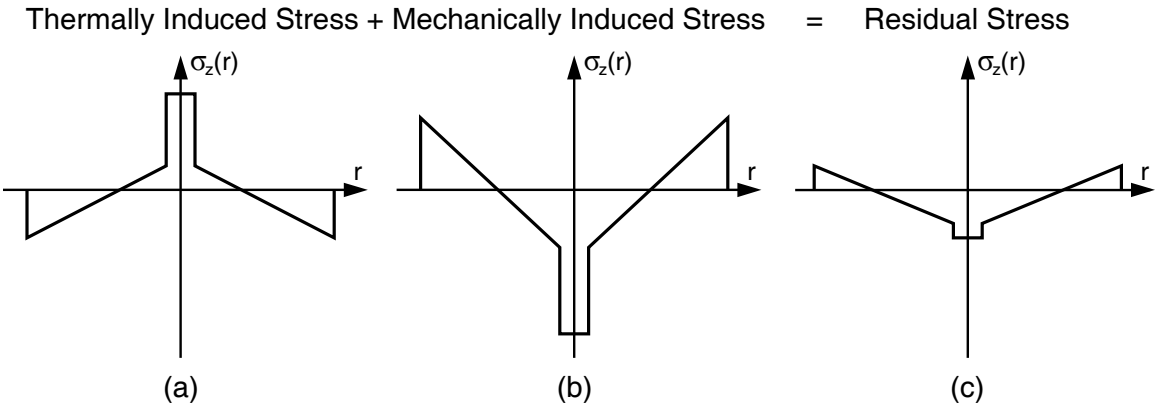

Figure 5.2: Relative contributions of thermally induced stress (a) and mechanically induced stress (b) to the total residual stress (c) in a conventional telecommunications fiber.

The contributions of both thermal and mechanical stresses are visible in Fig. 5.1. The presence of mechanical stress is indicated by (1) the overall shape of the RSD and (2) the peak in the compressive stress at the core-cladding boundary. The overall shape of the RSD as seen in the radial profile in the cut through the surface plot in Fig. 5.1 is similar in functional form to the mechanical stress profile in Fig. 5.2(b). The peak in the compressive stress (minimum overall stress) at the core-cladding boundary indicates the presence of OH impurities introduced during the manufacture of the fiber preform [113]. The OH impurities at the boundary lower the viscosity of the molten silica glass. Therefore, similar to the core, the core-cladding boundary region sustains a relatively small amount of the draw tension. When the draw tension is removed and mechanical equilibrium is established, compressive stresses are formed

in the boundary region.

The presence of thermal stress is indicated by the higher level of stress in the core relative to the surrounding core-cladding boundary. The relatively high thermal expansion coefficient in the germanium-doped core results in the contraction of the glass as it cools. As the core contracts, tensile stresses form as it conforms to the surrounding solidified cladding [5]. These tensile thermal stresses counteract the compressive mechanical stresses, resulting in the higher (less compressive) level of stress in the core.

5.1.1.1 Average Radial Profile of the Axial Stress

The azimuthal symmetry of the RSD permits the averaging of radial profiles at various angles to reduce noise and enable further analysis of the detailed features in the RSD. Radial profiles at azimuthal angles from 0 to 178 deg were extracted in 2 deg increments and averaged to produce an average axial stress profile. The average axial stress profile in the unperturbed fiber is shown with the solid line in Fig. 5.3.

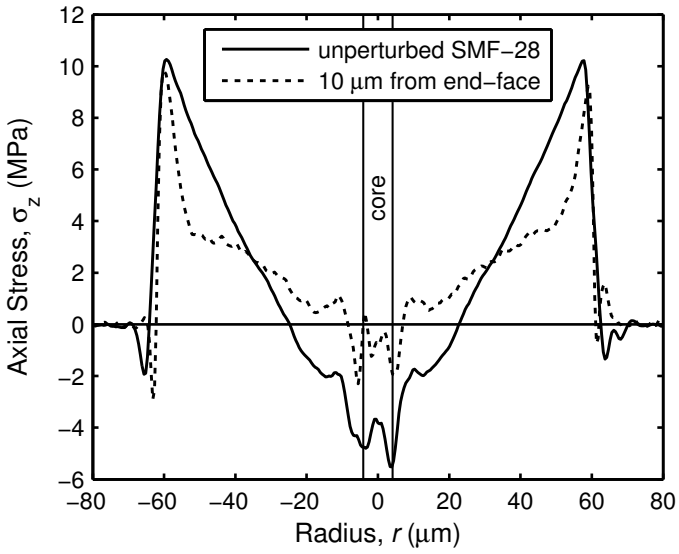

Figure 5.3: Average radial profile of the RSD in the unperturbed Corning SMF-28 fiber (solid line) and the RSD 10 µm from the cleaved end-face (dotted line). Both profiles indicate peaks of compressive stress (minimum overall stress) near the boundary between the core and cladding.

The contributions of mechanical and thermal stress described previously are seen clearly in the average profile. The peaks in the compressive stress (minimum overall stress) at the core-cladding boundary are readily visible, as is the higher level of stress in the core relative to the surrounding core-cladding boundary.

5.1.1.2 Mean Axial Stress

The cross-sectional RSD and the average stress profile both reveal a net tensile stress in the fiber. To analyze the origin of this net tensile stress, the mean axial stress, $\overline{\sigma}_z$, in the fiber cross section is evaluated. The mean axial stress is determined by

$$\overline{\sigma}_z = \frac{\int_0^{2\pi}\int_0^a \sigma_z(r,\theta)\, r\, \mathrm{d}r\, \mathrm{d}\theta}{\int_0^{2\pi}\int_0^a r\, \mathrm{d}r\, \mathrm{d}\theta}, \tag{5.1}$$

where a is the radius of the cladding. The mean axial stress in the unperturbed Corning SMF-28 fiber is +4.70 MPa, indicating a mean axial tension in the fiber. However, in the absence of external forces, the mean stress in the fiber should be zero.

The apparent non-zero mean stress has been hypothesized to be caused by the presence of inelastic strain birefringence that exists in the fiber along with stress-induced birefringence, which can be equivalently referred to as elastic strain birefringence. These two types of birefringence arise in optical fibers because of separate effects that occur during the drawing process, but their atomic-level origin is the same.

5.1.1.3 Origin of Fiber Birefringence

The molecular structure of the silica glass used in a conventional optical fiber is naturally isotropic. Birefringence arises in optical fibers because of two distinct effects the glass is strained [7, 94]. First, the lattice effect occurs when atoms are displaced and the structure of the glass becomes anisotropic. Second, the atomic effect occurs when the electron distribution of a displaced atom is distorted. The birefringence

that results in a strained optical fiber can be explained by considering induced dipole moments in each atom and the interaction among these dipoles that occurs between neighboring atoms (typically oxygen atoms) in the glass [114, 115].

With no strain present in the glass, the atoms are effectively equally spaced and their electron distributions are undistorted. This can be represented in an overly simplified way as a cubic lattice ($a = b = c$) of atoms with spherical electron distributions (hatched area) as shown in the upper part of Fig. 5.4(b).

A positive strain in the glass, defined as an elongation in the longitudinal (z) direction, can be represented by a tetragonal lattice with $c > a = b$ as shown in the upper part of Fig. 5.4(a). In this state, considering only the lattice effect, planes of atoms perpendicular to the axis of the fiber (z) are sufficiently far apart that the dipole interaction between planes is negligible. Although not represented in Fig. 5.4, these planes are oriented normal to the page and can be considered as non-interacting planes. For an electric field in the z direction there is a strong depolarizing effect; the dipole field of each atom reduces the total field (applied plus induced) at the four nearest-neighbor atom sites. This reduces the electric susceptibility and thus the permittivity and thus the refractive index of the field polarized in the z direction, n_z. This reduction in n_z due to the lattice effect is indicated by the downward facing arrow labeled L (for lattice) in the lower part Fig. 5.4(a). Within a plane however, the dipoles interact strongly. For an electric field perpendicular to the z direction there is a strong polarizing effect; the dipole field of each atom increases the total field at the neighboring atom sites. This increases the refractive index of the field polarized perpendicular to the z direction, $n_\perp$. This increase in $n_\perp$ due to the lattice effect is indicated by the upward facing arrow labeled L in the lower part Fig. 5.4(a).

The atomic effect in the positive strain case acts in opposition to the lattice effect. The electron distributions elongate in the z direction as shown in the hatched regions in the upper part of Fig. 5.4(a). This increases the polarizability of the

atoms in the z direction and effectively increases the dipole interaction between the previously non-interacting planes. The electron distributions contract perpendicular to the z direction and effectively decrease the dipole interaction between atoms within a plane. This leads to an increase in n_z and a decrease in $n_\perp$ as indicated with the arrows labeled A (for atomic) in the lower part of Fig. 5.4(a). The combined lattice and atomic effects lead to a decrease in both n_z and $n_\perp$, but to a greater decrease in $n_\perp$. Thus, the net birefringence is $n_z - n_\perp > 0$ and the fiber behaves like a positive uniaxial material.

A negative strain in the glass, defined as a compression in the longitudinal (z) direction, can be represented by a tetragonal lattice with $c < a = b$ as shown in Fig. 5.4(c). In this state, considering only the lattice effect, dipoles in a chain oriented along the axis of the fiber interact strongly, but neighboring chains are sufficiently far apart that interaction is negligible. The glass therefore consists of non-interacting chains (rather than planes). Opposite to the effect of the non-interacting planes, there is a strong polarizing effect for an electric field in the z direction (along a chain) and a strong depolarizing effect for an electric field perpendicular to the z direction. This increases n_z and decreases $n_\perp$ as indicated by the arrows labeled L in the lower part Fig. 5.4(c).

The atomic effect in the negative strain case again acts in opposition to the lattice effect. The electron distributions now compress in the z direction and elongate in the perpendicular to the z direction. These changes effectively decrease the dipole interaction within a chain and increase the dipole interaction between the previously non-interacting chains. This leads to a decrease in n_z and an increase in $n_\perp$ as indicated with the arrows labeled A in the lower part of Fig. 5.4(c). The combined lattice and atomic effects lead to an increase in both n_z and $n_\perp$, but to a greater increase in $n_\perp$. Thus, the net birefringence is $n_z - n_\perp < 0$ and the fiber behaves like a negative uniaxial material.

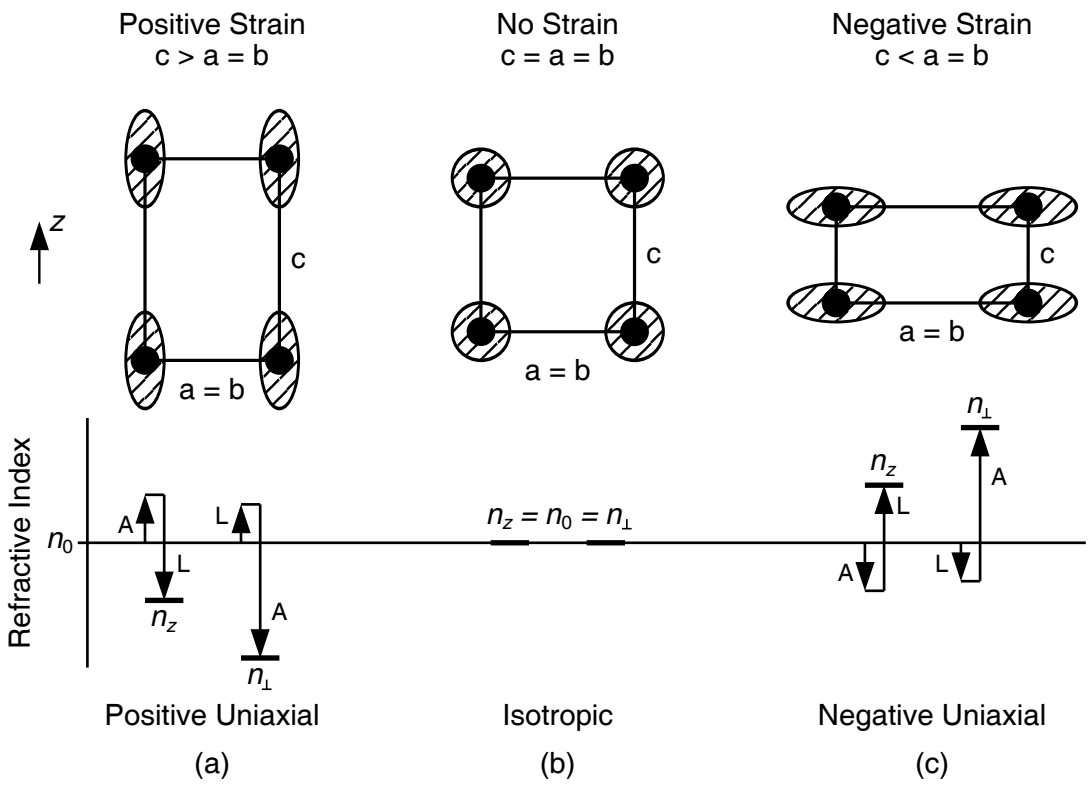

Figure 5.4: Physical depiction of the effect of strain in an optical fiber: (a) positive strain; (b) isotropic (no strain); and (c) negative strain. The hatched regions indicate the electron distribution around individual atoms (dots). The charts below the atomic diagrams indicate the relative contributions of the lattice effect (L) and the atomic effect (A) to the changes in the refractive index for an electric field polarized in the z direction, n_z, and a field polarized perpendicular to z, $n_\perp$.

5.1.1.4 Types of Fiber Birefringence

Stress-induced birefringence (or elastic strain birefringence) and inelastic strain birefringence are both present in optical fibers. Radial profiles of these two types of birefringence and how they contribute to the total fiber birefringence are shown in Fig. 5.5. Stress-induced birefringence arises because residual stresses remain in the fiber after it is drawn and without the presence of externally applied forces [5]. The glass in a fiber at room temperature behaves elastically, and thus the residual stresses create strains and the resulting stress-induced birefringence. Tensile (positive) residual stresses create a positive strain and thus a positive birefringence. Compressive

(negative) residual stresses create a negative strain and thus a negative birefringence. Therefore, the radial profile of stress-induced birefringence, shown in Fig. 5.5(a), is proportional in magnitude to the residual stress profile (Fig. 5.2).

Inelastic strain birefringence, shown in Fig. 5.5(b), is hypothesized to result from frozen-in viscoelasticity [5, 116]. Viscoelasticity refers to the time- and temperature-dependent relaxation, or contraction, of the molten glass during the drawing process. Frozen-in viscoelasticity refers to an incomplete contraction of the glass during the drawing process. In general, while the glass is molten, and thus viscoelastic, the glass contracts more in the transverse direction and less in the axial direction because of the draw tension. The glass then solidifies with a positive strain and thus a positive birefringence. This strain is frozen into the glass structure independent from the residual stresses that exist and is thus referred to as inelastic strain birefringence [5].

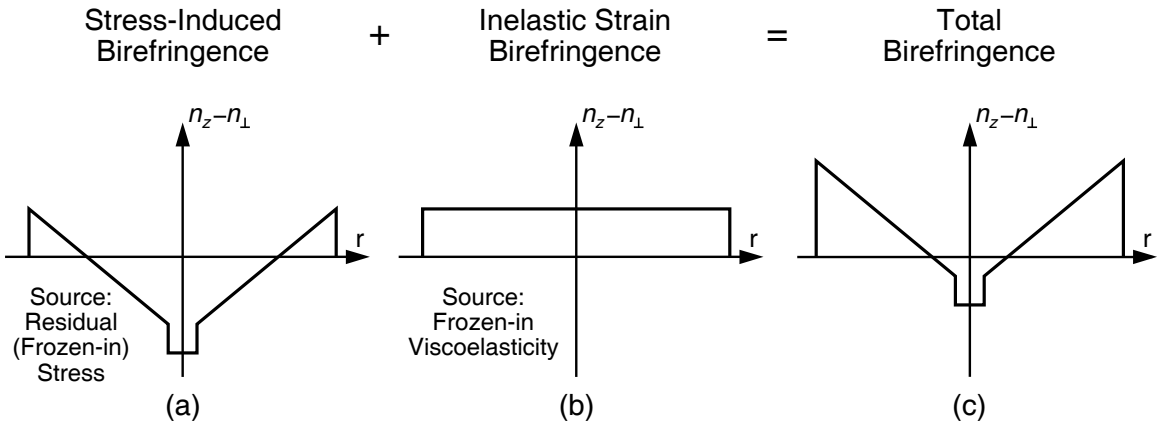

Figure 5.5: Types of birefringence present in a conventional telecommunications fiber: (a) Stress-induced birefringence; (b) inelastic strain birefringence; and (c) total birefringence. The small inset lattice structures show crystallographic representations of positive (top inset) and negative (bottom inset) birefringence.

5.1.1.5 Apparent Non-Zero Mean Stress

The apparent non-zero mean stress was measured in the unperturbed fiber because both types of birefringence were characterized with the BKC measurement technique (or any photoelastic technique). As discussed in Sec. 2.2.1, the measured retardation

in the fiber is due to birefringence. The birefringence is then related to the stress through the stress-optic law. However, the stress-optic law is only valid for stress-induced birefringence. The presence of inelastic strain birefringence also enters into the measured retardation, and thus it affects the calculated stress. The apparent mean axial tension in the unperturbed fiber is due to the measurement of not only the stress-induced birefringence, but also the inelastic strain birefringence.

Durr *et al.* showed that if the inelastic strain is assumed to be spatially uniform throughout the fiber, then its value can be determined experimentally from the measured mean axial stress [117]. The inelastic strain determined in this way agreed with the predicted inelastic strain for fibers drawn with various draw tensions. For this reason, the inelastic strain birefringence profile in Fig. 5.5(b) is shown as spatially uniform. This suggests that the actual residual axial stress in an unperturbed fiber can be determined by subtracting the mean axial stress from the measured axial stress.

5.1.2 Cleaved Fiber

The effect of cleaving the optical fiber was investigated by characterizing the RSD near the cleaved end-face of a Corning SMF-28 fiber. The axial component of the cross-sectional RSD 10 μm from the end-face of the fiber is shown in Fig. 5.6. For comparison to the RSD in the unperturbed fiber (Fig. 5.1), the same maximum and minimum axial stress values are used to define the axial stress scale.

The accuracy of the RSD was degraded because of diffraction from the end-face, scattering from a particle on the end-face, and scattering from cleave imperfections. Despite the artifacts produced by this scattering, reduced levels of stress are apparent throughout the cross section when compared to the unperturbed fiber. The stress near the cleaved end-face appears to be shifted towards equilibrium (zero) relative to the unperturbed fiber.

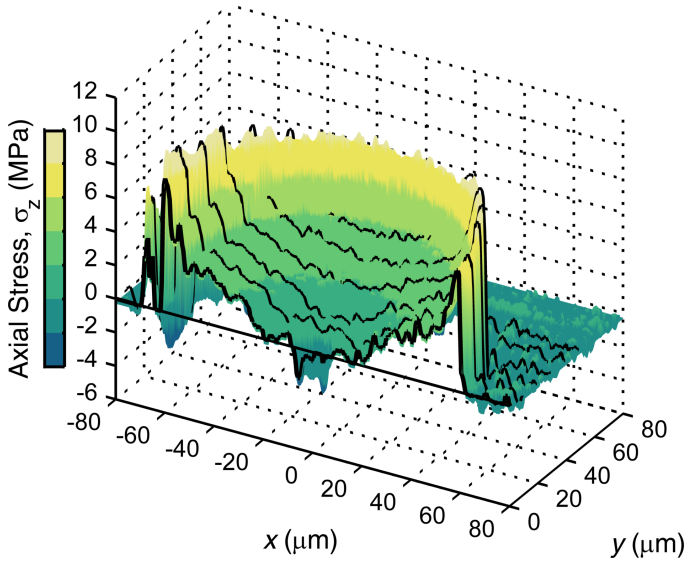

Figure 5.6: Plot of the axial component of the cross-sectional RSD 10 µm from the cleaved end-face of a Corning SMF-28 fiber. Line profiles are shown for x = 0, 10, 20, 30, 40, and 50 µm. For comparison with the unperturbed Corning SMF-28 fiber, the range of axial stress values shown is identical to the range in Fig. 5.1. When compared to the unperturbed fiber, stress relaxation is evident.

5.1.2.1 Average Radial Profile of the Axial Stress

Similar to the unperturbed fiber, the azimuthal symmetry of the RSD permits the averaging of radial profiles at various angles to reduce noise and enable further analysis of the detailed features in the RSD. The average axial stress profile 10 µm from the end-face is shown with the dotted line in Fig. 5.3. When compared to the average stress profile in the unperturbed fiber, two significant changes are present in the profile near the end-face. First, except for at the outer edge of the cladding, the tensile stresses are relaxed (reduced) in the outer cladding from a radius of 30 µm outward. Second, inside 30 µm, the stresses are shifted upwards, becoming more tensile relative to the unperturbed fiber.

These changes are indicative of partial mechanical stress relaxation near the cleaved end-face. Partial mechanical stress relaxation is shown in Fig 5.7. The thermal stress profile, (a), is assumed to be unaffected by the cleaving process. The dotted line in (b) indicates a shift in the mechanical stress profile towards equilibrium (zero).

The dotted line in (c) is the resulting total residual stress profile. The relative shift in the residual stress profile (c) is similar to average measured profile near the cleaved end-face shown in Fig. 5.3. The measured profiles in Fig. 5.3 appear more tensile (shifted upward) relative to the profiles in Fig 5.7(c) because of the overall positive mean stress caused by the presence of inelastic strain birefringence.

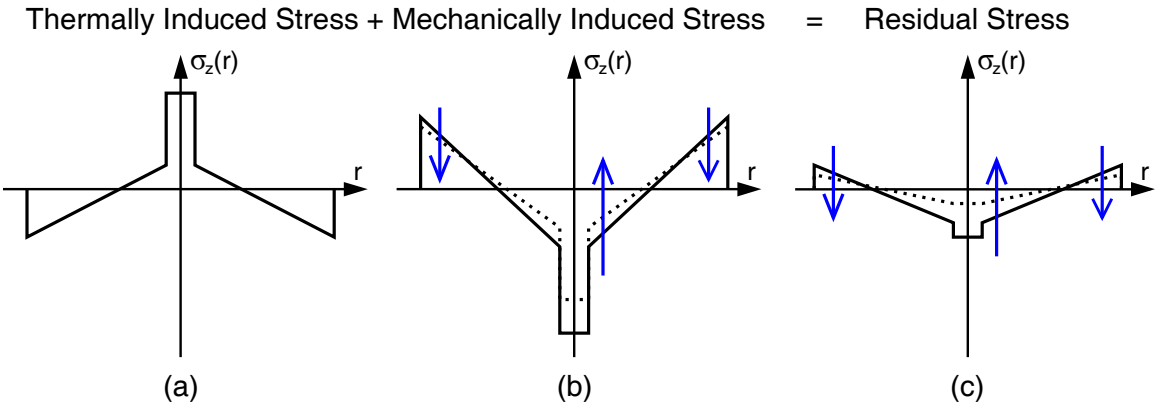

Figure 5.7: Relative contributions of thermally induced stress (a) and mechanically induced stress (b) to the total residual stress (c) in an unperturbed (solid line) and cleaved (dotted line) conventional telecommunications fiber. The arrows indicate the effect of the stress relaxation near the cleaved end-face.

5.1.2.2 Mean Axial Stress

The mean axial stress inside the cleaved fiber was evaluated to investigate the presence of inelastic strain birefringence. The mean axial stress for various cross sections along the fiber axis is shown in Fig. 5.8. The mean axial stress was calculated using Eq. (5.1) as a function of the distance from the cleaved end-face, z, where $z = 0$ is the position of the end-face. Shown for comparison is the mean axial stress of +4.70 MPa in the unperturbed fiber. For distances greater than 40 µm from the end-face, there is no significant reduction in the mean axial stress. However, from $z = 40$ µm towards the end-face, the mean axial stress drops exponentially to a value of +1.13 MPa at $z = 0$. The decreased mean axial stress in the fiber near the end-face indicates a decrease in the inelastic strain birefringence of the fiber. This suggests that cleaving reduces the

inelastic strains induced during manufacturing because of frozen-in viscoelasticity. However, the true extent of the relaxation of the residual stresses and the frozen-in viscoelasticity is not known with certainty because of degradation of the retardation measurements within 5 µm of the end-face. The diffraction from the end-face and the presence of dust particles and cleave imperfections reduced the accuracy of the retardation measurements and the calculated RSDs near the end-face.

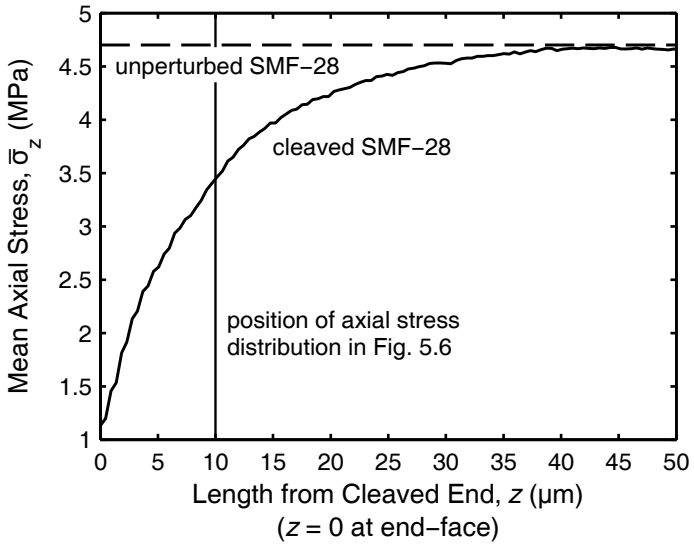

Figure 5.8: Mean axial stress inside the fiber at various lengths from the cleaved end-face of the Corning SMF-28 fiber (solid curve). For comparison, the mean axial stress inside the unperturbed Corning SMF-28 fiber is shown (dashed line).

5.1.3 Fiber Exposed to CO_2-Laser Radiation

The effect of exposing a fiber to CO_2-laser radiation was investigated by characterizing the cross-sectional RSD in a single period of an LPFG fabricated in a Corning SMF-28 fiber. The LPFG was fabricated by periodically exposing the fiber from one side to focused pulses CO_2-laser radiation with a wavelength of 10.59 µm [76]. The characterized period of the LPFG was exposed for 220 ms with a laser power of 5.75 W and a focused beam diameter of 140 µm (373.5 W/mm^2). The axial component of the cross-sectional RSD in the center of the region exposed to the laser radiation is

shown in Fig. 5.9. The two-dimensional pseudo-color plot in Fig. 5.9(a) shows the azimuthally asymmetric nature of the RSD. This azimuthal asymmetry is expected as a result of the one-sided exposure to the laser radiation. The dot-dashed center line indicates the radial direction that defines a line of approximate mirror symmetry. This indicates the direction of the exposure to the laser. The three-dimensional surface plot in Fig. 5.9(b) shows the magnitudes of the axial stress. The cut through the surface at $y = 0$ is along the dot-dashed center line in Fig. 5.9(a).

5.1.3.1 Determination of Direction of Exposure

It is difficult to determine precisely the direction of the exposure when performing a measurement. In general, when the fiber is characterized, the direction of the exposure is at an unknown azimuthal angle. Therefore, a procedure was developed to determine the direction from a measured RSD. The procedure uses the approximate mirror symmetry of the RSD about a radial line in the direction of the exposure. The mirror symmetry is due to (1) the inherent symmetry in the fiber geometry about a radial line passing through the center and (2) the use of a focused CO_2 laser beam that is centered in the transverse direction of the fiber.

The azimuthal orientation of the radial line that defines the mirror symmetry (mirror line) was determined for the RSD by performing the following procedure at various angular orientations: (1) opposite halves of the RSD were determined, (2) one half of the RSD was mirrored and subtracted from the other, and (3) the absolute values of the subtracted halves were summed. This procedure is illustrated for two angular orientations in Fig. 5.10. The smaller the sum of the absolute value of the subtracted halves, the greater their symmetry. The azimuthal angle at which the sum is minimized defines the mirror line of the distribution, and thus, the direction of the exposure. The direction of the exposure in the RSD shown in Fig. 5.9(a) is oriented at an azimuthal angle of -8 deg with respect to the x axis.

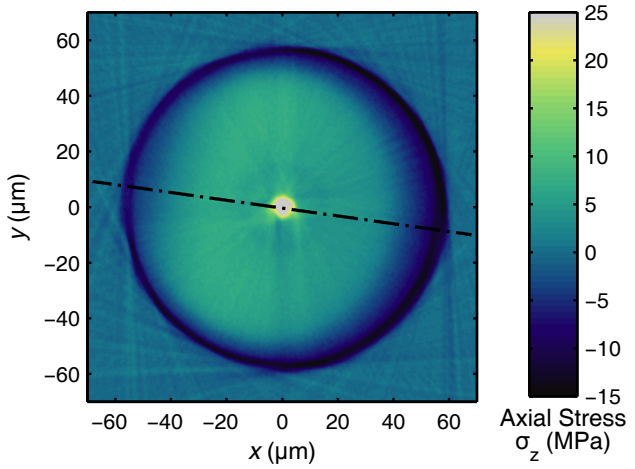

(a)

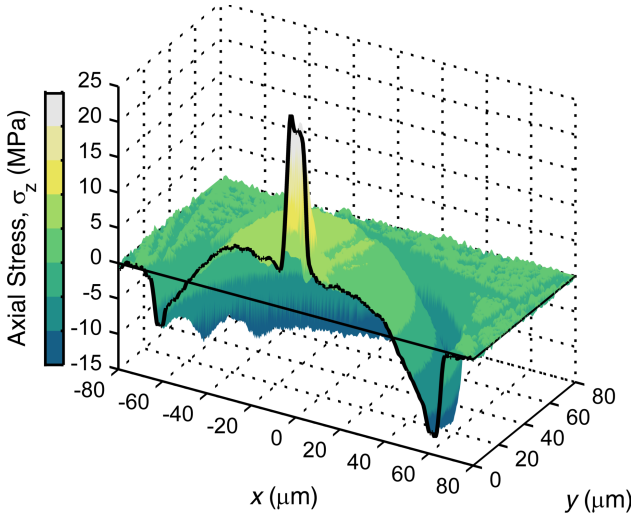

(b)

Figure 5.9: Plots of the axial component of the cross-sectional RSD at the center of a region of Corning SMF-28 fiber exposed to CO_2-laser radiation: (a) two-dimensional pseudo-color plot; and (b) three-dimensional surface plot. The dot-dashed center line in (a) indicates the radial direction with the greatest asymmetry.

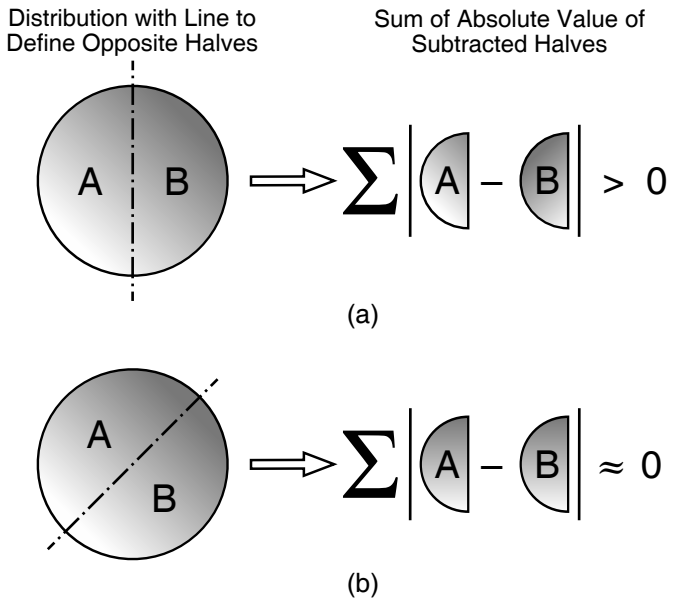

Figure 5.10: Procedure for determining the angular orientation of the mirror line of an RSD. The procedure is illustrated for two angular orientations of the line that defines opposite halves: (a) an orientation that does not define the mirror line and (b) an orientation that approximately defines the mirror line of the distribution.

5.1.3.2 Comparison to Unperturbed Fiber

The radial profile of the axial stress along the direction of the exposure is shown with the solid line in Fig. 5.11. Also shown for comparison is a typical radial profile from the unperturbed fiber. Significant changes are seen in the RSD present in the exposed fiber when compared with the unperturbed fiber. The tensile stresses around the cladding of the fiber became compressive after the exposure to the CO_2 laser. Conversely, the compressive stresses in the core of the unperturbed fiber became strongly tensile in the exposed fiber.

These changes in the RSD are consistent with mechanical stress relaxation by laser-induced heating [22, 118, 119]. This is similar to the relaxation seen near the cleaved end-face, however, the laser-induced relaxation, which is shown in Fig 5.12, is much more complete. The thermal stress profile, (a), is again assumed to be unaffected [22]. The dotted line in (b) indicates an almost complete shift in the mechanical stress profile towards equilibrium (zero). The dotted line in (c) is the

resulting total residual stress profile. The relative shift in the residual stress profile (c) is similar to the measured profile in the exposed fiber shown in Fig. 5.11. Especially evident in Fig. 5.11 is the relaxation of the mechanically induced compression in and around the core of the unperturbed fiber, thus exposing the thermally induced tension in the germanium-doped core.

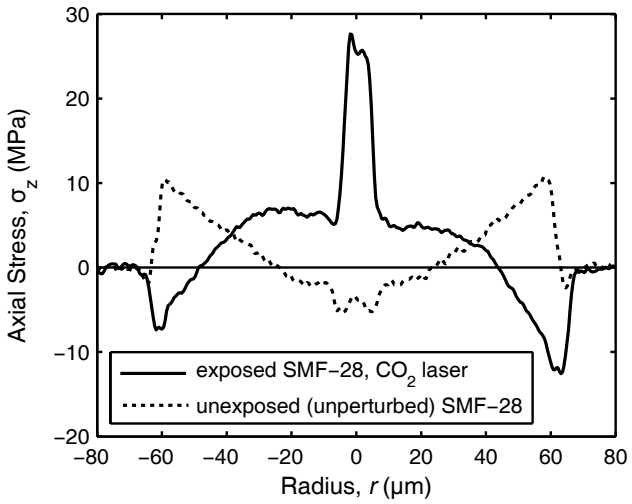

Figure 5.11: Radial profile of the axial stress along the dot-dashed center line in Fig. 5.9(a) (solid line) and a typical radial profile of the axial stress in the unperturbed Corning SMF-28 fiber (dotted line).

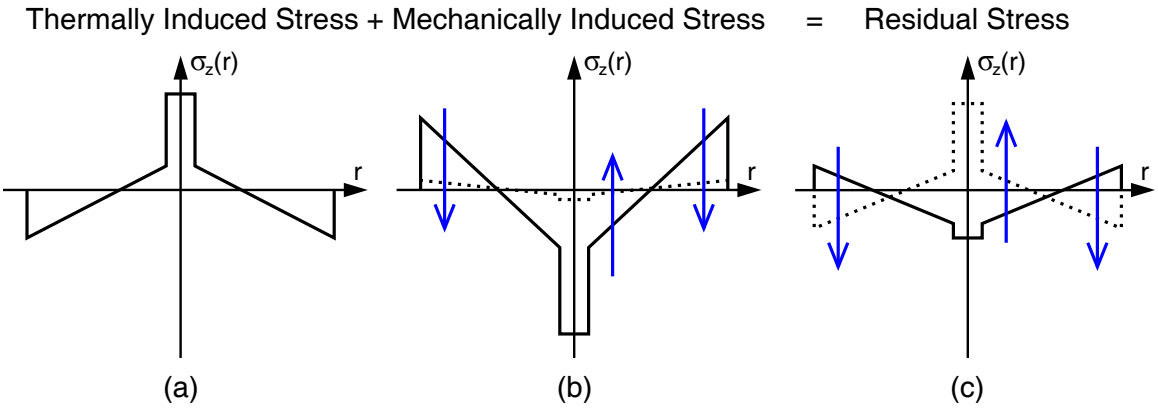

Figure 5.12: Relative contributions of thermally induced stress (a) and mechanically induced stress (b) to the total residual stress (c) in an unperturbed fiber (solid line) and a fiber exposed to a focused pulse of CO_2 laser radiation (dotted line). The arrows indicate the effect of the CO_2-laser-induced stress relaxation.

5.1.3.3 Mean Axial Stress

The mean axial stress inside the exposed fiber was evaluated to investigate the presence of inelastic strain birefringence. The mean axial stress for various cross sections along the fiber axis is shown in Fig. 5.13. The mean axial stress was calculated using Eq. (5.1) as a function of longitudinal position, z, along the fiber. Shown for comparison is the mean axial stress of +4.70 MPa in the unperturbed fiber. The extent of the focused, 140-µm-diameter beam on the fiber covers approximately $48 \leq z \leq 188$ µm. Inside this region, the mean axial stress is less than +1.5 MPa. Outside this region, the mean axial stress rapidly approaches the mean axial stress of the unperturbed fiber. The decreased mean axial stress in the exposed region indicates a decrease in the inelastic strain birefringence of the fiber. This suggests that the exposure to the CO_2-laser radiation reduced the inelastic strains induced during manufacturing because of frozen-in viscoelasticity.

Also present in the exposed region is a slight increase in the mean axial stress at the center of the exposure. It is hypothesized that this increase is due to the reintroduction of inelastic strain resulting from frozen-in viscoelasticity. The Gaussian shape of the CO_2 laser beam causes the peak of the laser power, which corresponds to the peak heating in the fiber, to occur at the center of the exposure. In addition, when the LPFG was fabricated, the fiber was held under a small amount of tension with a 3.9 g mass attached to one end. If the laser-induced heating combined with the tension produced conditions in the fiber which were similar to the drawing conditions, then a small amount of frozen-in viscoelasticity, and thus inelastic strain, may have been reintroduced when the exposure was finished and the fiber cooled.

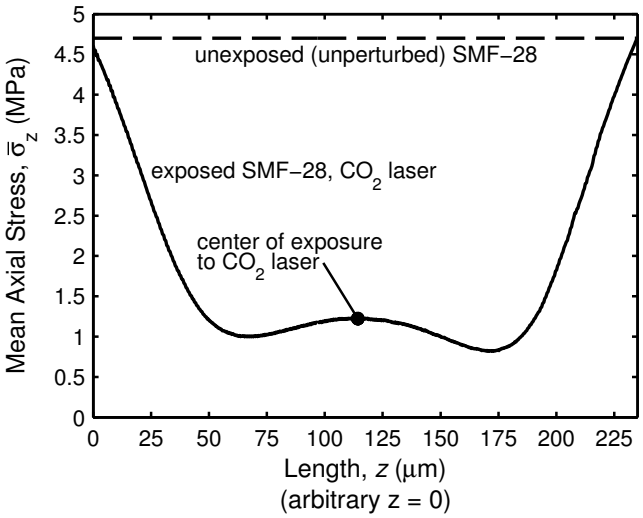

Figure 5.13: Mean axial stress inside the fiber exposed to CO_2-laser radiation at various lengths along the fiber axis (solid curve). For comparison, the mean axial stress inside the unperturbed Corning SMF-28 fiber is shown (dashed line).

5.1.4 Performance and Accuracy

No absolute standard of comparison for this type of measurement exists, however, several figures of merit can be used to assess the performance of the presented technique and apparatus. These figures of merit also provide a basis of comparison with other techniques as well as for future development and improvements. The performance of the presented technique and apparatus is evaluated in terms of the lateral spatial resolution, the noise present in the determined retardation, the noise present in the determined RSD, and the accuracy of the RSD. As discussed in Chapter 4 the lateral spatial resolution of the measurement apparatus is about 0.49 µm. This is the spatial resolution, or lateral resolving power, of the imaging optics as well as the spatial resolution of the binned images used to determine the retardation.

The noise present in the retardation is determined from the standard deviation of the retardation in the region surrounding the fiber (surrounding-region retardation). The average standard deviation of the surrounding region of all the retardation maps obtained for the unperturbed Corning SMF-28 fiber is 0.013 nm (at $\lambda = 546$ nm).

This is a 78% improvement from the 0.058 nm obtained from the initial measurement reported in [88] and [89] (reported as 0.06 nm). The improvement is attributed to (1) the more appropriate quadratic-polynomial-fit interpolation procedure discussed in Sec. 2.1.3 and (2) the better performance of the QImaging CCD camera relative to the camera reported in [89]. Further analysis of the retardation maps reveals a noise level throughout the fiber that is similar to the noise in the surrounding region. Therefore, the noise in the retardation determined with the improved technique and apparatus is estimated to be ± 0.013 nm. This value provides an estimate of the retardation resolution.

The noise present in the RSD is obtained by calculating the standard deviation of the axial component of the cross-sectional RSD in the region surrounding the fiber. This accounts for any effects of the filtered-backprojection algorithm. However, rather than consider the entire surrounding region, only an annular ring between the outer cladding edge and a circle inscribing the RSD data is considered. This eliminates the four corners of the RSD data that are generated from zeros appended to either side of the profiles in the aligned retardation sinogram, shown in Fig. 2.7(c). This zero padding is necessary for any tomographic reconstruction that uses filtered backprojection [95]. The standard deviation of the RSD in the annular-ring region surrounding the fiber is 0.35 MPa. This is a 68% improvement from the 1.10 MPa obtained from the initial measurement reported in [89]. This improvement is also attributed to (1) the more appropriate quadratic-polynomial-fit interpolation procedure discussed in Sec. 2.1.3 and (2) the better performance of the QImaging CCD Camera relative to the camera reported in [89]. Further analysis of the RSD reveals a noise level throughout the fiber that is similar to the noise in the surrounding region. Thus, the noise in the RSD determined with the presented technique is estimated to be ± 0.35 MPa. This value provides an estimate of the axial stress resolution.

A known reference value of the stress present in Corning SMF-28 fiber is not

available. However, an estimate of the accuracy of the presented technique can be made by comparing the current measurement of a Corning SMF-28 fiber with several published radial profiles of the axial stress in the same type of fiber [41,46,112] and the initial measurement [88, 89]. This estimate assumes that the structural features and the stress levels are consistent for all Corning SMF-28 fibers. The average peak value of the tensile stress at the outer edge of the cladding provides a common reference. The determination of the stress level at this location is less susceptible to variations between the techniques than the determination of the stress in the core or at the core-cladding boundary. The average peak stress values in the published literature and in the distribution shown in Fig. 5.1 are listed in Table 5.1. The group average peak value of all the results is 9.97 MPa. The accuracy of each result is assessed in terms of the difference between the average peak stress of the result and the group average. The difference for the presented technique is 0.27 MPa. Therefore, the accuracy relative to the other published results is estimated to be ±0.27 MPa.

Table 5.1: Average peak stress in Corning SMF-28 fiber.

Source	Average SMF-28 Peak Stress (MPa)	Group Average Peak Stress (MPa)	Difference[1] (MPa)
Ref. [41]	11.30		1.33
Ref. [46]	9.04		−0.93
Ref. [46]	9.91	9.97	−0.06
Ref. [112]	9.60		−0.37
Refs. [88, 89]	9.74		−0.23
Present Measurement	10.24		0.27

[1] Difference between the individual average peak stress and the group average peak stress.

5.2 Refractive-Index Characterization

5.2.1 Determination of Optimal Imaging Parameters

The quantitative-phase microscopy (QPM) technique requires the careful selection of the numerical aperture (NA) of the condenser and the defocus distance used to obtain the defocused images of the optical fiber [99]. The *a priori* optimal settings for the condenser NA and the defocus distance for the characterization of optical fibers are not clear. Furthermore, tradeoffs exist for selecting these parameters. In this section, the guidelines for selecting the condenser NA and the defocus distance are discussed and the results of preliminary measurements to determine the optimal settings are presented. From these results, the optimal settings are determined for the present measurement apparatus.

The condenser NA affects the coherence of the light that illuminates the fiber [99]. A higher NA results in less coherent illumination, which can increase the spatial resolution of the microscope. However, a lower NA results in more coherent illumination, which increases the spatial resolution of the longitudinal intensity derivative, and thus the spatial resolution of the phase shift.

The defocus distance must be small enough to provide an accurate approximation of the longitudinal change in the intensity, $\partial I/\partial z_m$, but it must be large enough to enable the detection of changes in the intensity in the presence of noise [99, 110]. Here longitudinal refers to the direction of propagation of the illuminating beam in the microscope. In addition to degrading the approximation of $\partial I/\partial z_m$, a larger defocus distance results in the blurring of the intensity distribution by the increasingly visible effects of diffraction. The manual for a commercially available software package that implements the QPM technique recommends a defocus distance of 1 µm for imaging performed with a 40× objective [120]. However, reports of the determination of the refractive-index profiles (RIPs) and the refractive-index distributions (RIDs) in fibers specify defocus distances of 2−3 µm with a 40× objective [69, 108].

Preliminary measurements were performed to determine the optimal condenser NA and the optimal defocus distance for the characterization of optical fibers. The relative RIP, $\Delta n(r) = n(r) - n_{oil}$, of an unperturbed Corning SMF-28 fiber was characterized with the procedure and apparatus described in Chapters 3 and 4. The term relative is omitted for brevity in the remainder of this chapter, but all references to and measurements of RIPs and RIDs refer to the refractive index relative to the index-matching oil. The RIP, rather than the full RID, was determined to assess rapidly the effect of changing the condenser NA and the defocus distance. The fiber was surrounded by a light mineral oil with an unknown index of refraction between the indices of the core and the cladding of the fiber.

Single phase-shift measurements were performed with condenser NAs of 0.1, 0.2, 0.4, and 0.6 and defocus distances of 1, 2, and 3 µm. The radial phase-shift profile was determined by solving for the full-field phase shift using Eq. (3.3) and then extracting the center column (center phase-shift profile). Based on the results presented in Sec. 3.2.2, the RIP was calculated from the phase-shift profile using the Fourier algorithm. The number of points along the fiber core radius, N, was set equal to the number of points in the phase-shift profile to eliminate the need for interpolation. The step size of the transformed variable, dt, and the number of Fourier harmonics, k, were set to 10^{-2} and 200 respectively. The number of Fourier harmonics is greater than the number used for the simulated data presented in Sec. 3.2.2.4 because the step-index profile of a Corning SMF-28 fiber resulted in a phase-shift profile with higher spatial frequencies than the power-law profile used previously.

A set of ten identical measurements was performed for each combination of the condenser NA and the defocus distance. In the following sections, the average RIP from a measurement set (ten identical measurements) is analyzed. Averaging in this manner removes the small differences that may occur from measurement to measurement and reveals clearly the differences that are caused by changing the condenser

NA and the defocus distance. The performance of each combination of the condenser NA and the defocus distance is assessed by (1) examining the qualitative features in the RIPs, (2) determining the accuracy of the RIPs, and (3) determining the repeatability of the measurements. The effect of the repeatability of focusing the fiber is also quantified.

5.2.1.1 Refractive-Index Profile Features

The average RIPs for each combination of the condenser NA and the defocus distance are shown in Fig. 5.14. The error bars indicate the standard deviation of a measurement set at positions of r = 2, 10, 20, 30, 40, 50, 60, and 70 µm. The dotted lines indicate the core radius (4.1 µm) and the cladding radius (62.5 µm) of the Corning SMF-28 fiber.

The profiles obtained with low condenser NAs have a less uniform cladding refractive-index than the profiles obtained with higher NAs. However, the profiles obtained with higher NAs show a more gradual change at the boundaries between the various regions of the fiber. These gradual changes indicate that a higher condenser NA results in a decreased spatial resolution of the longitudinal intensity derivative, and thus a decreased spatial resolution of the resulting RIP. Based on these observations, it is determined that a condenser NA of 0.4 is necessary to (1) provide an accurate measurement of the RIP as indicated by the uniform cladding and (2) avoid any unnecessary degradation in the spatial resolution.

The standard deviation of the profiles decreases with increasing defocus distance. This illustrates the necessity of increasing the defocus distance to enable the detection of changes in the intensity in the presence of experimental noise. Based on this observation, it is determined that a defocus distance of 3 µm is necessary enable the reliable, repeatable detection of the changes in the intensity.

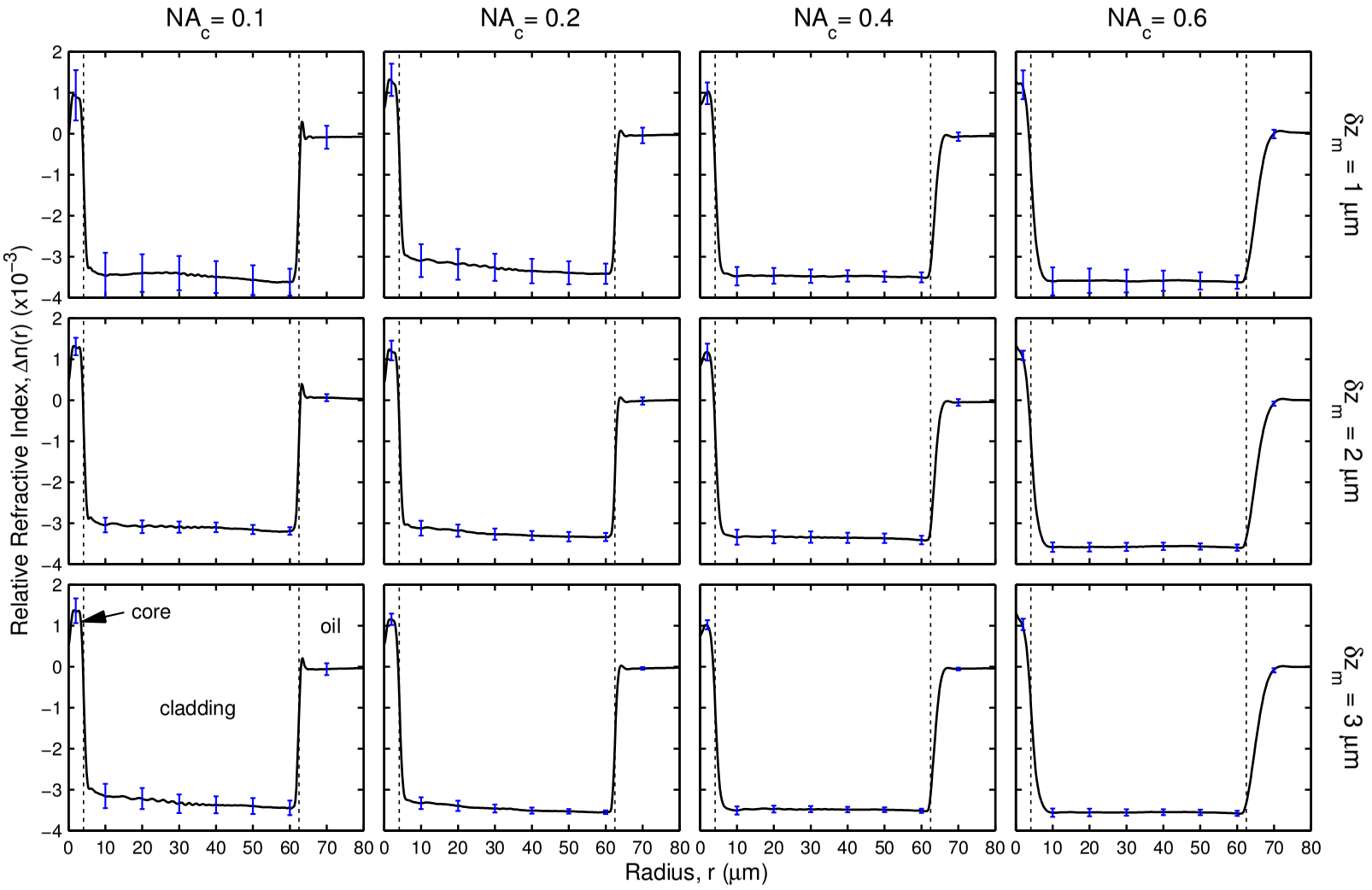

Figure 5.14: Average RIPs of an unperturbed Corning SMF-28 fiber obtained using the QPM technique with various condenser numerical apertures, NA_c, and defocus distances, δz_m. Each RIP is the average of ten measurements. The error bars indicate the standard deviation of the average RIP at positions of r = 2, 10, 20, 30, 40, 50, 60, and 70 µm. The dotted lines indicate the core radius and the cladding radius of a Corning SMF-28 fiber.

5.2.1.2 Refractive-Index Profile Accuracy

A quantitative assessment of the accuracy of the measured RIPs is performed by analyzing the step-index difference between the core and the cladding of the fiber, $\Delta n_s = n_{core} - n_{clad}$, where n_{core} is the maximum refractive index in the core region and n_{clad} is the average refractive index in the cladding region. The average of several reported measurements of Corning SMF-28 fibers indicates that $\Delta n_s = 4.97 \times 10^{-3}$ with a standard deviation of $\pm 1.86\%$ [63, 79, 121]. This value is used as a reference for the presented results. The average step-index difference of the RIPs for each combination of the condenser NA and the defocus distance are shown in Table 5.2. The percent difference between the average measured values and the reference value is shown in Table 5.3.

Table 5.2: Average Δn_s ($\times 10^{-3}$) of a Corning SMF-28 fiber for each combination of condenser numerical aperture, $\mathrm{NA_c}$, and defocus distance, δz_m.

	$\mathrm{NA_c}$			
δz_m (µm)	0.1	0.2	0.4	0.6
1	4.39	4.67	4.50	5.04
2	4.45	4.48	4.57	4.88
3	4.70	4.61	4.52	4.86

Table 5.3: Percent difference between the average measured Δn_s and the reference Δn_s for Corning SMF-28 fiber for each combination of condenser numerical aperture, $\mathrm{NA_c}$, and defocus distance, δz_m.

	$\mathrm{NA_c}$			
δz_m (µm)	0.1	0.2	0.4	0.6
1	−11.7%	−6.1%	−9.5%	1.5%
2	−10.4%	−9.8%	−8.1%	−1.9%
3	−5.4%	−7.3%	−9.0%	−2.1%

The results shown in Table 5.3 indicate that a high condenser NA provides a more accurate measurement of Δn_s. However, there is no clear relationship between the accuracy in measuring Δn_s and the measurement parameters when the condenser NA is less than 0.6. This apparent random variation for condenser NAs less than 0.6 is the result of not performing a background measurement for each combination of the condenser NA and the defocus distance. As discussed in Sec. 3.3.2, a background measurement is required to remove background phase shifts induced by the imaging system. The relatively high percent differences for the measurements with a condenser NA less than 0.6 are a result of background phase shifts that were not removed.

5.2.1.3 Measurement Repeatability

The repeatability of each combination of the condenser NA and the defocus distance is assessed by determining the standard deviation in the measured step-index difference for each measurement set. It is desirable to have a standard deviation in the measured step-index difference that is lower than the standard deviation of the reference step-index difference (1.86%). The standard deviations of the measured step-index differences are shown in Table 5.4. In general, a larger condenser NA and a larger defocus distance, which improve the detection of changes in the intensity in the presence of noise, provide a more repeatable measurement.

Table 5.4: Percent standard deviation in Δn_s for ten identical measurements.

	NA_c			
δz_m (µm)	0.1	0.2	0.4	0.6
1	5.66%	4.44%	3.63%	5.51%
2	1.94%	2.94%	1.64%	2.14%
3	2.12%	1.07%	1.61%	1.36%

5.2.1.4 Focusing Repeatability

The automated control of the fine focus knob provides repeatable defocusing of the fiber. However, the in-focus position of the fiber must be found manually. The radial runout of the fiber during rotation leads to defocusing and occasionally requires finding a new in-focus position. Therefore, the effect of variability in finding the in-focus position was investigated.

The effect of varying the in-focus position, z_{m0}, was determined by performing measurements with an intentional error in the in-focus position; the in-focus position was set intentionally to a position other than the position of best focus, $z_{m,bf}$. A set of 12 measurements was performed for each combination of the condenser NA and the defocus distance: four measurements with $z_0 = z_{m,bf}$, four with $z_{m0} = z_{m,bf} - 0.5$ µm, and four with $z_{m0} = z_{m,bf} + 0.5$ µm. The standard deviations of the step-index differences that were measured with the intentional in-focus position errors are shown in Table 5.5. The standard deviations are similar to those presented in Table 5.4. Several of the standard deviations for the measurements with the intentional in-focus position error are lower than the measurements with a consistent in-focus position. This result indicates that small variations in the in-focus position between measurements are negligible. The repeatability of the defocus distance, rather than the in-focus position, is the crucial parameter.

Table 5.5: Percent standard deviation in Δn_s for measurements with intentional in-focus position error.

	NA_c			
δz_m (µm)	0.1	0.2	0.4	0.6
1	5.14%	4.09%	5.16%	4.94%
2	2.77%	3.83%	2.17%	2.47%
3	1.51%	1.28%	1.19%	1.30%

Tables 5.4 and 5.5 indicate that the standard deviation in the step-index difference of measurements performed with a condenser NA of 0.4 and a defocus distance of 3 µm is lower than the standard deviation of the reference step-index difference. This demonstrated repeatability, combined with the qualitative assessment of Fig. 5.14, supports the selection of these values.

5.2.2 Unperturbed Fiber

The RID in an unperturbed Corning SMF-28 fiber was measured with the optimal condenser NA of 0.4 and the optimal defocus distance of 3 µm using the procedure and apparatus described in Chapters 3 and 4. A typical cross-sectional RID is shown in Fig. 5.15.

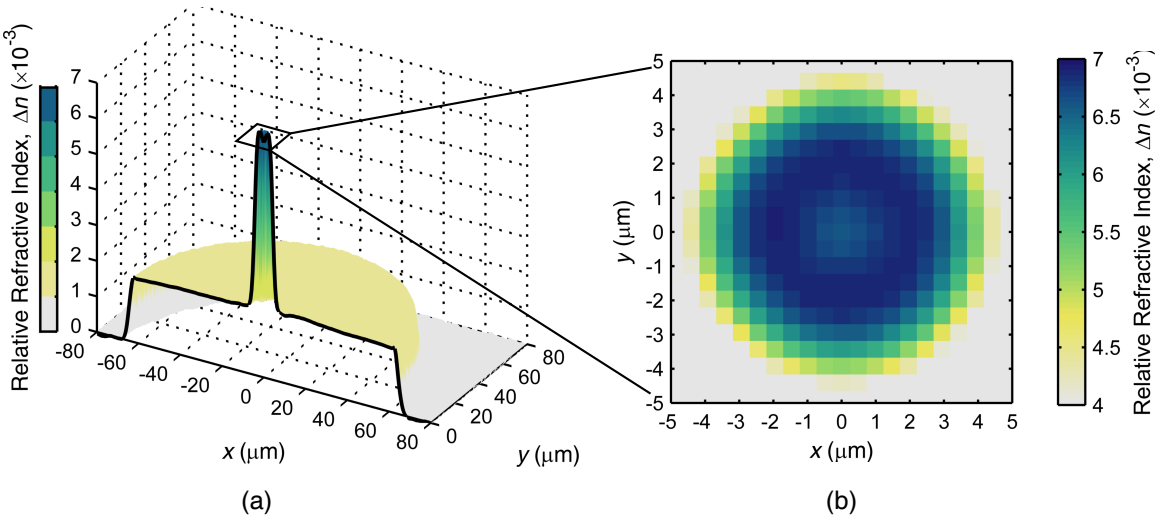

Figure 5.15: Plots of a typical cross-sectional RID in an unperturbed Corning SMF-28 fiber: (a) three-dimensional plot showing expected step-index profile; and (b) pseudo-color plot of the core showing central dip or burn-off region.

The fiber was surrounded by an index matching oil from Cargille Labs specified to have $n_D = 1.4580$. The three-dimensional plot shows that the expected step-index profile is reconstructed. Slightly visible in the three-dimensional plot and clearly visible in the pseudo-color plot of the core is a region of lower refractive index in the center of the core. This region is referred to as the center dip or burn-off region.

The decrease in the refractive index is a consequence of the internal vapor deposition used to manufacture the core preform [122]. In the final stage of collapsing the tube to form the core preform, some of the dopant gas is not deposited on the innermost layer, resulting in a lower index of refraction in the center of the core. This center dip has been measured in the same type of fiber by other techniques and indicates sufficient spatial resolution to characterize this small feature [61, 63, 121].

5.2.3 Performance and Accuracy

The performance of the index characterization technique and apparatus is assessed in a manner analogous that used for the stress characterization technique/apparatus, discussed in Sec. 5.1.4. The performance of the presented technique and apparatus is evaluated in terms of the lateral spatial resolution, the noise present in the determined phase shift, the noise present in the determined RID, and the accuracy of the RID. As discussed in Chapter 4 the lateral spatial resolution of the measurement apparatus is about 0.49 µm.

The noise present in the phase-shift is determined from the standard deviation of the phase shift in the region surrounding the fiber (surrounding-region phase shift). The average standard deviation of the surrounding region of all the phase-shift maps obtained for the unperturbed Corning SMF-28 fiber is 2.84 nm (at $\lambda = 546$ nm). This value provides an estimate of the phase-shift resolution.

The noise present in the RID is obtained by calculating the standard deviation of the cross-sectional RID in the region surrounding the fiber. However, as discussed in Sec. 5.1.4, only an annular ring between the outer cladding edge and a circle inscribing the RID data is considered. The standard deviation of the RID in the annular-ring region surrounding the fiber is 2.34×10^{-5}. Thus, the noise in the RID determined with the presented technique is estimated to be $\pm 2.34 \times 10^{-5}$. This value provides an estimate of the refractive-index resolution.

A known reference value of the refractive index present in Corning SMF-28 fiber is not available. However, an estimate of the accuracy of the presented technique can be made by comparing the current measurement of a Corning SMF-28 fiber with several published RIPs in the same type of fiber [61, 63, 121]. This estimate assumes that the RIP is consistent for all Corning SMF-28 fibers. The step-index difference, Δn_s, provides a common reference that is less susceptible to dispersion, and therefore, measurements made at different wavelengths. The step-index difference in the published literature, one unpublished result, and the distribution shown in Fig. 5.1 are listed in Table 5.6. The group average step-index difference of all the results is 5.01×10^{-3}. The accuracy of each result is assessed in terms of the difference between the step-index difference of the result and the group average step-index difference. The difference for the presented technique is 1.4×10^{-4}, which is the estimated accuracy relative to the other results.

Table 5.6: Step-index difference, Δn_s, in Corning SMF-28 fiber.

Source	Δn_s ($\times 10^{-3}$)	Group Average Δn_s ($\times 10^{-3}$)	Difference[1] ($\times 10^{-4}$)
Ref. [61]	5.09		0.8
Unpublished[2]	4.90		-1.1
Ref. [121]	4.90	5.01	-1.1
Ref. [63]	5.00		-0.1
Present Measurement	5.15		1.4

[1] Difference between the individual Δn_s and the group average Δn_s.
[2] Unpublished measurement by B. L. Bachim using technique from [61].

5.3 Summary

In this chapter, measurements of the RSD in a Corning SMF-28 fiber in an unperturbed region, a region near a cleaved end-face, and a region exposed to CO_2 laser radiation were presented. The results indicate that the developed BKC technique and the measurement apparatus are capable of resolving small structural features

and small variations in azimuthally asymmetric distributions of the axial stress. The measurement of the unperturbed fiber resolved the compressive stress at the core-cladding boundary that results from the presence of OH impurities introduced during the manufacture of the fiber preform. An analysis of the region surrounding the fiber was used to determine the noise in the retardation and the axial stress. The noise in the retardation was calculated to be ± 0.013 nm (at $\lambda = 546$ nm) and the noise in the axial stress was calculated to be ± 0.35 MPa. A comparison with other published profiles of the axial stress in Corning SMF-28 fiber gives an estimated accuracy of the axial stress of ± 0.27 MPa.

Measurements of the RIP and the RID in an unperturbed Corning SMF-28 fiber were also presented. A sequence of measurements with various settings of the condenser NA and the defocus distance reveal that a condenser NA of 0.4 and a defocus distance of 3 µm are optimal for characterizing optical fibers with the current apparatus. The measurement of the RID resolved the center dip in the core of the fiber that results from dopant burn off. An analysis of the region surrounding the fiber was used to determine the noise in the phase shift and the refractive index. The noise in the phase shift was calculated to be ± 2.84 nm (at $\lambda = 546$ nm) and the noise in the refractive index was calculated to be $\pm 2.34 \times 10^{-5}$. A comparison with other published profiles of the refractive index in Corning SMF-28 fiber gives an estimated accuracy of the refractive index of $\pm 1.4 \times 10^{-4}$. While no standard of comparison exists for these types of measurements, these figures of merit provide a provide a basis of comparison with other techniques as well as for future development and improvements.

CHAPTER 6

CHARACTERIZATION OF CO_2-LASER-INDUCED LPFGS

6.1 Previous Efforts

The knowledge of the residual-stress distribution (RSD) and the refractive-index distribution (RID) in carbon-dioxide-laser-induced long-period fiber gratings (CO_2-laser-induced LPFGs) is crucial to the understanding and the optimizing of their fabrication and performance. The general effect of the CO_2-laser radiation on the RSD and the RID in several types of optical fibers has been investigated and theories have been developed about the functional form of the physical properties and the processes that occur during the fabrication of the LPFGs. Unless otherwise specified, investigations of conventional (germanium-doped core, pure-silica cladding) telecommunications fibers are discussed.

Davis *et al.* measured the refractive-index profile (RIP) at various axial positions in the first CO_2-laser-induced LPFGs using transverse interferometry [76]. Although this technique is not capable of characterizing the azimuthally asymmetric RID, the measurement did provide evidence that the exposure to the focused laser pulses caused an increase in the refractive index of the cladding on the side facing the exposure. It was hypothesized that stress relaxation and densification were responsible for the increase in the refractive index.

6.1.1 Theoretical Investigations

Drozin *et al.* modeled the heat transfer within an optical fiber exposed to a focused CO_2 laser and indicated that the fiber reaches temperatures on the order of 1700 °C

[123]. This is higher than the fictive temperature of the fiber (the temperature to which the glass must be heated to produce a change in the molecular structure at room temperature), which is on the order of 1500−1600 °C in a 125-µm-diameter silica fiber [116, 124]. This result indicates that the laser-induced heating is sufficient to melt locally the fiber and then allow it to solidify with a room-temperature density, and thus refractive index, that is different from the pre-exposure room-temperature refractive index.

VanWiggeren *et al.* calculated the intensity distribution inside the fiber cross section for one-sided exposure to an incident plane wave with $\lambda = 10.6$ µm [29]. Strong absorption of the CO_2 laser light results in a significant azimuthal variation in the intensity distribution inside the fiber, which is shown in Fig. 6.1. This result indicates that the changes in the refractive index will be azimuthally asymmetric and larger on the side of the fiber facing the exposure.

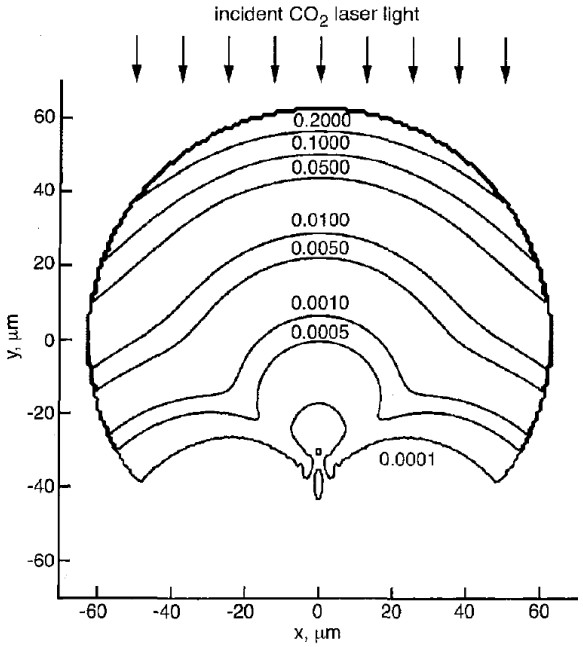

Figure 6.1: Calculated intensities (relative to unity incident intensity) over a fiber transverse cross section for incident CO_2 laser light with $\lambda = 10.6$ µm. The fiber diameter is 125 µm and the complex refractive index is $n = 2.22 - j0.1$. The light is polarized parallel to the longitudinal axis of the fiber [29].

Yamasaki *et al.* and Kim *et al.* provided more detailed hypotheses about the relationship between the relaxation of mechanically induced (mechanical) stresses and the stress-induced changes in the RID that are caused by the CO_2-laser radiation [118, 119]. Although these investigations do not consider conventional telecommunications fibers, the hypotheses apply. As discussed in Sec. 5.1.1 and shown in Fig. 5.2, the drawing of fibers with a doped-silica core and a pure-silica cladding results in the formation of compressive mechanical stresses in the core and tensile mechanical stresses in the cladding. It was hypothesized that the CO_2-laser radiation would relax these stresses and change the RID of the fiber because of the photoelastic effect. The change in the stress caused by the CO_2-laser radiation is shown conceptually in Fig. 6.2.

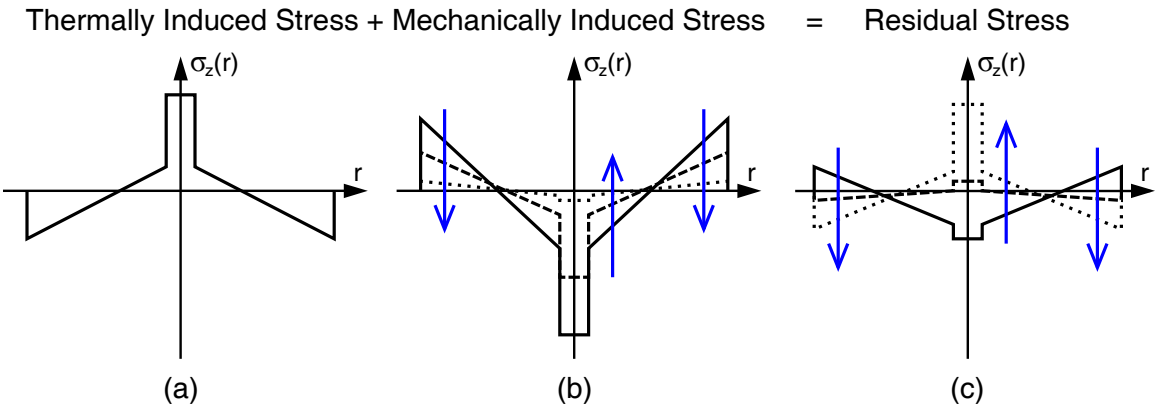

Figure 6.2: Relative contributions of thermally induced stress (a) and mechanically induced stress (b) to the total residual stress (c) in an unperturbed fiber (solid line) and a fiber exposed to CO_2 laser radiation (dashed and dotted lines). The arrows indicate the effect of increased CO_2-laser-induced stress relaxation. The dashed lines and the dotted lines indicate progressively more relaxed stress profiles.

The photoelastic effect describes the relationship between the stress and the refractive index in the optical fiber. Stresses in a room-temperature (elastic) fiber induce strains, which as discussed in Sec. 5.1.1, affect the refractive index of the fiber. Therefore, changes in the stress result in changes in the strain and thus the refractive index. The photoelastic effect is described in more detail in Sec. 6.3.1, but in several

of the previous efforts summarized here, it is simplified to relate the changes in the axial stress, $\Delta\sigma_z$, to the changes in the refractive index for polarization in the radial direction, Δn_r, of the fiber

$$\Delta n_r = C_2 \Delta\sigma_z, \tag{6.1}$$

where C_2 is the stress-optic or photoelastic constant and is assumed to be equal to that of silica glass (-4.22×10^{-6} MPa^{-1}) [114]. In a conventional fiber, the CO_2 laser radiation relaxes the compressive mechanical stresses in the core leaving only the tensile thermally induced (thermal) stresses. This positive net change in the stress leads to a decrease in refractive index of the core as governed by Eq. (6.1). This is consistent with the net decrease in $n_\perp$ due to positive strain as shown in Fig. 5.4(a). The opposite occurs in the cladding.

6.1.2 Investigations of Changes in the Core

The effect of the CO_2-laser radiation on the residual stress was first measured by Kim *et al.* using the Sénarmont compensator technique [22]. Custom fibers with germanium-boron-doped cores were drawn with various levels of draw tension to produce different levels of compressive mechanical stress in the core. Measurements of the radial profile of the axial stress, which assume azimuthal symmetry, were made on the fibers before and after a 15 minute exposure to unfocused CO_2-laser radiation.

The measurements performed by Kim *et al.* on the unexposed fibers showed that the fibers drawn at higher draw tensions had higher levels of compressive stress in the core before the exposure [22]. After the exposure however, each fiber had approximately the same level of tensile stress in the core. These results indicate a laser-induced relaxation of the compressive mechanical stress that revealed the tensile thermal stress, as indicated in Fig. 6.2(b) and (c). The thermal stress was assumed to be independent of the draw tension because each fiber had approximately the same

level of tensile stress in the core after the exposure. This evidence confirmed the hypothesis that the exposure to the CO_2-laser radiation relaxes the mechanical stresses in a fiber with a doped-silica core. However, the use of a long-duration, unfocused exposure is not similar to the typical focused, short-duration exposures used for LPFG fabrication.

The effect of CO_2-laser radiation on the refractive index of a fiber with a doped-silica core has been estimated using interferometric techniques [23,85]. The techniques use the fringe shift in a fiber-based interferometer to estimate the change in the refractive index of the core resulting from the exposure to the CO_2 laser radiation. The first investigation [23] used custom fibers with germanium-boron-doped cores drawn with various levels of draw tension to produce different levels of compressive mechanical stresses in the core. Short sections of the fibers were inserted in to a fiber-based interferometer and the interference fringes were measured before and after multiple 15 minute exposures to unfocused CO_2-laser radiation. The refractive index of the core was estimated to decrease. This is consistent the previous evidence of mechanical stress relaxation in the core (net increased stress) [22] and the resulting index decrease predicted by the photoelastic effect, Eq. (6.1).

The second investigation [85] used a Corning SMF-28e optical fiber exposed to multiple short-duration exposures from a focused CO_2-laser. The exposure parameters were chosen to match those used for LPFG fabrication. As with the previous investigations, the refractive index of the core was estimated to decrease. While these two investigations are in general agreement with mechanical stress relaxation, the interferometric techniques required the assumption that the changes in the refractive index were spatially uniform and occurred primarily in the core.

6.1.3 Investigations of Changes in the Cladding

Fourier-transform infrared (FTIR) spectroscopy has been used to estimate the refractive-index modulation in the cladding of a CO_2-laser-induced LPFG fabricated in conventional telecommunications fiber [86]. The results indicate an increase in the refractive index of the cladding. This is consistent with (1) the hypothesis of mechanical stress relaxation in the cladding (net decreased stress) and the resulting index increase predicted by the photoelastic effect, Eq. (6.1), and (2) the previous evidence that densification is possible. However, the relative contributions of stress relaxation and densification were not determined.

6.1.4 Qualitative Investigations

The Sénarmont compensator technique was used to characterize the cross-sectional RSD in a CO_2-laser-induced LPFG fabricated in a standard optical-network fiber (LG Cable single-mode fiber) [24]. The measurement confirmed that an azimuthally asymmetric change in the RSD is caused by the one-sided exposure to the laser radiation. An analysis of the cross-sectional RSD was used to estimate the polarization-dependent response of the LPFG, but no measurement of the RID was performed. Furthermore, the RSD of the fiber was not characterized before the exposure to the CO_2 laser radiation.

The developed Brace-Köhler compensator (BKC) technique was also used to characterize the cross-sectional RSD in a CO_2-laser-induced LPFG fabricated in a Corning SMF-28 fiber. The results are covered in detail in Sec. 5.1.3, and the RSD was similar to that measured in the LG Cable fiber [24].

Microinterferometric optical phase tomography (MIOPT) was used to characterize the cross-sectional RID in a CO_2-laser-induced LPFG fabricated in Corning SMF-28 fiber [79]. The measurement confirmed that an azimuthally asymmetric change in the RID is caused by the one-sided exposure to the laser radiation. However, because

MIOPT can only provide the average cross-sectional RID over the axial distance spanned by adjacent fringes, the direct comparison of this RID measurement with a measurement of the RSD is lacking.

Despite the efforts towards the characterization of CO_2-laser-induced LPFGs, the information available is insufficient (1) to enable the modeling of LPFG behavior without assumptions about the functional form of the physical properties and (2) to provide a complete understanding of the processes and changes that occur during LPFG fabrication. This information is necessary for the design of LPFGs for specific applications and the tailoring of fabrication parameters to achieve the design requirements. The remainder of this chapter describes the efforts to provide this crucial information. This includes a description of the fabrication of an incrementally exposed fiber and the results of characterizing the RSD and the RID in various regions of this fiber using the developed BKC and quantitative-phase microscopy (QPM) techniques.

6.2 Characterization of an Incrementally Exposed Fiber

6.2.1 Incrementally Exposed Fiber

An incrementally exposed fiber was fabricated by periodically exposing a Corning SMF-28 fiber from one side to focused CO_2 laser pulses ($\lambda = 10.6$ µm) with incrementally increasing durations. A diagram of the fiber is shown in Fig. 6.3. The fiber was prepared by removing approximately 40 mm of the fiber buffer with a mechanical fiber stripper and cleaning the stripped section with wipes and isopropyl alcohol. The fiber was then placed in the LPFG fabrication apparatus described by Bachim [79].

The fiber was held on a translation stage with the longitudinal axis of the fiber in the horizontal direction. The laser was focused by a cylindrical lens into a vertical line (perpendicular to the longitudinal fiber axis). This gives a tightly focused Gaussian beam in the fiber longitudinal direction, z, but a nearly uniform exposure in the

transverse direction. The duration of the exposure was controlled with a mechanical shutter. The LPFG fabrication apparatus and a typical fabrication procedure are described in further detail in the literature [32, 79].

The incrementally exposed fiber was exposed every 2 mm along the length of the fiber to laser pulses with durations of 100, 200, 300, 400, and 500 ms. A single continuous laser pulse with a duration of 500 ms is typically required to fabricate each period of an operational LPFG. Dividing this duration into five smaller increments enabled the dynamic changes in the RSD and the RID to be characterized. Translating the fiber 2 mm between exposed regions ensured that there were no overlapping effects from adjacent regions.

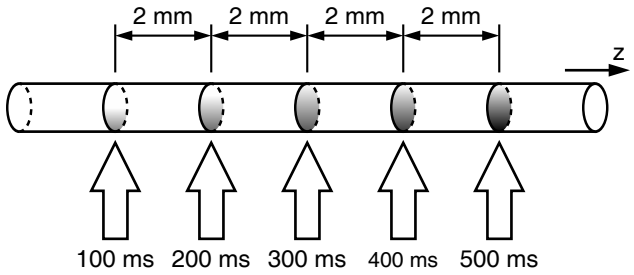

Figure 6.3: Diagram of incrementally exposed fiber. The spacing between each exposed region is 2 mm. The large arrows indicate one-sided exposure to a focused CO_2 laser pulse with the duration specified below the arrow.

6.2.2 Characterization Procedure

The three-dimensional RSD and RID in an unexposed region and each of the five exposed regions of the incrementally exposed fiber were characterized using the techniques and apparatus described in Chapters 2−4. Each of these six regions were positioned in the field-of-view (FOV) of the microscope by translating the fiber rotation apparatus (Sec. 4.1.3) in the longitudinal direction of the fiber. The laser-induced perturbations to the fiber birefringence in the exposed regions were visible when viewing the fiber between crossed polarizers. These visible longitudinal perturbations were used to center approximately each exposed region in the FOV. A longitudinal extent

of approximately 320 µm was visible within the FOV .

One region was characterized per day for six consecutive days (excluding the weekend). Measurements were made during business hours when the HVAC systems in the building were active to reduce variations in external environmental factors, such as the temperature, as much as possible. The typical procedure for characterizing one region required six to seven hours: one hour to allow the mercury-arc light source to warm up and stabilize, three to four hours to perform the retardation measurements with the BKC technique, and two hours to perform the phase-shift measurements with the QPM technique. The fiber remained in the custom microscope stage plate (Sec. 4.1.2) immersed in index-matching oil (Cargille Labs, $n_D = 1.4580$) between characterizing each region to prevent the introduction of contaminants.

6.2.3 Overall Results

Arrays of RSDs, $\sigma_z(x, y, z)$, and relative RIDs, $\Delta n(x, y, z) = n(x, y, z) - n_{oil}$, at various longitudinal positions, z, for each region of the incrementally exposed fiber are shown in Figs. 6.4 and 6.5. The center column in each figure, labeled $z = 0$ µm, corresponds approximately to the longitudinal center of the exposure to the focused CO_2 laser. The outer columns, labeled $z = -150$ µm and $z = 150$ µm, are approximately 10 µm inside the longitudinal extent of the fiber that was visible in the FOV.

Two procedures were performed on the distributions shown in Figs. 6.4 and 6.5 to enable the straightforward comparison of the RSDs and RIDs. First, the distributions were aligned azimuthally with the exposed side of the fiber facing downward. Second, the RIDs were normalized to have a constant relative refractive index in an a section of the cladding that is unaffected by the laser. This second procedure was required to compensate for small variations in the refractive index of the index-matching oil that were caused by differences in the temperature between characterizing each region (between days).

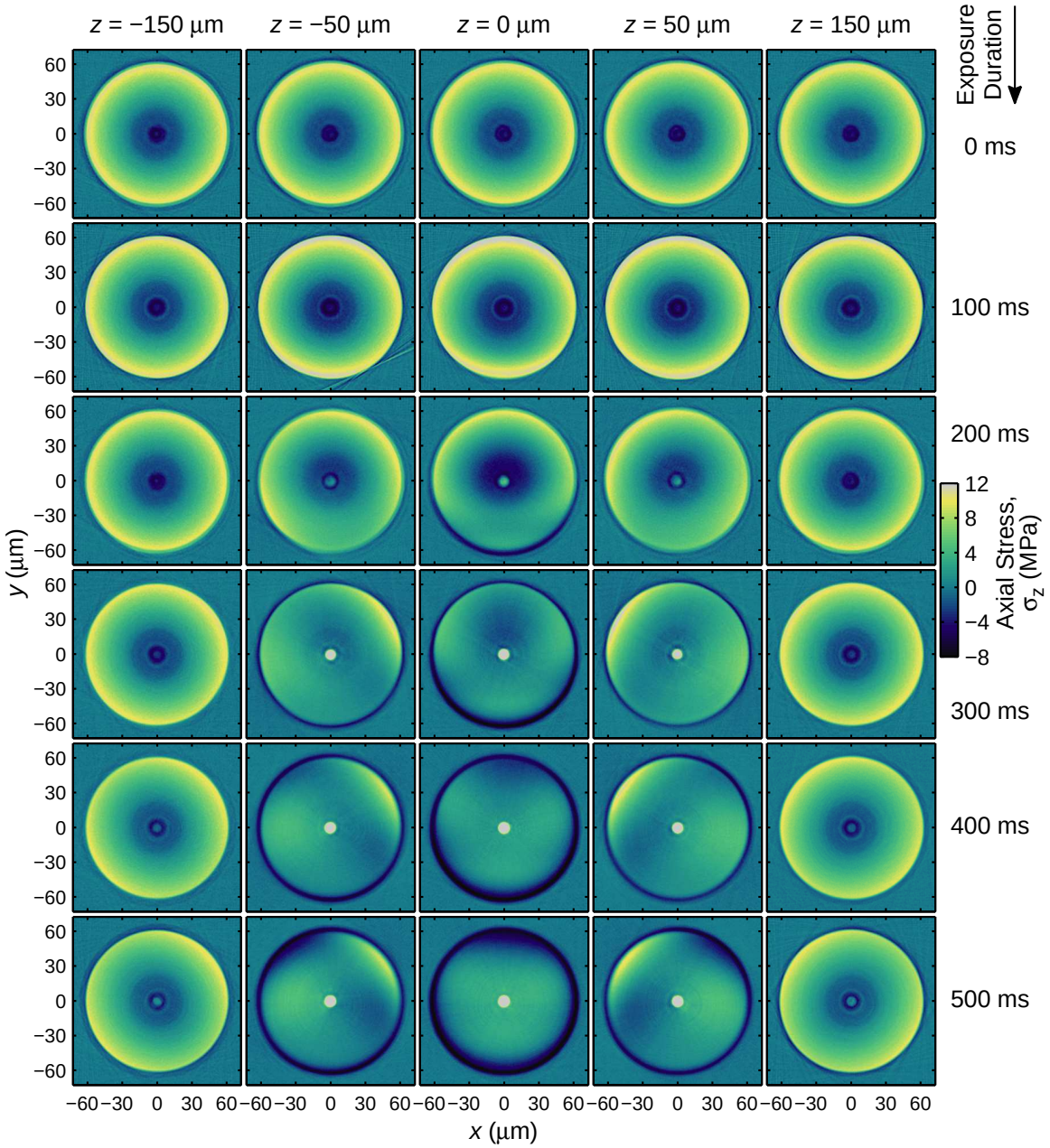

Figure 6.4: RSDs (axial component) at various longitudinal positions, z, in the unperturbed region (top row) and the incrementally exposed regions (subsequent rows) of the fiber. The center column of RSDs, labeled $z = 0$ µm, corresponds approximately to the longitudinal center of the exposure to the focused CO_2 laser.

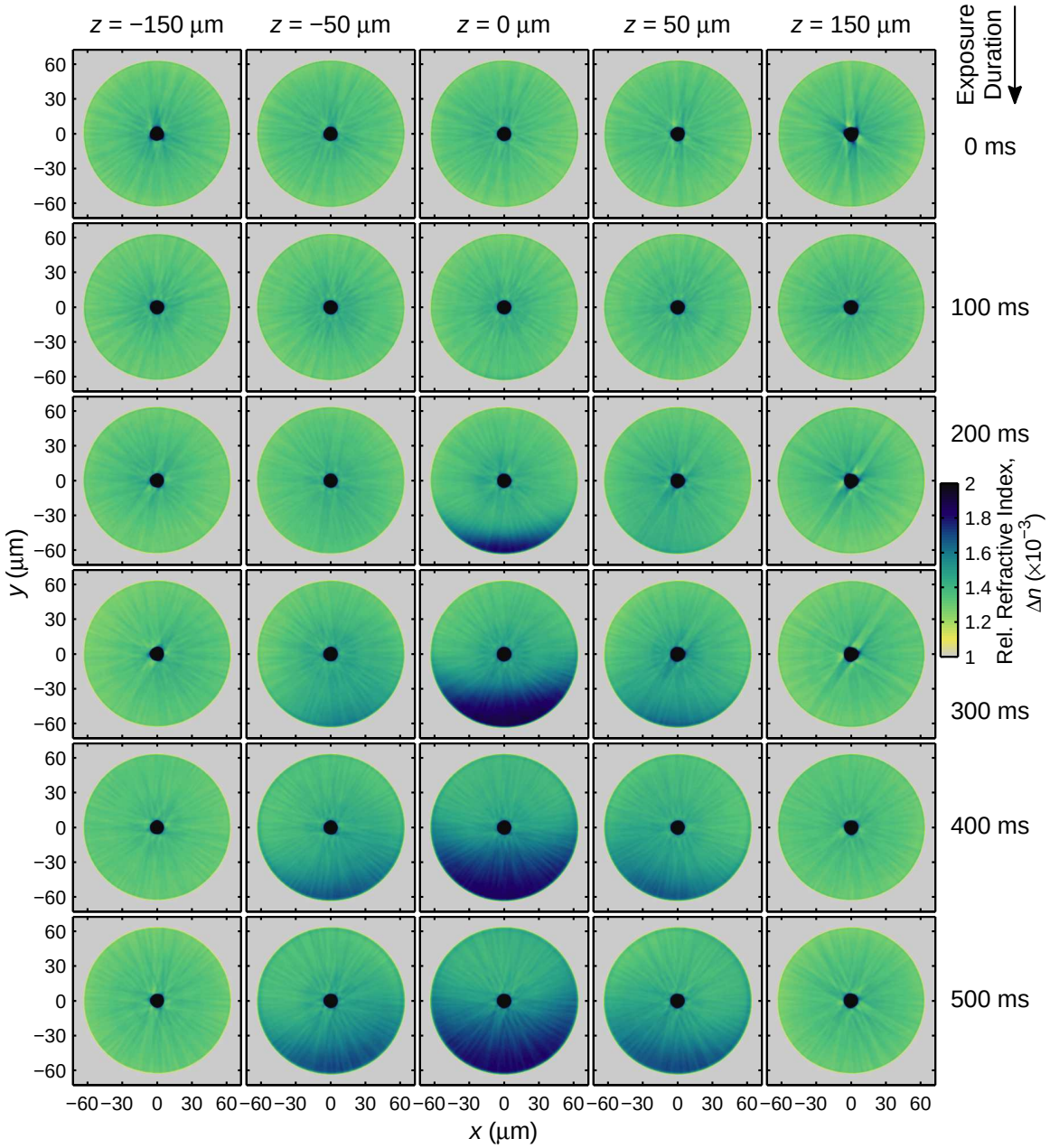

Figure 6.5: Relative RIDs at various longitudinal positions, z, in the unperturbed region (top row) and the incrementally exposed regions (subsequent rows) of the fiber. The center column of RIDs, labeled $z = 0$ µm, corresponds approximately to the longitudinal center of the exposure to the focused CO_2 laser.

6.2.3.1 Azimuthal Alignment

The azimuthal asymmetry of the RSDs and the RIDs in the exposed regions is clear in Figs. 6.4 and 6.5. This asymmetry is expected because of the one-sided exposure to the laser. The absorption of higher intensities results in more heating on the side of the fiber facing the exposure, and thus, the asymmetric changes. The direction of the exposure was determined for the $z = 0$ cross-sectional RSDs and RIDs by using the procedure to find the azimuthal orientation of the radial line that defines the mirror symmetry (mirror line) as given in Sec. 5.1.3.

The angular orientations of the mirror lines for the $z = 0$ cross-sectional RSDs and RIDs are shown in Fig. 6.6. Angular orientations of 0 deg and 90 deg indicate that no laser-induced asymmetry was determined. As expected, this is the case for both the RSD and the RID in the unperturbed fiber. However, there was also no detectable laser-induced asymmetry in the RID of the fiber exposed for 100 ms. The remainder of the RSDs and RIDs had a mirror line with an average azimuthal orientation of 29 deg, as indicated with the dashed line in Fig. 6.6.

Differences in the mirror line orientation are seen for (1) different exposure durations and (2) the RSD and the RID for a single exposure duration. The differences between the exposure durations are caused by slight changes in the azimuthal orientation of the fiber between characterizing the different regions. Each day after a region was characterized, the fiber chuck in the fiber rotation apparatus was loosened to allow the custom stage plate to be lowered. The next day when a new region was characterized, the chuck was re-tightened. Slight changes in the azimuthal orientation of the fiber likely occurred while moving the stage plate with the chuck loosened.

The difference between the RSD and the RID for a single exposure duration is not caused by the tightening and loosening of the fiber chuck because the chuck remained tight while characterizing a single region. These differences appear to increase with the exposure duration, indicating that they are related to the response of the RSD

and the RID to the exposure. The mirror line orientation in the RSD may be related not only to the direction of the exposure, but also to the horizontal orientation of the fiber. Although the fiber is held under a small amount of tension, it may bend slightly under its own weight, thus perturbing the stresses present in the fiber. Because of these differences, the RSDs and the RIDs shown in Figs. 6.4 and 6.5 were all rotated by the same average amount (90 deg − 29 deg = 61 deg) to orient the mirror line in approximately the vertical (y) direction.

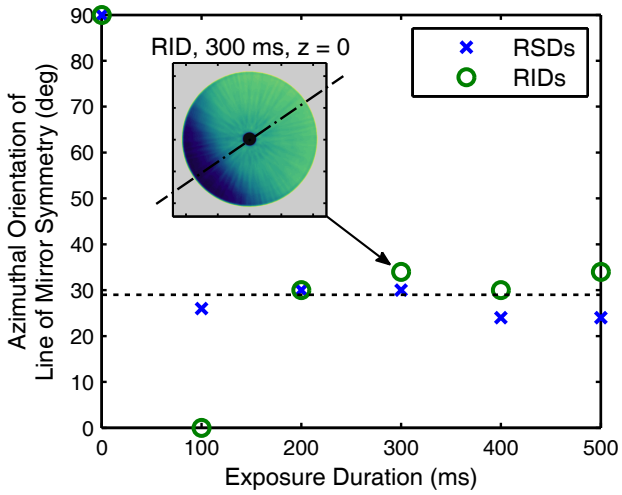

Figure 6.6: Azimuthal orientation of the mirror line in the $z = 0$ cross-sectional RSDs and the RIDs for each region of the incrementally exposed fiber. Orientations of 0 deg and 90 deg indicate that no laser-induced asymmetry was determined. The average of the orientations not equal to 0 or 90 deg was 29 deg, as indicated with the dashed line. The dot-dashed centerline on the inset RID is the mirror line for the $z = 0$ RID in the region of the fiber exposed to a 300 ms duration pulse.

6.2.3.2 RID Normalization

As discussed in Sec. 3.3.1, the refractive index of the index-matching oil is sensitive to changes in the temperature. This results in temperature-induced variations in the measured phase shift and the resulting calculated relative refractive index, $\Delta n(x, y, z) = n(x, y, z) - n_{oil}$. In Sec. 3.3.1, a procedure was given to minimize these temperature-induced variations during the time required to perform the phase-shift measurements in one region of the incrementally exposed fiber. However, temperature

variations still occurred between the six days required to characterize the six regions of the fiber. This resulted in a different refractive index of the index-matching oil each day and a consequent overall shift in the relative RID in each region. Therefore, the RIDs were normalized by determining a mean cladding relative refractive index, $\overline{\Delta n}_{clad}$, in a section of each characterized region that was unaffected by the laser.

The entire cladding between the longitudinal positions of $z = -150 \pm 5$ µm and $z = +150 \pm 5$ µm was assumed to be unaffected by the laser exposure. These sections are shown as shaded in the fiber diagram in Fig. 6.7. The center of the exposure is $z = 0$ and the $1/e^2$ intensity of the focused Gaussian beam occurs at $z \approx \pm 65$ µm.

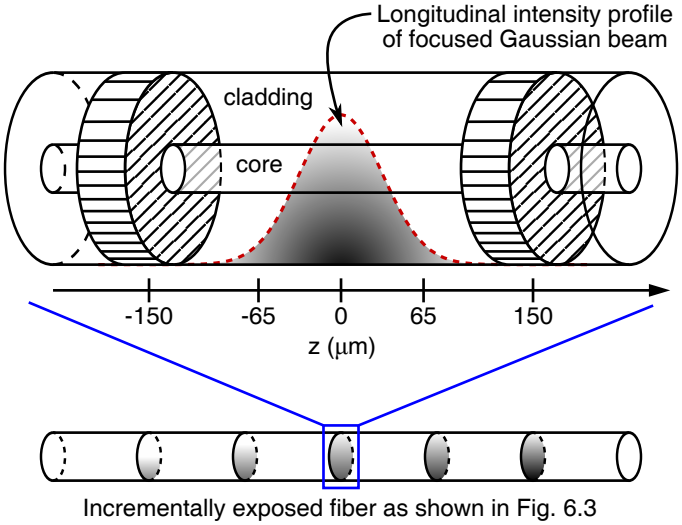

Figure 6.7: Diagram of fiber cladding sections (hatched) that are assumed to be unaffected by the exposure to the focused CO_2 laser. The approximate longitudinal intensity profile of the focused laser beam is shown with the dotted line. The core diameter, the cladding diameter, and the 10 µm longitudinal width of the shaded sections are exaggerated for clarity. A diagram of the incrementally exposed fiber is shown for reference.

The mean cladding relative refractive index, $\overline{\Delta n}_{clad}$, in these sections was determined by integrating the RID in these sections and dividing by the volume of the sections

$$\overline{\Delta n}_{clad} = \frac{\int_{-155\,\mu m}^{-145\,\mu m}\int_0^{2\pi}\int_{r_{core}}^{r_{clad}} \Delta n\, r\, \mathrm{d}r\, \mathrm{d}\theta\, \mathrm{d}z + \int_{145\,\mu m}^{155\,\mu m}\int_0^{2\pi}\int_{r_{core}}^{r_{clad}} \Delta n\, r\, \mathrm{d}r\, \mathrm{d}\theta\, \mathrm{d}z}{\int_{-155\,\mu m}^{-145\,\mu m}\int_0^{2\pi}\int_{r_{core}}^{r_{clad}} r\, \mathrm{d}r\, \mathrm{d}\theta\, \mathrm{d}z + \int_{145\,\mu m}^{155\,\mu m}\int_0^{2\pi}\int_{r_{core}}^{r_{clad}} r\, \mathrm{d}r\, \mathrm{d}\theta\, \mathrm{d}z} \tag{6.2}$$

where r_{core} and r_{clad} are the radii of the core and the cladding. The values of $\overline{\Delta n}_{clad}$ in the six regions of the incrementally exposed fiber are shown in Fig. 6.8. The fact that the values of $\overline{\Delta n}_{clad}$ are not equal indicates that temperature variations occurred between the six days required to characterize the six regions. Therefore, the RID in each region was normalized by shifting it to make $\overline{\Delta n}_{clad}$ in each region equal to the group average, which is indicated by the dashed line in Fig. 6.8. The result of this normalization procedure is evident in the RIDs in Fig. 6.5 as shown by the common shading in the cladding of the RIDs for $z = \pm 150$ µm (outer columns). This was not the case before the normalization procedure was performed.

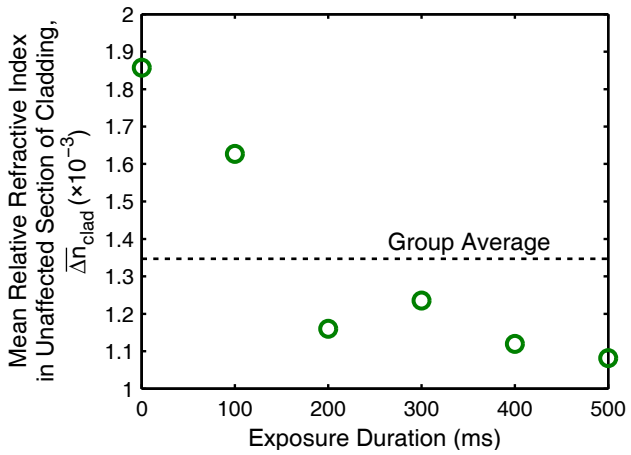

Figure 6.8: Mean cladding relative refractive index in sections of the incrementally exposed fiber unaffected by the CO_2 laser radiation. The dashed line indicates the group average.

6.3 Analysis of the Incrementally Exposed Fiber

The changes in the RSD and the RID that occur during the fabrication of an LPFG period can be estimated from the measurements of the incrementally exposed fiber. The changes are determined by subtracting the distribution in an exposed region of the fiber from the distribution in the unperturbed region of the fiber. These changes provide evidence of the temporal and spatial response of the axial stress and the refractive index to the CO_2 laser. Additionally, the change in the RSD can be used

with the photoelastic effect to estimate the stress-induced index changes in the fiber. The stress-induced index changes can then be compared directly to the measured index changes for each of the exposure durations. This comparison is enabled because the RSDs and the RIDs were characterized concurrently with one piece of equipment. In the remainder of this section, the photoelastic effect is described and the axial-stress changes, the stress-induced index changes, and the measured index changes are analyzed.

6.3.1 Photoelastic Effect

The photoelastic effect was introduced in Sec. 2.2.1 and expressed in Cartesian coordinates in Eq. (2.5). However, the stress-induced index changes in optical fibers are typically expressed in cylindrical coordinates [7]. Following Sec. 2.2.1, the residual stress, σ (in $\mathrm{Pa} \equiv \mathrm{N/m^2}$), can be decomposed into normal stress components, σ_r, σ_θ, and σ_z, along the three principal orthogonal directions. The stresses induce changes in the normally isotropic refractive index of the materials used in the fiber, n_0, giving rise to unique principal indices of refraction, n_r, n_θ, and n_z. The principal indices are for electric fields polarized in the radial, azimuthal, and longitudinal directions respectively. The anisotropic, principal refractive indices are related to the isotropic refractive index by

$$\begin{aligned} n_r &= n_0 + C_1\sigma_r + C_2(\sigma_\theta + \sigma_z), \\ n_\theta &= n_0 + C_1\sigma_\theta + C_2(\sigma_r + \sigma_z), \\ n_z &= n_0 + C_1\sigma_z + C_2(\sigma_r + \sigma_\theta), \end{aligned} \tag{6.3}$$

where C_1 and C_2 are the stress-optic or photoelastic constants of the extraordinary wave and the ordinary wave respectively (in $\mathrm{Pa^{-1}}$). The values of C_1 and C_2 in a silica-based optical fiber are assumed to be identical to those in fused silica. These values as measured in Corning fused silica at a wavelength of 546 nm and a temperature of 24−25 °C are $C_1 = -0.65 \times 10^{-6}$ $\mathrm{MPa^{-1}}$ and $C_2 = -4.22 \times 10^{-6}$ $\mathrm{MPa^{-1}}$ [114].

The notation used to express the relationships in Eq. (6.3) is not consistent in the

literature. The separate conventions used in the references of this thesis are described here to avoid confusion. The symbols C_1 and C_2 used in this thesis were chosen to be consistent with the notation in the source of their actual values, [114]. In some references however, the symbols C_1 and C_2 are replaced by C_a and C_b respectively [22] or by B_2 and B_1 respectively [7]. Furthermore, in this thesis, the terms after n_0 on the right hand side of Eq. (6.3) are added to make the equations general. However, some references subtract the terms on the right hand side of Eq. (6.3), and thus, the actual values of the stress-optic constants in fused silica are given as positive [5, 7].

The principal indices of refraction in the fiber before and after the exposure to the CO_2 laser can be expressed by Eq. (6.3). The stress-induced index changes are determined by subtracting the principal indices after the exposure from the principal indices before the exposure. The resulting terms for the changes in the transverse stresses, $\Delta\sigma_r$ and $\Delta\sigma_\theta$, can be neglected. As discussed in Sec. 6.1.2, the mechanical stress is primarily affected by the CO_2 laser [22]. Therefore, changes in the thermal stresses can be assumed to be negligible. In addition, the transverse mechanical stresses can be neglected in a drawn optical fiber [5, 125, 126]. This leaves only the changes in the axial stress, $\Delta\sigma_z$. With these simplifications, the stress-induced index changes that result from the laser exposure can be expressed in terms of the changes in the axial stress only,

$$\begin{aligned} \Delta n_{r,\sigma} &= C_2 \Delta\sigma_z, \\ \Delta n_{\theta,\sigma} &= C_2 \Delta\sigma_z, \\ \Delta n_{z,\sigma} &= C_1 \Delta\sigma_z, \end{aligned} \tag{6.4}$$

where the subscript $_\sigma$ indicates stress-induced index changes.

These relationships between changes in the stress and changes in the refractive index are consistent with the combined lattice effect and atomic effect in a strained optical fiber as described in Sec. 5.1.1 and shown in Fig. 5.4. The negative values of C_1 and C_2 indicate an inverse relationship between changes in the stress and changes

in the refractive index. This is consistent with the negative relationship between the strain and refractive index shown in Fig. 5.4. Furthermore, the fact that $|C_2| > |C_1|$ indicates that the refractive index change is larger for an electric field polarized perpendicular to the direction of the stress. This is consistent with the greater net change in $n_\perp$ for strains in the longitudinal (z) direction as shown in Fig. 5.4.

6.3.2 Overall Stress-Induced and Measured Index Changes

The stress-induced index changes determined by Eq. (6.4) are averaged to determine the average stress-induced index change

$$\Delta n_\sigma = \frac{2C_2 + C_1}{3}\Delta\sigma_z. \tag{6.5}$$

This enables the direct comparison to the measured index change, Δn_m, which, as discussed in Sec. 4.3.1, provides an average of the changes in the transverse and longitudinal indices.

Arrays of the stress-induced index change, $\Delta n_\sigma(x, y, z)$, and the measured index change, $\Delta n_m(x, y, z)$, at various longitudinal positions, z, for each exposed region of the incrementally exposed fiber are shown in Figs. 6.9 and 6.10. As in Figs. 6.4 and 6.5, the center column in each figure, labeled $z = 0$ µm, corresponds approximately to the longitudinal center of the exposure to the focused CO_2 laser. The outer columns, labeled $z = -150$ µm and $z = 150$ µm, are approximately 10 µm inside the longitudinal extent of the fiber that was visible in the FOV. The measured index changes for the exposure duration of 500 ms provide the first direct measurement of the three-dimensional index modulation in CO_2 laser-induced LPFGs. This information is crucial for the modeling of LPFG behavior.

There are two major differences that can be seen in Figs. 6.9 and 6.10. First, the asymmetry in the stress-induced index change is more subtle than in the measured index change. This difference indicates that the refractive index responds more closely to the predicted laser intensity distribution (Fig. 6.1) than the axial stress. Second,

the stress-induced index changes are approximately and order of magnitude smaller than the measured index changes. The values on the pseudo-color scale in Fig. 6.9 are exactly one order of magnitude less than those in Fig. 6.10. This indicates that the measured index changes, which are assumed to be the total index modulation, result primarily from a process other than stress relaxation.

These effects are examined further in the remainder of this section by analyzing (1) longitudinal profiles of the changes in the stress and the index and (2) the changes at the longitudinal center of the exposure ($z = 0$), both as a function of exposure duration. These analyses are performed in the core of the fiber, at a point in the cladding on the side of the fiber facing the exposure (bottom side in Figs. 6.9 and 6.10), and at a point in the cladding on the side opposite the exposure (top side). The longitudinal profiles provide further insight into the relationship between the changes and the laser intensity distribution. The changes at $z = 0$ provide insight into the processes that produce these changes.

6.3.3 Changes in the Core

The changes in the core of the incrementally exposed fiber were determined by averaging over the transverse (x, y) area of the core. This was done to remove any apparent variations that are caused by slight transverse misalignments between the distributions. As demonstrated in Chapter 5, the developed measurement techniques are capable of detecting small variations in the RSD and the RID over small spatial scales. The resolved center dip in the RID of the unperturbed fiber shown in Fig. 5.15 is an example of this. When two distributions are compared, or subtracted to determine the changes, slight spatial misalignments can produce apparent variations that are not actually present. This occurs most severely in regions of the fiber where there are large variations in the RSD or the RID over small spatial scales, such as the edges of the core and the edges of the fiber. This was addressed in the core by determining

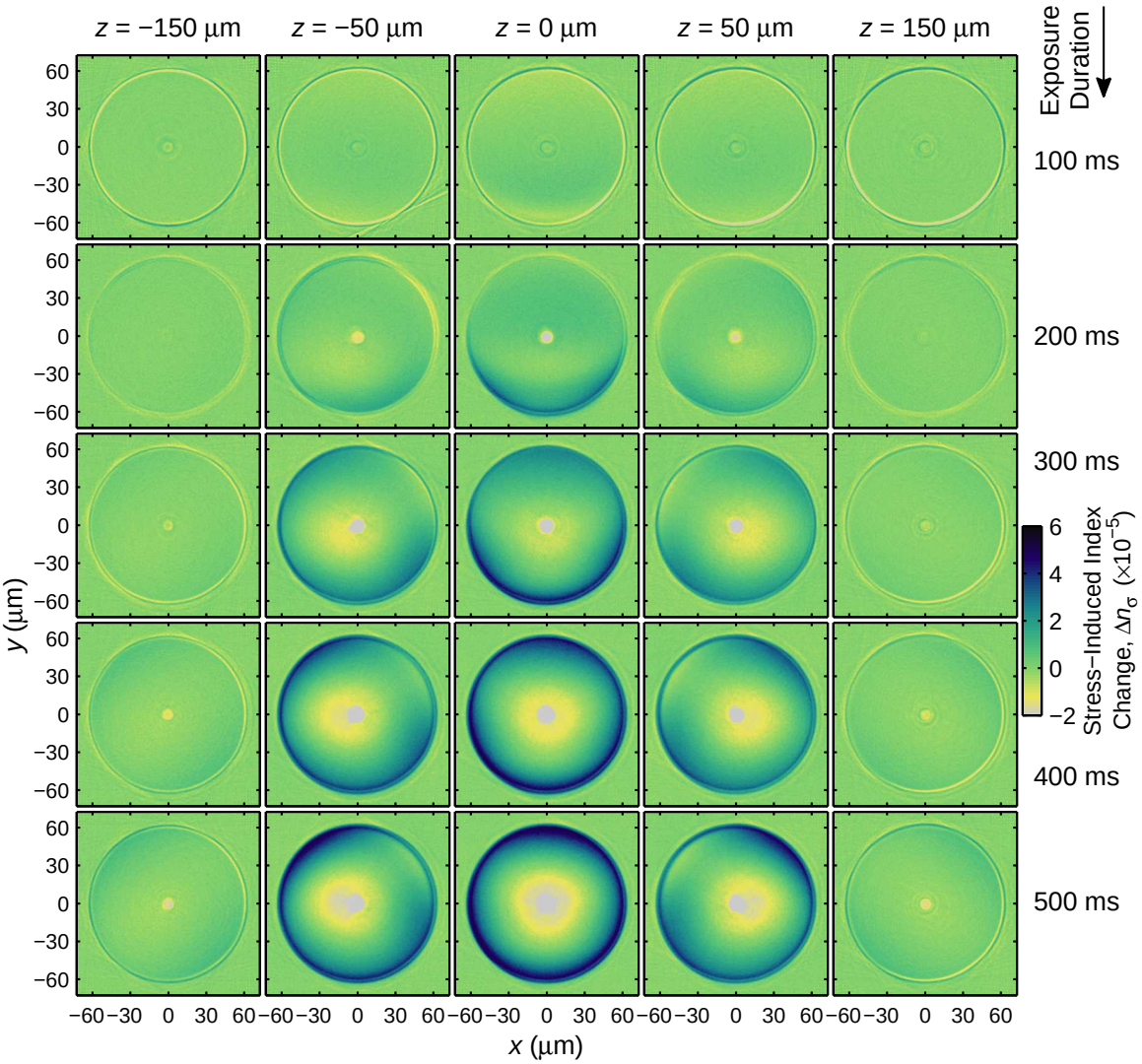

Figure 6.9: Distributions of the stress-induced index change at various longitudinal positions, z, in the exposed regions of the incrementally exposed fiber. The center column of distributions, labeled $z = 0$ µm, corresponds approximately to the longitudinal center of the exposure to the focused CO_2 laser.

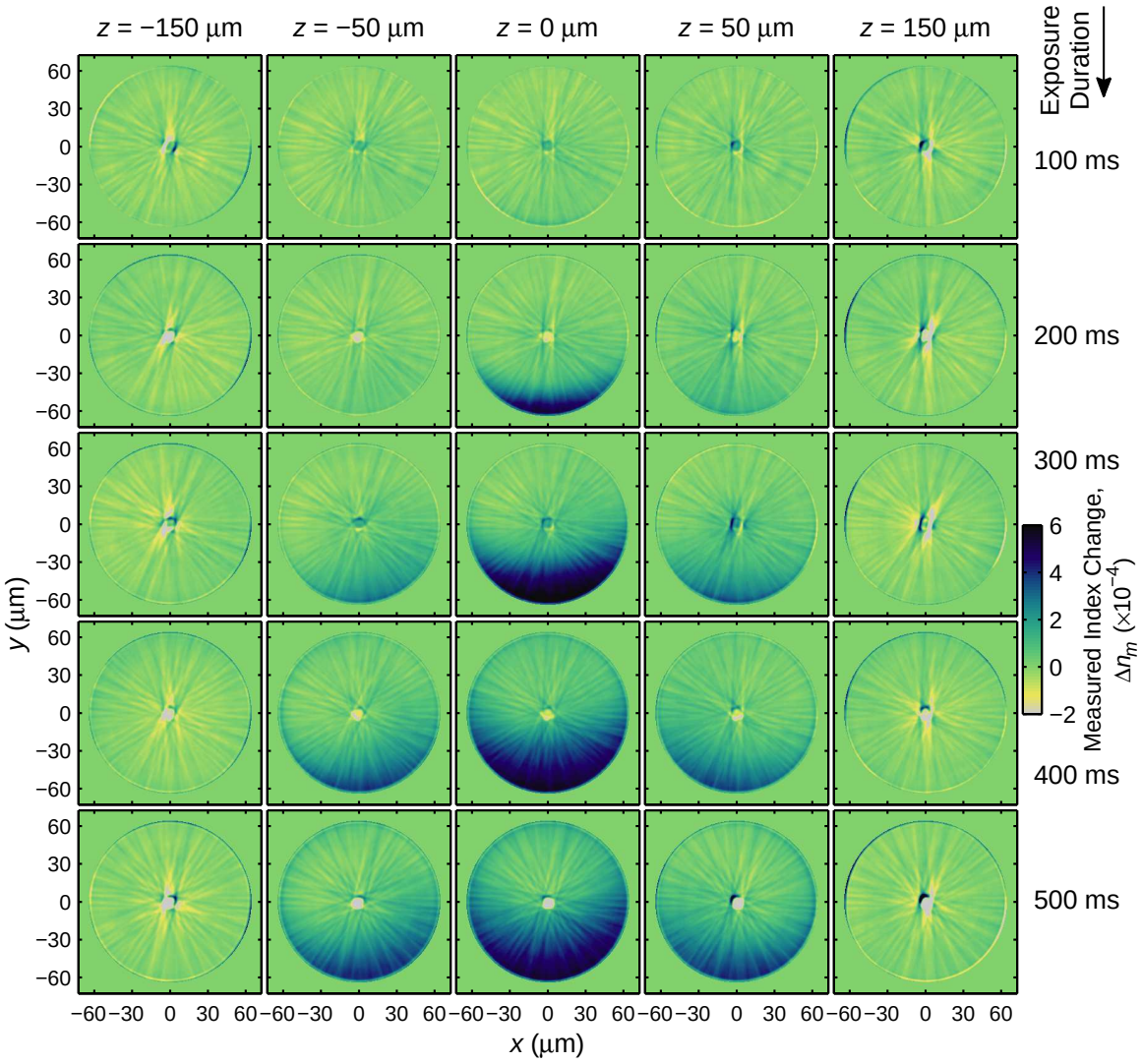

Figure 6.10: Distributions of the measured index change at various longitudinal positions, z, in the exposed regions of the incrementally exposed fiber. The center column of distributions, labeled $z = 0$ µm, corresponds approximately to the longitudinal center of the exposure to the focused CO_2 laser.

the average changes in the stress and the index over the area of the core.

6.3.3.1 Longitudinal Profiles

Longitudinal profiles of the axial-stress change, $\Delta\sigma_z(core, core, z)$, and the measured refractive-index change, $\Delta n_m(core, core, z)$, in the core are shown in Fig. 6.11. The notation $core, core$ in place of x, y indicates that the changes were determined by averaging over the area of the core as discussed previously. The axial-stress change profiles, shown in Fig. 6.11(a), increase consistently with the exposure duration. This increase corresponds to mechanical stress relaxation in the core (Fig. 6.2).

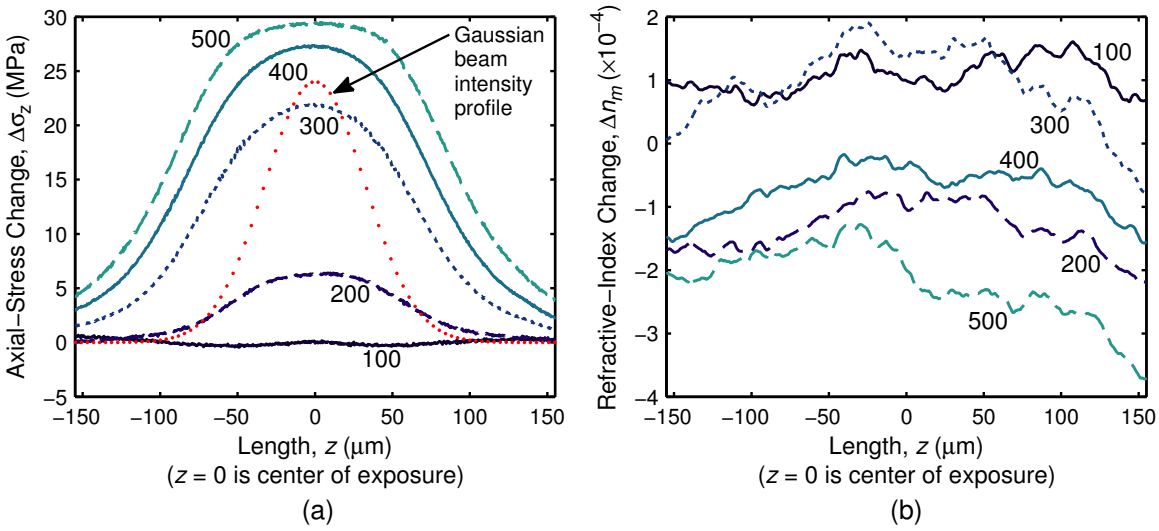

Figure 6.11: Longitudinal profiles of the axial-stress change (a) and the measured refractive-index change (b) in the core for various exposure durations. The exposure durations are listed near their respective profiles. Shown for reference in (a) is the longitudinal Gaussian intensity profile of the focused CO_2 laser beam.

The longitudinal shape of the axial-stress change profiles indicates that the stress responds in proportion to the longitudinal profile of the laser beam. The intensity profile of the focused Gaussian beam is shown with the annotated dotted line. The $1/e^2$ diameter of the focused beam is approximately 130 μm. The Gaussian-like profiles of the axial-stress change are much wider than the beam intensity indicating that the stress responds to a laser-induced thermal gradient that diffuses beyond the

exposed region. This is discussed further when the cladding facing the exposure is analyzed.

Unlike the axial-stress change profiles, the measured refractive-index change profiles, Fig. 6.11(b), appear to have no correlation to the exposure duration or to the beam intensity profile. The primary reason for this lack of correlation is likely an insufficient repeatability between measurements to resolve the small laser-induced index changes in the core. As discussed in Sec. 3.1.1, the QPM technique is based on the transport of intensity equation, Eq. (3.1), which requires the derivative of the intensity (of the light propagating through the microscope). This derivative is approximated with two defocused images of the fiber and a central-difference formula, Eq. (3.2). The accuracy of the central-difference formula is directly proportional to the accuracy with which the distance between the two defocused images (twice the defocus distance) is known. The accuracy of the calculated phase shifts and RID are both, in turn, directly proportional the accuracy of the intensity derivative. Therefore, any unknown percent error in the defocus distance results in the same percent error in the resulting RID.

The defocus is controlled by a computerized rotation stage coupled directly to the microscope fine focus adjustment knob with a gear-like coupling (Sec. 4.3.2). This coupling is not perturbed during the measurements required to characterize one region of the incrementally exposed fiber. However, between regions of the fiber, the rotation stage was removed from the fine focus adjustment knob to allow for manual control. Therefore, the coupling between the stage and the focus knob was re-established for each region of the fiber. The coupling consists of a smooth metal cylindrical surface mating to a smooth but compliant rubber surface. Variations in this coupling likely resulted in small variations in the actual defocus distance used for the different regions of the fiber.

The variation in the measured refractive-index change profiles in Fig. 6.11(b)

is approximately $\pm 3 \times 10^{-4}$. This is equivalent to the variation in the measured relative core refractive index of each exposed region, and it is approximately 4% of the maximum relative index measured in the core of the unperturbed region (Fig. 5.15). If this 4% is attributed to variations in the defocus distance alone, which was 3 µm for the measurements of the incrementally exposed fiber, then maximum coupling-induced defocus varations of only 120 nm occured between the measurements. Such small varaiations are not visible: the scale on the fine focus knob of the microscope is marked in 1 µm increments. A new defocusing apparatus consisting of a peizoelectric objective lens positioner with a repeatability of ±10 nm is currently available to reduce significantly the defocus distance variations as a source of error.

6.3.3.2 Changes at the Center of the Exposure

The axial-stress change and the refractive-index change in the core at the longitudinal center of the exposure ($z = 0$) are shown as a function of exposure duration in Fig. 6.12. These points correspond to the $z = 0$ values on the longitudinal profiles. In Fig. 6.12(b), both the measured index change (circles) and the stress-induced index change as predicted by Eq. (6.5) (x's) are shown.

The axial-stress change for exposure durations greater than 100 ms follows a power-law trend. The equation that best fits the change is inserted in Fig. 6.12(a). The fit indicates that the axial-stress change is asymptotically approaching a maximum value of 33.3 MPa. This behavior is expected for the relaxation of mechanical stress: there is a finite amount of mechanical stress in the fiber, and once fully relaxed, only the thermal stress remains.

The measured index change, shown with the circles in Fig. 6.12(b), indicates no clear relationship with the exposure duration, as discussed with the longitudinal profiles. However, the measured index change varies around the predicted stress-induced index change (x's). This suggests that even with the uncertainty in the

measured index, stress-induced index change may be the primary source of index modulation in the core of the fiber. If this is the case, the asymptotic behavior the axial-stress change indicates that the maximum decrease in the core refractive index is approximately 1×10^{-4}.

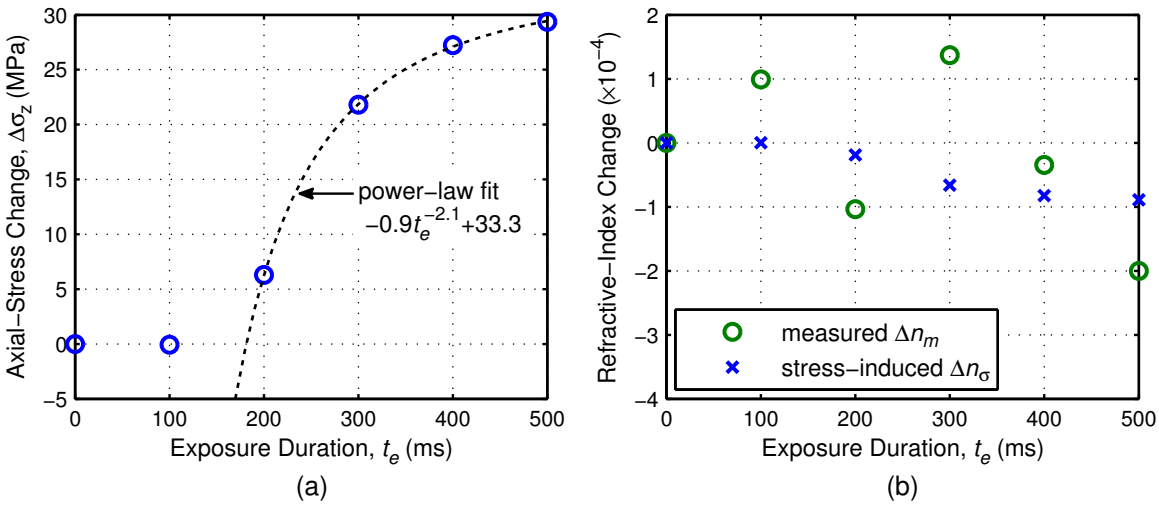

Figure 6.12: Changes in the core at the longitudinal center of the exposure: (a) axial-stress changes and (b) measured index changes (circles) and predicted stress-induced index changes (x's). The change in the stress for exposure durations greater than 100 ms follows a power-law trend.

6.3.4 Changes in the Cladding Facing the Exposure

The changes in the cladding were determined at a radius of approximately 57 µm on the side of the fiber facing the exposure (the point $x, y = 0, -57$ µm in Figs. 6.9 and 6.10). This point was chosen to be approximately 5 µm inside the boundary of the cladding to avoid the need to average over a small transverse area of the fiber; there are no large variations over small spatial scales in this region of the cladding.

6.3.4.1 Longitudinal Profiles

Longitudinal profiles of the axial-stress change, $\Delta\sigma_z(0, -57\ \mu\text{m}, z)$, and the measured refractive-index change, $\Delta n_m(0, -57\ \mu\text{m}, z)$, in the cladding facing the exposure are shown in Fig. 6.13. The axial-stress change profiles, Fig. 6.13(a), show a similar effect

to that seen in the core of the fiber. First, the decrease in the stress with the exposure duration is consistent with progressive mechanical stress relaxation in the cladding (Fig. 6.2). Second, the wide, Gaussian-like longitudinal shape of the profiles indicates that the stress responds to a laser-induced thermal gradient that diffuses beyond the exposed region.

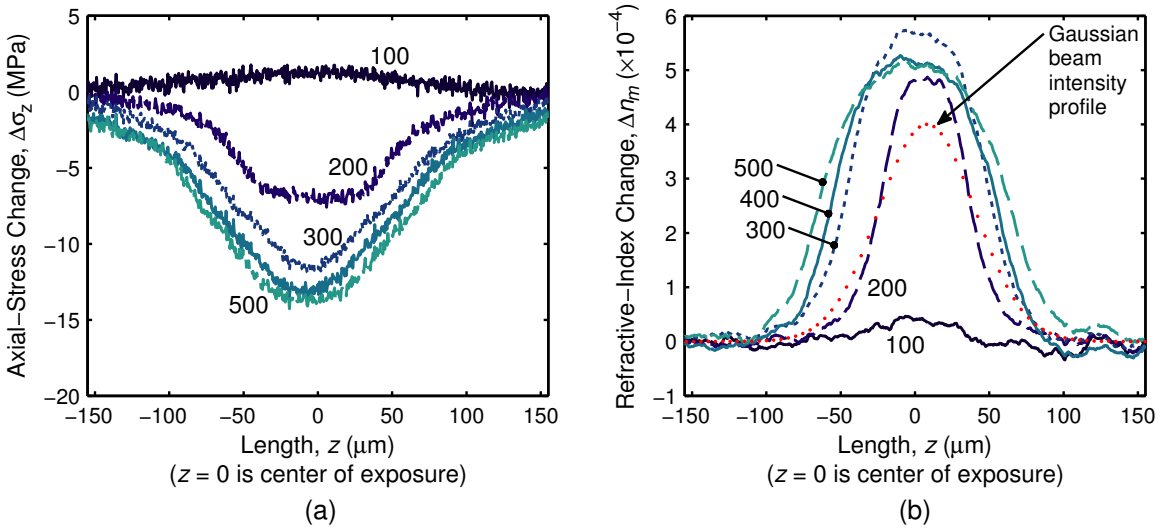

Figure 6.13: Longitudinal profiles of the axial-stress change (a) and the measured refractive-index change (b) in the cladding facing the exposure for various exposure durations. The exposure durations are listed near their respective profiles. Shown for reference in (b) is the longitudinal Gaussian intensity profile of the focused CO_2 laser beam.

The measured refractive-index change profiles, Fig. 6.13(b), also indicate a clear relationship to the exposure duration and the intensity profile of the focused CO_2 laser beam, which is shown with the annotated dotted line. As with the axial-stress profiles, the Gaussian-like longitudinal shape of the index profiles indicate that the refractive index responds to the a laser-induced thermal gradient. However, unlike the stress profiles, the refractive-index profiles quickly reach a relatively constant height and then widen with increased exposure durations. This suggests that if the stress and the index respond to a laser-induced thermal gradient that diffuses beyond the exposed region, then the stress responds more slowly with changes that become progressively larger and diffuse outward with increasing exposure durations. The

index, however, changes abruptly in magnitude between 100 to 200 ms and then diffuses outward while maintaining a relatively constant magnitude.

6.3.4.2 Changes at the Center of the Exposure

The axial-stress change and the refractive-index change in the cladding facing the exposure at the longitudinal center of the exposure ($z = 0$) are shown as a function of exposure duration in Fig. 6.14. The axial-stress change, Fig. 6.14(a), shows a similar effect to that seen in the core of the fiber. The change for exposure durations greater than 100 ms follows a power-law trend. The equation that best fits the change is inserted in Fig. 6.14(a). The fit indicates that the axial-stress change is asymptotically approaching a minimum value of -15.5 MPa. This behavior is expected for the relaxation of mechanical stress: there is a finite amount of mechanical stress in the fiber, and once fully relaxed, only the thermal stress remains.

The measured index change, shown with the circles in Fig. 6.14(b), is much larger than the stress-induced index change (x's) for exposure durations greater than 100 ms. This indicates that a process other than stress-induced index change is primarily responsible for the index modulation. Although there is some variation in the measured index change for exposure durations greater than 100 ms, the change remains relatively constant at approximately 5×10^{-4}. Yablon *et al.* showed that this is the expected annealing-induced index change, or densification, in the cladding of a conventional telecommunications fiber drawn with a typical draw tension of 1 N (100 g) [116].

The annealing performed by Yablon *et al.* consisted of heating several fibers drawn at various draw tensions to a temperature close to the fictive temperature for a few seconds. Measurements of the RIP of the fibers were performed before and after the annealing to determine the annealing-induced index changes. The index of the cladding was observed to increase uniformly and the magnitude of the increase was

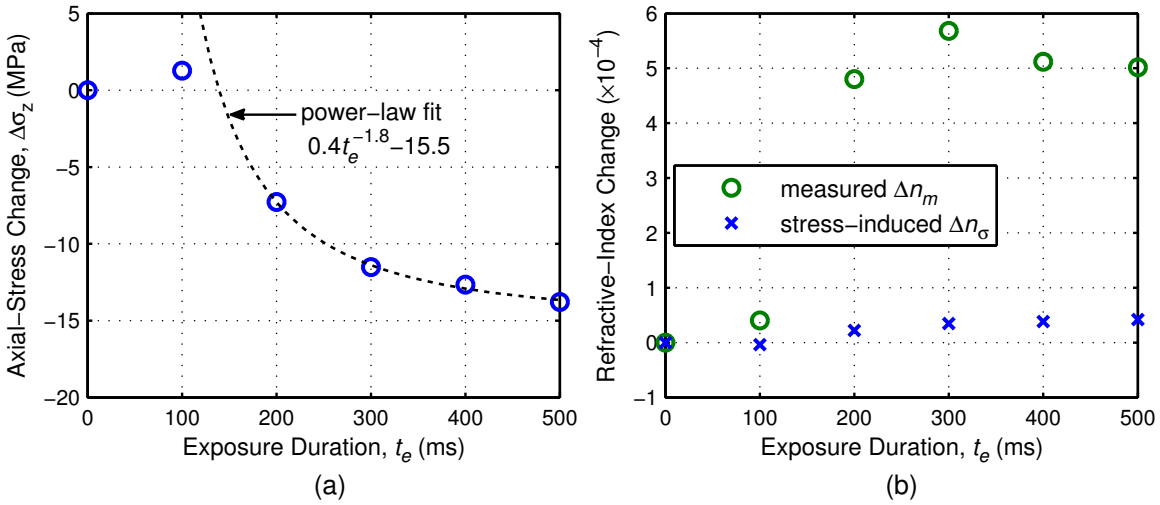

Figure 6.14: Changes in the cladding facing the exposure at the longitudinal center of the exposure: (a) axial-stress changes and (b) measured index changes (circles) and predicted stress-induced index changes (x's). The change in the stress for exposure durations greater than 100 ms follows a power-law trend.

related linearly to the draw tension used to manufacture the fiber. The index changes were described to originate from the relaxation of frozen-in viscoelasticity. This effect was discussed in Sec. 5.1.1 as being the source of inelastic strain birefringence in the fiber, however, Yablon *et al.* showed that frozen-in viscoelasticity also results in isotropic changes in the fiber index. The frozen-in viscoelasticity reduces isotropically the cladding index of an optical fiber when it is drawn (manufactured). The annealing process then heats the fiber to a temperature near or above its fictive temperature and the glass contracts to a higher density, and thus higher index, than was possible during the draw.

The relatively constant measured index change of approximately 5×10^{-4} for exposure durations greater than 100 ms indicates that the laser heats the fiber to a sufficiently high temperature to remove completely the frozen-in viscoelasticity in the optical fiber. Further investigation of the measured index changes in the cladding reveals that this complete removal is achieved only in a very shallow transverse region on the cladding-air boundary and over a small longitudinal width around the

longitudinal center of the exposure.

The measured index change, as seen in the 500 ms, $z = 0$ distribution (bottom center) in Fig. 6.10, drops from the side facing the exposure with a functional form similar to the intensity distribution in the fiber cross section (Fig. 6.1) predicted by VanWiggeren *et al.* [29]. The longitudinal profiles in Fig. 6.13(b) indicate that the longitudinal extents of the annealing-induced index changes are closely related to the longitudinal intensity profile of the laser. This evidence shows clearly the preferential heating in the fiber caused by the one sided exposure and indicates that the heating is sufficient to anneal locally, or produce local densification in, the optical fiber. The densification is achieved by relaxing the frozen-in viscoelasticity that results from the fiber drawing process.

6.3.5 Changes in the Cladding Opposite the Exposure

The changes in the cladding were also determined at a radius of approximately 57 µm on the side of the fiber opposite the exposure (the point $x, y = 0, 57$ µm in Figs. 6.9 and 6.10). This point was chosen approximately 5 µm from the cladding boundary to avoid the need to average over a small transverse area of the fiber. This point on the side of the fiber opposite the exposure also allows for the investigation of the index modulation where annealing is not likely to occur.

6.3.5.1 Longitudinal Profiles

Longitudinal profiles of the axial-stress change, $\Delta\sigma_z(0, 57\ \mu\text{m}, z)$, and the measured refractive-index change, $\Delta n_m(0, 57\ \mu\text{m}, z)$, in the cladding opposite the exposure are shown in Fig. 6.15. The axial-stress change profiles, Fig. 6.15(a), show a similar effect to that seen in the cladding facing the exposure. The decrease in the stress with the exposure duration is consistent with mechanical stress relaxation and the wide, Gaussian-like longitudinal shape of the profiles indicate that the stress responds to a laser-induced thermal gradient that diffuses beyond the exposed region.

The refractive-index change profiles, Fig. 6.15(b), also indicate a relationship to the exposure duration and the intensity profile of the focused CO_2 laser beam, although this relationship is much weaker than was seen in the cladding facing the exposure. This relationship is evident only in the regions of the fiber exposed for 400 ms or more.

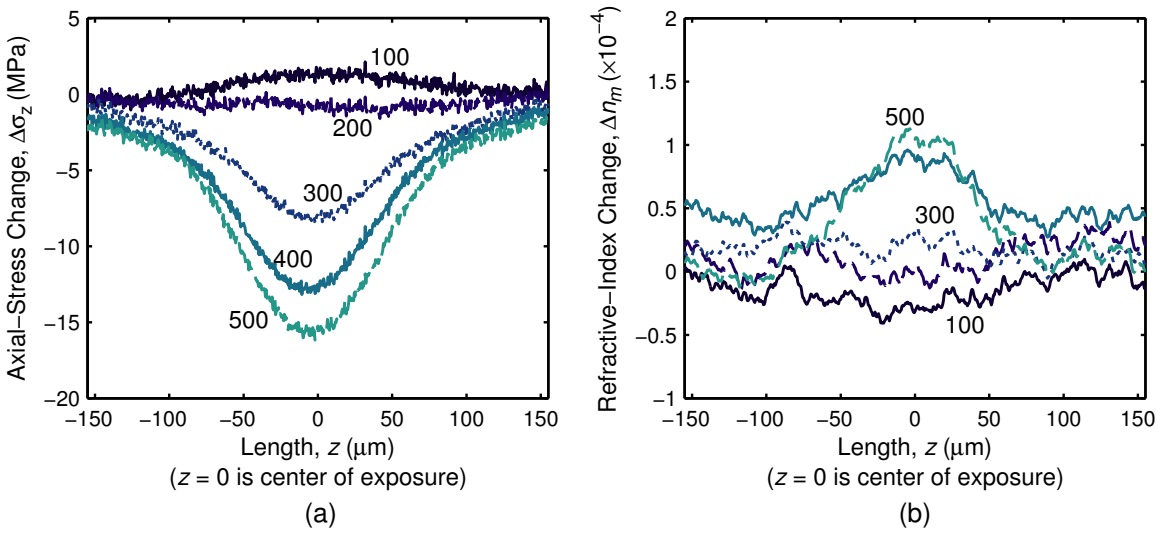

Figure 6.15: Longitudinal profiles of the axial-stress change (a) and the measured refractive-index change (b) in the cladding opposite the exposure at various exposure durations. The exposure durations are listed near their respective profiles.

6.3.5.2 Changes at the Center of the Exposure

The axial-stress change and the refractive-index change in the core at the longitudinal center of the exposure ($z = 0$) are shown as a function of exposure duration in Fig. 6.16. The axial-stress change, Fig. 6.16(a), shows a similar effect to that seen on the side of the fiber facing the exposure. The change for exposure durations greater than 100 ms follows a power-law trend. The equation that best fits the change is inserted in Fig. 6.16(a). The fit indicates that the axial-stress change is asymptotically approaching a minimum value of −36.9 MPa. This change is more than double the maximum change predicted for the side of the fiber facing the exposure and indicates

that a power-law fit may not be appropriate. The changes on the side opposite the exposure likely take longer to occur and may follow a more linear trend.

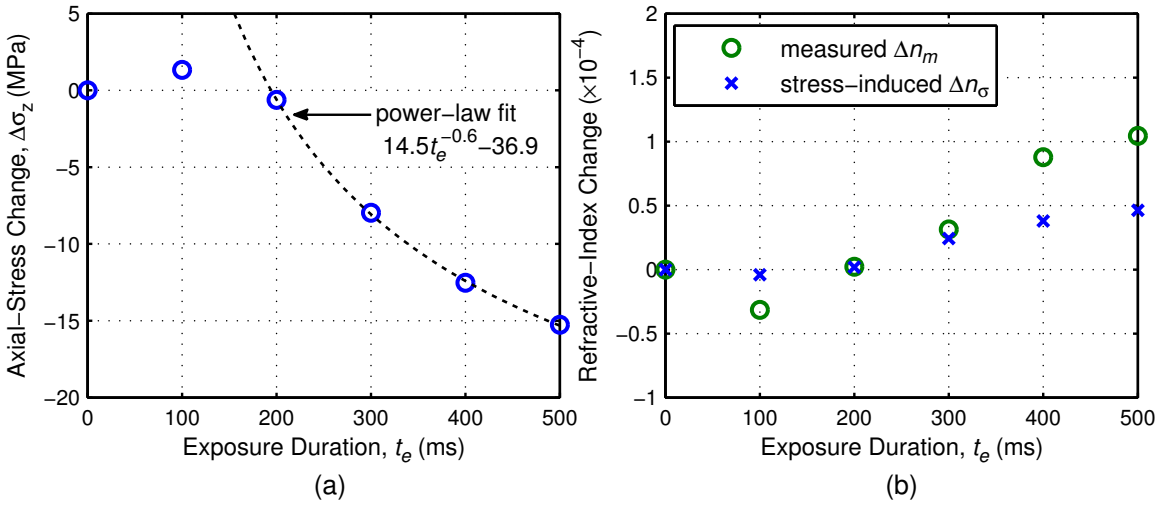

Figure 6.16: Changes in the cladding opposite the exposure at the longitudinal center of the exposure: (a) axial-stress changes and (b) measured index changes (circles) and predicted stress-induced index changes (x's). The change in the stress for exposure durations greater than 100 ms follows a power-law trend.

Unlike the cladding facing the exposure, the measured index changes opposite the exposure, shown with the circles in Fig. 6.16(b), are now similar to the predicted stress-induced index changes (x's). This verifies that very little annealing is occurring on the side of the fiber opposite the exposure and that stress relaxation is a primary source of the index modulation.

To verify the spatial extent of the relative contributions of the annealing-induced index changes and the stress-induced index changes, arrays of the stress-induced index change, $\Delta n_\sigma(x, y, z)$, and the measured index change, $\Delta n_m(x, y, z)$, at various longitudinal positions, z, for each exposed region of the incrementally exposed fiber are shown in Figs. 6.17 and 6.18. These figures show the same information as Figs. 6.9 and 6.10, however, the values of the measured index change shown in Fig. 6.18 are reduced compared to Fig. 6.10. This makes visible the small contributions of the stress-induced index changes to the total measured index change. However, noise in

the measured index change and artifacts from slight misalignments of the phase-shift profiles used to calculate the RIDs are more visible. The radial lines in the distributions are caused by misalignments of the phase-shift profiles, they are not actual features. Despite the noise and the artifacts, similar features can be seen in the stress-induced index change and the measured index change on the side of the fiber opposite the exposure. This is most clear for the longer exposure durations at the center of the exposure ($z = 0$).

6.4 Summary

When Davis *et al.* fabricated the first LPFGs in conventional fibers by exposure to focused CO_2 laser pulses, measurements of the RIP indicated an increase in the cladding refractive index on the side of the fiber facing the exposure [76]. It was hypothesized that stress relaxation and densification were responsible for the increase in the refractive index. Since then, theories of the formation of CO_2-laser-induced LPFGs have been expanded and a significant amount of theoretical and experimental evidence has been produced. However, the available information is insufficient to provide a complete understanding of the changes that occur during LPFG fabrication and to enable the modeling of LPFG behavior without assumptions about the functional form of the physical properties.

The results presented in this chapter verify many of the previous investigations and tie them together to present a more coherent picture of LPFG fabrication. In addition, the new evidence provides a further understanding of the dynamic changes that occur during fabrication. The theories and evidence from the previous and present results that provide insight into (1) the functional form of the physical properties and (2) the processes that occur during LPFG fabrication are summarized in Table 6.1.

In addition to providing a more coherent picture of LPFG fabrication, the results in this chapter provide immediate information for the modeling of LPFG behavior

and for understanding the limitations of LPFG fabrication in commercial optical fibers. The direct measurement of the RID provides the three-dimensional functional form of the index modulation. The cross-sectional form is related closely to the predicted cross-sectional laser intensity distribution (Fig. 6.1) [29]. The longitudinal form is Gaussian-like with a wide top and extends approximately ±100 µm from center of exposure. This is in contrast to the often assumed sinusoidal longitudinal form [85, 127, 128].

The two main processes that produce a CO_2-laser-induced index modulation are the relaxation of frozen-in viscoelasticity and mechanical stress relaxation. The maximum index modulation possible with these processes is directly related to the levels of frozen-in viscoelasticity and mechanical stress in the fiber. Variations in these draw-induced fiber properties between fiber manufacturers introduces a degree of freedom, but also limitations, when fabricating LPFGs in commercial optical fiber.

The results presented in this chapter also provide significant evidence for further investigation. Potential future research areas concerning CO_2-laser-induced LPFGs are discussed in the following chapter.

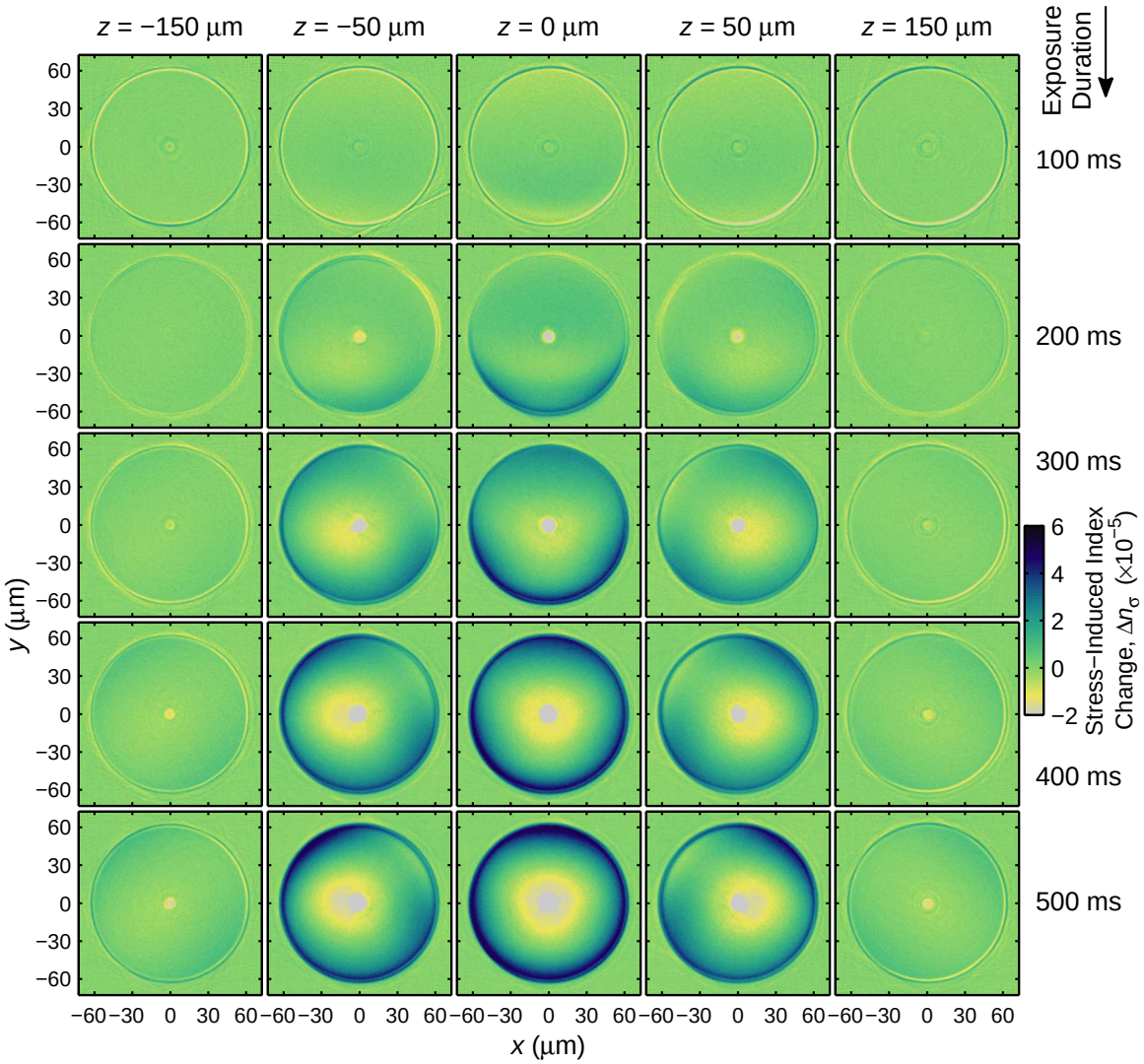

Figure 6.17: Distributions of the stress-induced index change at various longitudinal positions, z, in the exposed regions of the incrementally exposed fiber. The center column of distributions, labeled $z = 0$ µm, corresponds approximately to the longitudinal center of the exposure to the focused CO_2 laser. This figure is identical to Fig. 6.9.

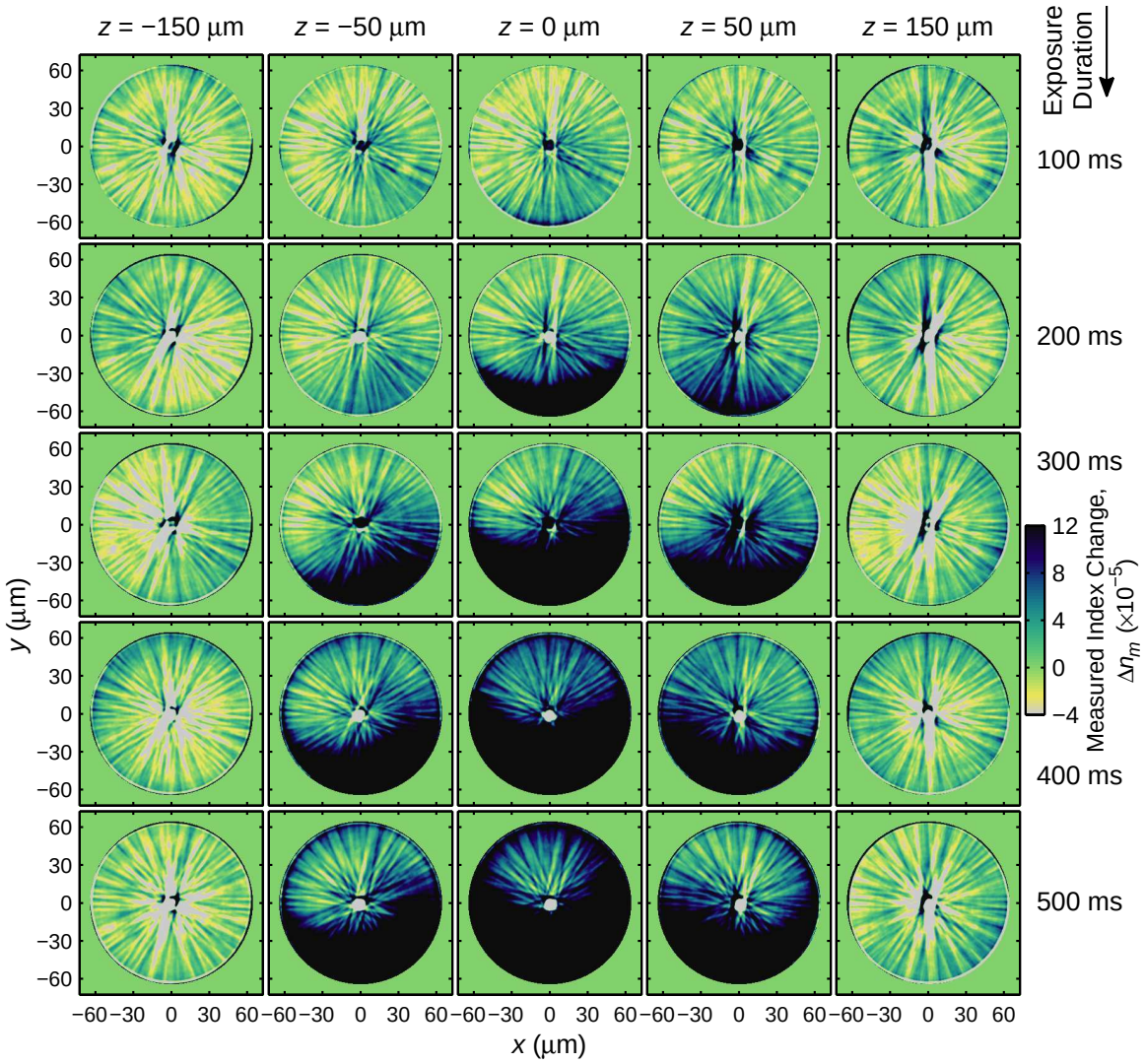

Figure 6.18: Distributions of the measured index change at various longitudinal positions, z, in the exposed regions of the incrementally exposed fiber. The center column of distributions, labeled $z = 0$ µm, corresponds approximately to the longitudinal center of the exposure to the focused CO_2 laser. This figure shows the same information as Fig. 6.10, however, the values of the measured index change shown are reduced to make visible the small contributions of the stress-induced index changes.

Table 6.1: Summary of the theories and evidence from the previous and present results that provide insight into the functional form of the physical properties and the processes that occur during fabrication of CO_2-laser-induced LPFGs.

Previous Theory	Previous Evidence	New Contribution
Stress relaxation and densification raise cladding index on side of fiber facing exposure [76]	• Index increase observed in measured RIP [76] • Modeling indicates that temperature in fiber exceeds fictive temperature [123] • Index increase inferred from FTIR measurement [86]	Laser-induced densification is primary source of cladding index increase on side facing exposure, mechanical stress relaxation contributes $< 10\%$, Fig. 6.14(b)
Mechanical stress relaxation lowers core index [119]	• Stress relaxation observed in measured residual-stress profile [22] • Index decrease inferred from interferometer-based measurements [23, 85]	Laser-induced mechanical stress relaxation is not ruled out as primary source of reduced core index, Fig. 6.12
One-sided exposure results in azimuthally asymmetric RID [76]	• Modeling indicates that laser intensity distribution is asymmetric [29] • Asymmetric RSD measured [24] • Asymmetric RID measured [79]	Azimuthal asymmetry in cross-sectional RID in cladding is related closely to laser intensity distribution, Fig. 6.5

New Theory and Evidence
Densification of cladding on side facing exposure is produced by CO_2-laser-induced annealing (relaxing) of frozen-in viscoelasticity formed during fiber drawing (manufacturing) process, Fig. 6.14(b) and [116]
Index modulation in cladding on side opposite exposure is weak and produced primarily by laser-induced mechanical stress relaxation, Figs. 6.16(b) and 6.18
Mechanical stress relaxation and densification respond to laser-induced thermal gradient that diffuses beyond exposed region, Figs. 6.11(a), 6.13, and 6.15
Longitudinal form of index modulation by densification is Gaussian-like with a wide top and extends approximately ± 100 µm from center of exposure, Fig. 6.13(b)

CHAPTER 7

CONCLUSIONS

The primary objective of this research was to provide a methodology that is capable of characterizing concurrently the three-dimensional residual-stress distributions (RSDs) and refractive-index distributions (RIDs) in optical fibers and fiber-based devices. This was accomplished by (1) extending the Brace-Köhler compensator (BKC) technique to enable the numerous retardation measurements necessary to characterize cross-sectional RSDs, (2) implementing the quantitative-phase microscopy (QPM) technique alongside the BKC technique for the concurrent characterization of RIDs, and (3) developing a custom measurement apparatus that enables the tomographic measurement of optical fibers and fiber-based devices using these techniques. The secondary objective of this research was to validate the methodology by characterizing both unperturbed and modified optical fibers, including carbon-dioxide-laser-induced long-period fiber gratings (CO_2-laser-induced LPFGs). This was accomplished by characterizing the RSD and the RID in a conventional telecommunications fiber (Corning SFM-28) in an unperturbed region, a region near a cleaved end-face, and regions exposed to focused pulses of CO_2 laser radiation. In this chapter, the main accomplishments are summarized and potential areas of future research are discussed.

7.1 Summary of Results

7.1.1 Review of Existing Characterization Techniques

The techniques available for the nondestructive characterization of the RSD in optical fibers were reviewed and the requirements for the accurate characterization of cross-sectional RSDs were discussed. The available photoelasticity techniques require the measurement of relative intensity distributions, which is generally not as accurate

as the measurement of minima or nulls of intensity provided by the compensator techniques. Furthermore, of the available compensator techniques, only the BKC technique has been shown to provide (1) the accuracy required to measure the small retardations (on the order of $\lambda/100$) produced by typical optical fibers and (2) a workable measurement duration for the characterization of cross-sectional RSDs.

The techniques available for the characterization of the cross-sectional RIDs in optical fibers were also reviewed. The axial techniques are inherently destructive because they require cleaving and polishing to prepare the end-face of the fiber. The interferometric techniques require the use of an interferometer and cannot be carried out on the same equipment as the RSD characterization techniques. Only the QPM technique (1) is capable of characterizing cross-sectional RIDs without perturbing the fiber or fiber-based device and (2) uses a standard microscope-based configuration. This crucial second requirement enables the simultaneous characterization of the RSD and the RID with one measurement apparatus.

7.1.2 Residual-Stress Characterization with the BKC Technique

The underlying theory of the BKC technique for the measurement of the retardation produced by optical fibers was discussed and extended to remove the need to use the small-retardation approximation. A measurement procedure was developed to obtain the numerous images required to determine full-field retardation maps of the fiber and data analysis procedures were developed to process the images. The underlying theory for the determination of cross-sectional RSDs was also presented. Additional data analysis procedures were developed to determine the cross-sectional RSDs from the retardation maps using computed tomography principles.

A measurement procedure was established to characterize the presence of birefringence and other effects in the imaging system. However, it was demonstrated that a single background measurement cannot account for any drift in the background

retardation that occurs during the several hours required to perform the measurements with the fiber. Therefore, a procedure was developed to detect and remove background retardations that cannot be accounted for with a single background measurement.

7.1.3 Refractive-Index Characterization with the QPM Technique

The underlying theory of the QPM technique for the measurement of the phase shift produced by optical fibers was presented. A measurement procedure was developed to obtain the numerous images required to determine full-field phase-shift maps of the fiber and data analysis procedures were established to process the images. The underlying theory for the determination of cross-sectional RIDs was also presented and additional data analysis procedures were developed to determine the cross-sectional RIDs from the phase-shift maps. The theory and the procedures were described in a manner analogous to those used with the BKC technique to exploit the complementary nature of these transverse, projection-based measurements.

Fluctuations in temperature were shown to result in variations in the measured phase shift that were caused by changes in the refractive index of the index-matching oil. These variations affect the accuracy of the calculated RID and must be minimized. A procedure was developed to minimize these temperature-induced variations during the time required to perform the numerous phase-shift measurements necessary to calculate the RID. Similar to the BKC technique, a procedure was also developed to characterize the presence of background phase shifts and other effects in the imaging system. It was shown that in addition to performing background measurements, efforts must be made to reduce image noise to suppress noise-induced artificial phase shifts.

The *a priori* optimal settings for the condenser numerical aperture (NA) and the defocus distance for the characterization of optical fibers using the QPM technique

were not clear. Measurements of the refractive-index profile (RIP) of an optical fiber, rather than the full RID, were used as a means of assessing rapidly the effect of the condenser NA and the defocus distance. However, there were several algorithms to compute the RIP from a phase-shift measurement and the *a priori* optimal settings for the algorithms were not clear. A study of three algorithms was conducted and it was determined that a Fourier-theory-based algorithm provided the overall best results. Guidelines for selecting the optimal settings for the Fourier algorithm were also presented. Measurements were performed on a Corning SMF-28 fiber with various settings of the condenser NA and the defocus distance. It was determined that a condenser NA of 0.4 and a defocus distance of 3 µm are optimal for the current measurement apparatus.

7.1.4 Measurement Apparatus for the Concurrent Characterization of the RSD and RID

An Olympus BX60 commercial microscope with polarization microscopy accessories was used to develop an apparatus to perform concurrently the BKC technique and the QPM technique. Custom components and controlling software were designed and implemented to enable the partially automated, tomographic measurement of optical fibers and fiber-based devices. A custom microscope stage plate was designed and fabricated to enable measurements at various angular orientations of the fiber while limiting the radial runout of the fiber during rotation. Custom coupling devices were also designed and fabricated to allow for computer control of the precise and repeated tasks of rotating the compensator and focusing/defocusing the optical fiber. This apparatus combined with the techniques discussed previously made possible the first concurrent measurements of the three-dimensional RSD and RID in optical fibers and fiber-based devices [87].

7.1.5 Experimental Verification

Measurements of the RSD in a Corning SMF-28 fiber in an unperturbed region, a region near a cleaved end-face, and a region exposed to CO_2 laser radiation were presented. The results indicate that the developed BKC technique and the measurement apparatus are capable of resolving small structural features and small variations in azimuthally asymmetric distributions of the axial stress. The measurement of the unperturbed fiber resolved the compressive stress at the core-cladding boundary that results from the presence of OH impurities introduced during the manufacture of the fiber preform. An analysis of the region surrounding the fiber was used to determine the noise in the retardation and the axial stress. The noise in the retardation was calculated to be ± 0.013 nm (at $\lambda = 546$ nm) and the noise in the axial stress was calculated to be ± 0.35 MPa. A comparison with other published profiles of the axial stress in Corning SMF-28 fiber gives an estimated accuracy of the axial stress of ± 0.27 MPa.

The measurement near the cleaved end-face provided the first evidence of the cross-sectional and longitudinal extents of the relaxation of mechanically induced stresses near the end-face. The measurement of the exposed region of the fiber demonstrated the capability of the technique to characterize an azimuthally asymmetric fiber. Furthermore, this measurement revealed laser-induced relaxation of mechanically induced stress as well as frozen-in viscoelasticity.

A measurement of the RID in an unperturbed Corning SMF-28 fiber was also presented. The measurement resolved the center dip in the core of the fiber that results from dopant burn off. An analysis of the region surrounding the fiber was used to determine the noise in the phase shift and the refractive index. The noise in the phase shift was calculated to be ± 2.84 nm (at $\lambda = 546$ nm) and the noise in the refractive index was calculated to be $\pm 2.34 \times 10^{-5}$. A comparison with other published profiles of the refractive index in Corning SMF-28 fiber gives an estimated

accuracy of the refractive index of $\pm 1.4 \times 10^{-4}$.

7.1.6 Characterization of CO_2-Laser-Induced LPFGs

The existing theories and evidence of the functional form of the physical properties in CO_2-laser-induced LPFGs and the processes that occur during LPFG fabrication were reviewed. The first measurements of the dynamic changes in the three-dimensional RSD and RID that occur during the fabrication of CO_2-laser-induced LPFGs were presented [91]. The measurements were performed on a fiber that was exposed in various regions to focused pulses from a CO_2 laser with incrementally increasing durations. The results verified many of the previous investigations and tied them together to present a more coherent picture of LPFG fabrication. The relative contributions of residual stress relaxation and densification were specified in various regions of the fiber. Densification was identified as the primary source of index modulation in the cladding on the side of the fiber facing the exposure to the CO_2 laser, while stress relaxation was observed to be the primary source in the core and on the side of the fiber opposite the exposure.

The results provide the first direct measurement of the three-dimensional functional form of the index modulation, which is necessary for the modeling of LPFG behavior. The limitations of LPFG fabrication in commercial optical fibers were also discussed. The two main processes that produce a CO_2-laser-induced index modulation are the relaxation of frozen-in viscoelasticity and mechanical stress relaxation. The maximum index modulation possible with these processes is directly related to the levels of frozen-in viscoelasticity and mechanical stress in the fiber. Variations in these draw-induced fiber properties between fiber manufacturers introduces a degree of freedom, but also limitations, when fabricating LPFGs in commercial optical fibers.

7.2 Future Work

While the results presented in this thesis verify the capabilities of the BKC technique, the QPM technique, and the experimental apparatus, more work is needed to realize their full potential. In addition, the results represent a small fraction of the unresolved issues in optical fiber and fiber-based device fabrication, operation, and performance. The future long-term goals of this research are that the transmission properties (loss, dispersion, polarization-dependent performance, etc.) of optical fibers and fiber-based devices will be predictable in terms of (1) the physical properties (RSD, RID, etc.) and (2) the fabrication/processing properties (preform characteristics, draw parameters, grating fabrication parameters, etc.). Potential areas of future research as they relate to these goals are discussed in the following sections.

7.2.1 RSD and RID Characterization Techniques

7.2.1.1 Defocus Distance Repeatability

As discussed in Sec. 6.3.3, variations in the defocus distance induced by the current defocusing apparatus result in variations in the calculated RIDs. These variations must be reduced, for example, to determine more accurately the changes in the core refractive index in fibers exposed to CO_2 laser radiation. A new defocusing apparatus consisting of a PI (Physik Instrumente) piezoelectric objective lens positioner (Model P-721.SL2) with a repeatability of ± 10 nm is currently available [129]. An Olympus objective lens turret has also been modified to accept the larger-diameter positioner. This new positioner needs to be installed and the current custom LabVIEW virtual instrument needs to be modified to control the positioner.

7.2.1.2 Modeling the Imaging of Optical Fibers

As discussed in Sec. 5.2.1, the QPM technique requires the careful selection of the condenser NA and the defocus distance used to obtain the needed defocused images of the optical fiber. These parameters were determined experimentally for the current

measurement apparatus by measuring and analyzing the RIP of a Corning SMF-28 fiber, however, they may change if other magnifications are used or fibers with different diameters are characterized. The optimal parameters must be predictable in terms of the expected sample configuration (diameter, refractive index, surrounding medium, etc.) and the imaging system properties (wavelength, numerical apertures, magnification, etc.). A possible starting point for this analysis is the modeling performed by Barty [99] and Barone-Nugent *et al.* [130].

7.2.1.3 Modeling the Effects of Refraction and Diffraction

The use of projection-based measurements and computed tomography principles requires the assumption that the impinging rays of light pass through the fiber sample undeviated. However, the inherent variations and asymmetries present in the RID of optical fibers will lead to refraction and diffraction, and thus a deviation of the impinging rays. The effect of refraction on the resulting residual-stress profiles of hollow-core fibers has been examined for low-magnification (20×) imaging [43], however, the effect on RSDs determined using tomographic measurements at higher magnifications (40×) has not been examined.

The influence of ray deviation on the phase-shift measurements made using the QPM technique is related to the optimal imaging parameters. The QPM technique relies on the measurement of the longitudinal derivative of the intensity of the light propagating through the microscope. Ray deviations are required to produce variations in the intensity. Therefore, modeling of the imaging of optical fibers to predict the optimal imaging parameters must take into account the impact of ray deviation on the computed tomography principles employed to determine the RID.

7.2.2 CO_2-Laser-Induced LPFGs

7.2.2.1 Modeling LPFG Behavior

The resonant wavelength of an LPFG can be estimated using the Bragg condition together with the calculated effective indices of guided modes in the fiber. The full transmission spectrum of an LPFG can be determined using coupled-mode theory [127]. However, without tailoring the optical fiber and LPFG modeling properties, both of these techniques have yet to provide simulated resonant wavelengths or spectra that are in good agreement with those observed in CO_2-laser-induced LPFGs [85,128]. The measurements performed on the incrementally exposed fiber provide the first direct measurement of the three-dimensional functional form of the index modulation. This data can be used with existing methods based on coupled-mode theory to model the behavior of LPFGs with arbitrary RIDs [127]. A starting point is to use the measured data to refine the radial, azimuthal, and longitudinal index variations used to model existing CO_2-laser-induced LPFGs with periods fabricated using a single continuous focused laser pulse. This is the first step to realizing the long-term goal of predicting the LPFG transmission properties in terms of the physical properties.

7.2.2.2 Investigation of CO_2-Laser-Induced Thermal Effects

The CO_2-laser-induced mechanical stress relaxation and densification were shown to respond to a laser-induced thermal gradient that diffuses beyond the exposed region. The time-dependent transverse extent of the densification and the longitudinal extent of both processes were measured for the first time. This provides experimental data that can be used to verify and refine efforts to model the laser-induced heat diffusion in an optical fiber. A starting point is the effort by Davis to model the transient longitudinal temperature distribution in a fiber exposed to a CO_2 laser pulse [131]. This work is a first step towards predicting the laser-induced changes in the physical properties in terms of the LPFG fabrication properties.

7.2.2.3 Characterization of Other Fabrication Parameters

The fibers exposed to CO_2 laser radiation that were characterized and presented in this thesis were exposed to a single continuous laser pulse. Bachim showed that the LPFG fabrication yield could be improved by using a series of multiple short-duration laser pulses per period [79]. A typical period was fabricated using 160 pulses with a period of 50 ms and duty cycle of 75%. This results in a total exposure time per period of 6000 ms, which is much longer than the typical 500 ms duration used for a single continuous pulse. The changes in the RSD and the RID that result from multiple short-duration pulses need to be examined to uncover the reasons for improved fabrication yeild.

7.2.3 Other Optical Fibers and Fiber-Based Devices

As optical fibers and fiber-based devices continue to advance, the need to understand their fundamental physical properties simultaneously increases. An understanding of their transmission properties alone is no longer sufficient for the design and optimization of emerging novel fiber types, communication components, and fiber-based sensors. Fiber and fiber-based device development must include a complete understanding of their physical properties to move beyond the limited capability of exclusively demonstrating their signal and sensing behaviors to modeling and optimizing their designs for specific applications. In addition to the CO_2-laser-induced LPFGs already discussed, additional areas to investigate using the measurement techniques and apparatus described in this thesis are suggested.

7.2.3.1 Multi-Core Optical Fibers

There are many compelling recent applications of multi-core optical fibers including; high-capacity multichannel data transmission [132]; high-power fiber lasers [133];

biomedical imaging and monitoring [134]; and multi-dimensional tilt [135], acceleration [136], and curvature sensing [137]. While these applications have been demonstrated and continue to be optimized, the modeling of multi-core fibers requires idealized assumptions about their structure or the observation of a cleaved end-face. As shown in Sec. 5.1.2, stress relaxation occurs near the end-face of a traditional telecommunications fiber. Therefore, stress relaxation will also be present in multi-core fibers and the cleaved end-face may not represent accurately the structure inside the fiber. The effects of diffraction and refraction on the projection-based measurement techniques discussed previously will be more significant in multi-core fibers than single-core fibers. In addition, fibers with air holes will require procedures such as injecting index-matching oil to permit the use of the projection-based measurements.

7.2.3.2 Optical Fiber Spinning

Polarization-division multiplexing is an optical technique that can be used to increase the capacity of an optical fiber by splitting a single-wavelength channel into two channels with orthogonal polarizations. However, polarization-mode dispersion (PMD) limits the data rate that can be achieved with this technique. The spinning of optical fibers during the draw process can be used to reduce PMD. The cross-sectional RSD in spun optical fibers has been characterized and the measurements revealed a decrease in the tensile stress in the core of a spun fiber relative to a fiber that was not spun [15, 16]. Longitudinal variations in the RSD in spun optical fibers have not been examined and no attempt has been made to characterize the RID. Longitudinal variations are required to verify the relationship between spin parameters and the resulting variation in the physical properties of the fiber.

7.3 Concluding Remarks

The measurement techniques and apparatus presented in this thesis allow the concurrent characterization of the RSD and the RID in optical fibers and fiber-based

devices. The need to transfer the fiber between two different pieces of equipment is eliminated and therefore the small and asymmetric changes in the RSD and the RID can be compared. To the best of the author's knowledge, this is the first time such a capability has been demonstrated. As optical fibers and fiber-based devices continue to advance in complexity and application, the optimization of their fabrication and performance by changing fabrication parameters and observing the results will become increasingly less effective. Furthermore, assumptions about the physical properties will have a larger impact on the capabilities of modeling as fiber structures become more complicated. The developed techniques and apparatus meet the need to characterize experimentally the fundamental physical properties in optical fibers and fiber-based devices. The impact of this capability was demonstrated by the measurements performed on fibers exposed to focused pulses of CO_2 laser radiation. The measurements verified and extended many of the previous investigations of fibers exposed to CO_2 laser radiation and provided new evidence that was not previously available. These measurements represent only a small fraction of the unresolved issues in optical fiber and fiber-based device fabrication, operation, and performance. The potential impact of the measurement techniques and apparatus is much larger.

APPENDIX A

OPTICAL FIBER END-FACE MIRROR

A.1 Introduction

Optical fiber-based sensors have attracted significant interest because of several advantages over other sensing methods. First, these sensors use the inherent advantages of optical fibers, including small size, immunity to electromagnetic interference, resistance to many hazardous chemicals, and remote monitoring capability. In addition, these sensors can exploit intrinsic optical properties as a means of detection. These characteristics (1) simplify sample processing by eliminating the need for a label or an indicator and (2) enable the sensor to make a more direct measurement by removing the need for an external or secondary means of detection. Additional advantages can be gained from the use of optical fiber-based sensors by placing the sensor at the end of the optical fiber. This eliminates the need to have access to both ends of the optical fiber, thus creating a more convenient and extremely compact probe-type sensor. Fiber-based sensors of this type have been developed using surface-plasmon resonance (SPR) effects [138–140], fiber-Bragg gratings (FBGs) [141], long-period fiber gratings (LPFGs) [142–144], tapered fibers [145, 146], and offset fibers [147].

Probe-type, fiber-based sensors require a reflective fiber-based device or a reflective end-face. FBGs are inherently reflective, however, other probe-type, fiber-based sensors require a reflective end-face. The reflection from the cleaved glass end-face can be used [146]. However, the fraction of the power reflected (reflectance) is less than 4% for an air-glass interface, and it decreases with an increase in the refractive index of the medium surrounding the fiber. Sputtering and evaporation are

commonly used to fabricate metallic and multi-layer dielectric mirrors with high reflectance [138–140, 142, 144, 147, 148]. These techniques can be used with a variety of materials, but they require access to specialized equipment and careful preparation of the fiber. The deposition of metallic silver from an aqueous solution (the mirror reaction using Tollen's reagent) has been used to fabricate end-face mirrors [149]. This technique does not require specialized equipment, but the solution must be prepared at the time it is needed and used immediately. Sputtering, evaporation, and the mirror reaction can also require long deposition times to achieve a sufficiently thick metallic layer. While these techniques can provide high-quality mirrors, the time-consuming preparation steps and procedures do not enable the rapid prototype fabrication and testing of novel probe-type, fiber-based devices and sensors.

A rapid mirror fabrication technique has been demonstrated previously by dipping the fiber into molten, low-melting-point metal alloys [150]. This technique requires only a heating element and commonly available metal alloys, such as tin-lead solder. However, the details of the technique were not provided and the requirements for the reliable and repeatable adhesion of the mirror were not reported. Furthermore, the reflectance of the mirrors was characterized using bulk optics for a wavelength of 633 nm. A reliable and repeatable technique to fabricate mirrors suitable for use with near-infrared telecommunications wavelengths is necessary for the development of probe-type, fiber-based devices and sensors.

In this appendix, an improved mirror fabrication technique based on the dipping technique is presented [92]. The new technique uses a small (a couple hundred micrometers thick, about 1 mm wide) puddle of molten metal to achieve reliable, reproducible adhesion of the metal to the fiber end-face. This is the first reported use of such a small amount of molten metal and it was observed that the small amount is crucial for reliable, reproducible mirror fabrication. The technique can be performed with the fiber in a horizontal orientation to enable the observation of the process

in a standard optical microscope. The broadband reflectance of the fabricated mirrors was measured using an all-fiber characterization system for wavelengths in the range of 1300−1600 nm. This is the first detailed characterization of fiber mirrors at telecommunications wavelengths. This technique permits the on-demand, rapid fabrication of mirrors with readily available equipment and minimal fiber preparation, and it enables the rapid prototyping and testing of probe-type, fiber-based devices and sensors.

A.2 Fabrication and Characterization

The cleaved end-face of a bare optical fiber was prepared using the following cleaning procedure: The end of the fiber was rinsed sequentially with isopropyl alcohol, deionized water, acetone, and deionized water. The fiber was then dried with forced air. The acetone rinse was required to ensure the adhesion of the metal to the fiber; a rinse with only isopropyl alcohol resulted in poor or no adhesion.

The configuration of the mirror fabrication technique is shown in Fig. A.1. The cleaved optical fiber was mounted on a horizontal translation stage on one side of a microscope. A soldering iron was mounted horizontally on the other side of the microscope. With the soldering iron tip in the field of view of the microscope and heated above the melting point of the metal, a small amount of metal was melted onto the tip. A readily available 60% tin, 40% lead solder was used for the mirrors presented in this thesis, however, other low-melting-point metal alloys can also be used. The amount of molten metal was limited to form a small, thin puddle that was only a couple hundred micrometers deep and approximately 1 mm wide. The size of the molten metal puddle relative to a 125-µm-diameter fiber is shown to scale in Fig. A.1(b). Next, the cleaved fiber was translated horizontally to push the end-face into the molten metal and then slowly withdraw it. For the metal to adhere to the fiber end face, the adhesion energy between the metal and the fiber must

exceed the surface energy of the molten metal. It is likely that the small puddle has a reduced surface energy compared to an open container of the molten metal (which consistently resulted in poor adhesion or no adhesion). The slow withdraw (a few seconds) is necessary to allow the metal on the fiber end-face to solidify and not be drawn back into the molten metal puddle.

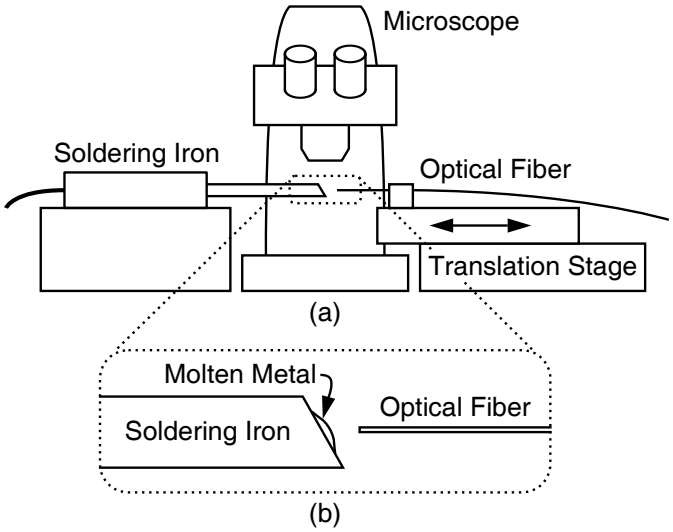

Figure A.1: Configuration of the mirror fabrication technique: (a) arrangement of the microscope, translation stage, and soldering iron; and (b) detailed view of the soldering iron tip, molten metal, and fiber. The optical fiber is translated horizontally into and out of the small puddle of molten metal.

The mirrors fabricated using this technique were characterized by visual inspection and by measuring their reflectance for wavelengths in the range of 1300−1600 nm. The reflectances were measured using the configuration shown in Fig. A.2. The reflectance of the mirror, R_M, was calculated as

$$R_M = \frac{P_{out}}{P_{in}\, T_{13}\, T_{32}}, \tag{A.1}$$

where P_{in} is the power of the broadband source, P_{out} is the power measured by the optical spectrum analyzer (OSA), and T_{mn} is the percent of the power transmitted (transmittance) from port m to port n of the 1×2 splitter. The transmittances were measured by connecting the source to port m, connecting the OSA to port n, and

immersing the end of the fiber from the unused port in an index matching oil to minimize reflections.

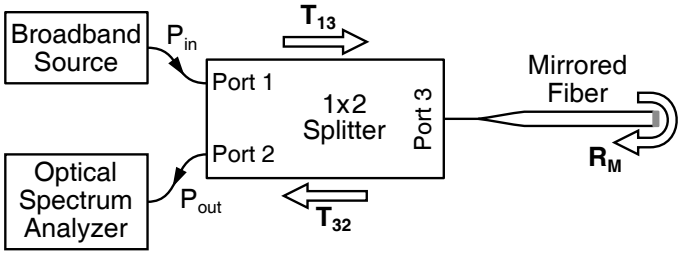

Figure A.2: Configuration for determining the reflectance of the mirrors. T_{mn} is the transmittance from port m to port n of the 1x2 splitter. R_M is the reflectance of the mirror.

A.3 Fabricated Mirrors

Images of a typical mirror fabricated using the presented technique are shown in Fig. A.3. The side view shows the tapered profile that results from slowly withdrawing the fiber from the molten metal. The tapered profile results in the diameter of the mirror being somewhat smaller than the diameter of the fiber. This permits the wiping and cleaning of the fiber without damaging or removing the mirror. The mirror required no special handling requirements above those necessary for a bare optical fiber. The end view of the mirrored end shows almost complete coverage of the end-face. Shown for reference is the end view of a bare end-face.

For test purposes, a series of five mirrors was fabricated according to the described process and their reflectances were measured. The average reflectance of the mirrors is shown in Fig. A.4. The reflectance of the mirrors is determined by the optical properties of the tin-lead alloy. The overall average reflectance is 69.7±5.9%. This is an 11.7% higher reflectance than the previously reported value of 58% for a tin-lead alloy [150]. This increase is attributed to the difference in wavelengths between the present result and [150] as well as the all-fiber characterization system shown in Fig. A.2.

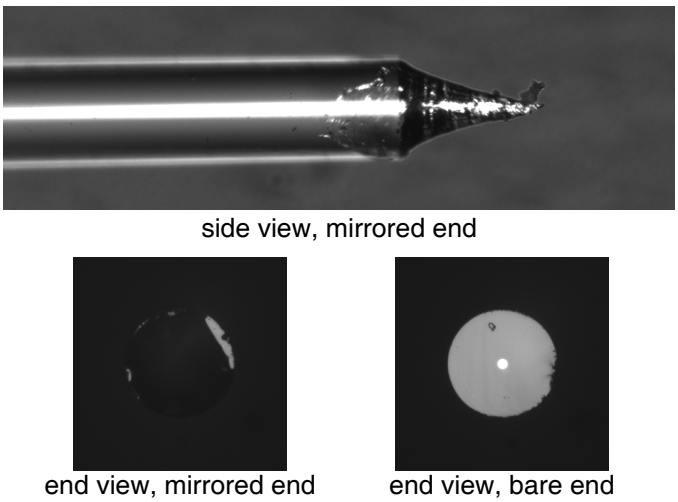

Figure A.3: Images of a typical mirror obtained using reflected-light microscopy (10× magnification). The side view shows a small amount of metal on the side of the fiber. The end view of the mirror shows almost complete coverage of the end-face. The bright spot in the center of the bare end is light from the microscope transmitted through the fiber and reflected by the mirror.

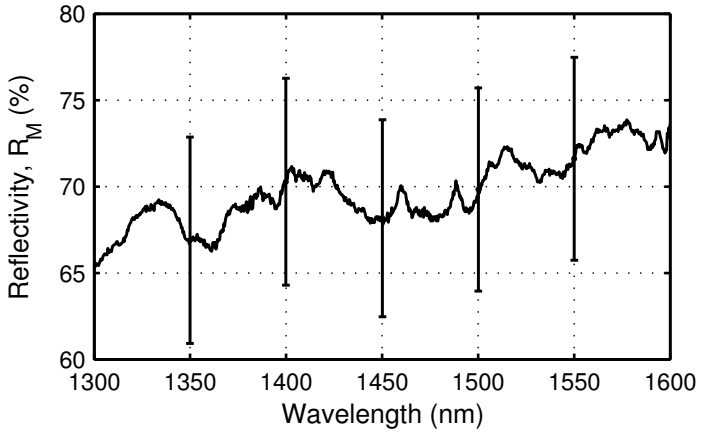

Figure A.4: Average reflectance of five mirrors. The error bars indicate the standard deviation of the reflectance of the five mirrors.

The reflectance of one of the five mirrors was measured again 448 days after fabrication to determine the long-term performance. The remeasured reflectance was higher by an overall average of 4.8%. This increase is attributed to better connections in the all-fiber characterization system rather than to age-related effects. The temperature dependence of the reflectance of one of the mirrors was also characterized for temperatures in the range of $10-74$ °C. A linear decrease in the reflectance was observed with an increase in the temperature. The decrease in the reflectance was also wavelength dependent. The smallest decrease was 0.7% at a wavelength of 1300 nm and the largest decrease was 1.6% at a wavelength of 1550 nm.

A.4 Example Device

To demonstrate the utility of this technique to prototype rapidly novel, probe-type devices, it was used to fabricate an end-of-fiber LPFG. Probe-type, LPFG-based interferometers have been developed by fabricating an LPFG near the mirrored end-face of an optical fiber [142, 143]. These devices require a short span ($40-50$ mm) of unperturbed fiber between the LPFG and the mirror to accumulate a phase difference between the cladding-guided modes and the core-guided mode. The need for shorter devices was addressed by developing a reflective LPFG [144]. This device uses a mirror on the cladding region of the fiber to reflect only the cladding guided modes, which are coupled back into the core on their second pass through the LPFG. This reduced the total length of the device to 26 mm.

In this thesis, a mirrored end-of-fiber LPFG is presented (introduced in Sec. 1.4.1). It was fabricated by cleaving a traditional LPFG and mirroring the resulting end-face. The LPFG was fabricated by exposing a Corning SMF-28 fiber to carbon-dioxide (CO_2) laser radiation using the configuration described in [32]. Before cleaving, the LPFG had 31 periods with a spacing of 640 µm. After cleaving, the end-of-fiber LPFG had only 11 periods, giving a device length of only 7 mm.

An image of the mirror and the two LPFG periods closest to the mirror was obtained using reflected-light, differential-interference-contrast (DIC) microscopy and is shown in Fig. A.5 (identical to Fig. 1.3). DIC microscopy allows the index modulation in the LPFG to be visualized. This technique also allows the precise placement of the LPFG in a fiber cleaver. The end-of-fiber LPFG shown in Fig. A.5 was cleaved just before period number 12. The response of the end-of-fiber LPFG was measured using the configuration shown in Fig. A.2. The response before mirroring (dashed line) and after mirroring (solid line) are shown in Fig. A.5. Also shown for reference with the dotted line is the transmission response of the LPFG before it was cleaved. The responses of the end-of-fiber LPFG have been normalized to the average mirror reflection spectrum shown in Fig. A.4 to isolate the effect of the LPFG structure.

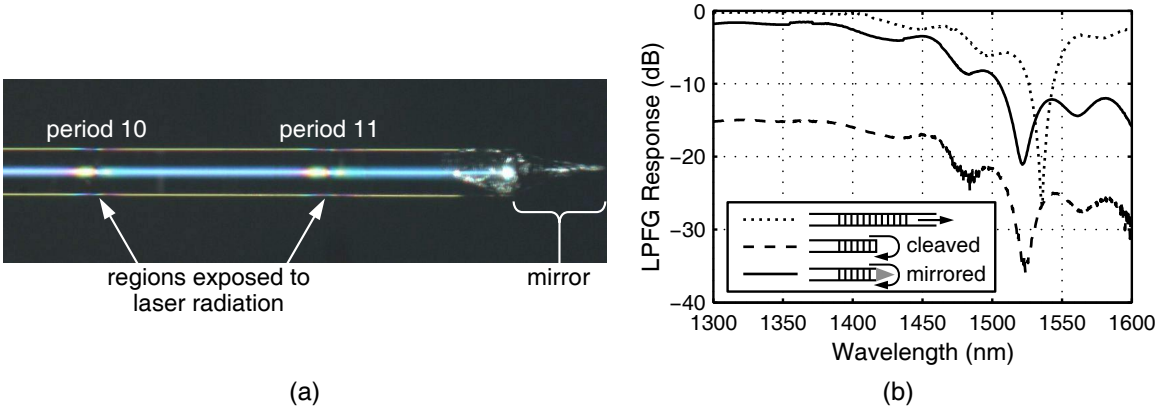

Figure A.5: End-of-fiber LPFG: (a) DIC microscopy image of the mirror and the two LPFG periods closest to the mirror (5× magnification); and (b) transmission response of the original LPFG (dotted line), the cleaved end-of-fiber LPFG (dashed line), and the mirrored end-of-fiber LPFG (solid line). The end-of-fiber LPFG features the band-rejection characteristics of a typical traditional LPFG.

The original LPFG had a resonant wavelength of 1536.1 nm. The end-of-fiber LPFG has a resonant wavelength of 1521.5 nm. The shift in the measured resonant wavelength after cleaving is primarily caused by the conditions under which the grating is characterized. The original LPFG was fabricated by exposing one side of the fiber to the CO_2 laser radiation. Furthermore, the fiber was held with a small amount

of tension during fabrication to ensure the repeatability of the process. These fabrication conditions result in LPFGs with azimuthally asymmetric refractive-index distributions, and they are sensitive to strain, bending, and bending direction [29, 30, 32]. The original LPFG was characterized with the LPFG held with a small amount of tension and no bending. However, the end-of-fiber LPFG was characterized with no tension. The shift in the measured resonant wavelength after cleaving is primarily caused by the lack of tension in the end-of-fiber LPFG. The resulting difference in the resonant wavelengths further indicates the sensitivity of these devices to strain, bending, and bending direction.

A.5 Summary

The fabrication of efficient, inexpensive optical fiber end-face mirrors was demonstrated by dipping the fiber into a small puddle of molten metal to achieve reliable, reproducible adhesion of the metal to the fiber end-face. The technique can be performed with the fiber in a horizontal orientation to enable the observation of the process in a standard optical microscope. The average reflectance of five mirrors fabricated using this technique is 69.7±5.9% for wavelengths in the range of 1300−1600 nm. This technique permits the on-demand, rapid fabrication of mirrors with readily available equipment and minimal fiber preparation, and it enables the rapid prototyping and testing of probe-type, fiber-based devices and sensors. Further, the fabrication of a novel, end-of-fiber LPFG was demonstrated. This probe-type device features the band-rejection characteristics of a traditional LPFG with a length of only 7 mm.

REFERENCES

[1] J. Yu and X. Zhou, "Ultra-high-capacity DWDM transmission system for 100G and beyond," *IEEE Commun. Mag.*, vol. 48, pp. S56–S64, Mar. 2010.

[2] P. R. Watekar, S. Ju, and W. T. Han, "Design and development of a trenched optical fiber with ultra-low bending loss," *Opt. Express*, vol. 17, pp. 10350–10363, June 8, 2009.

[3] L. Eldada, "Optical communication components," *Rev. Sci. Instrum.*, vol. 75, pp. 575–593, Mar. 2004.

[4] U. C. Paek and C. R. Kurkjian, "Calculation of cooling rate and induced stresses in drawing of optical fibers," *J. Am. Ceram. Soc.*, vol. 58, pp. 330–335, July/Aug. 1975.

[5] A. D. Yablon, "Optical and mechanical effects of frozen-in stresses and strains in optical fibers," *IEEE J. Sel. Topics Quantum Electron.*, vol. 10, pp. 300–311, Mar./Apr. 2004.

[6] K. Brugger, "Effect of thermal stress on refractive index in clad fibers," *Appl. Opt.*, vol. 10, pp. 437–438, Feb. 1971.

[7] G. W. Scherer, "Stress-induced index profile distortion in optical waveguides," *Appl. Opt.*, vol. 19, pp. 2000–2006, June 15, 1980.

[8] Y. Hibino, F. Hanawa, and M. Horiguchi, "Drawing-induced residual stress effects on optical characteristics in pure-silica-core single-mode fibers," *J. Appl. Phys.*, vol. 65, pp. 30–34, Jan. 1, 1989.

[9] P. L. Chu and T. Whitbread, "Stress modification in optical fibre," *Electron. Lett.*, vol. 20, pp. 449–450, May 24, 1984.

[10] P. C. P. Bouten, W. Hermann, C. M. G. Jochem, and D. U. Weichert, "Drawing influence on the lifetime of optical fibres," *J. Lightwave Technol.*, vol. 7, pp. 555–559, Mar. 1989.

[11] S. M. Oh, P. H. Predieux, and X. G. Glavas, "Increased durability of optical fiber through the use of compressive cladding," *Opt. Lett.*, vol. 7, pp. 241–243, May 1982.

[12] D. I. Yeom, H. S. Kim, M. S. Kang, H. S. Park, and B. Y. Kim, "Narrow-bandwidth all-fiber acoustooptic tunable filter with low polarization-sensitivity," *IEEE Photon. Technol. Lett.*, vol. 17, pp. 2646–2648, Dec. 2005.

[13] J. A. Buck, *Fundamentals of Optical Fibers*. Hoboken, N.J.: John Wiley and Sons, 2004.

[14] Y. Park, U.-C. Paek, and D. Y. Kim, "Determination of stress-induced intrinsic birefringence in a single-mode fiber by measurement of the two-dimensional stress profile," *Opt. Lett.*, vol. 27, pp. 1291–1293, Aug. 1, 2002.

[15] M. Ferrario, S. M. Pietralunga, M. Torregiani, and M. Martinelli, "Modification of local stress-induced birefringence in low-PMD spun fibers evaluated by high-resolution optical tomography," *IEEE Photon. Technol. Lett.*, vol. 16, pp. 2634–2636, Dec. 2004.

[16] S. M. Pietralunga, M. Ferrario, M. Tacca, and M. Martinelli, "Local birefringence in unidirectionally spun fibers," *J. Lightwave Technol.*, vol. 24, pp. 4030–4038, Nov. 2006.

[17] Y. Park, U.-C. Paek, and D. Y. Kim, "Complete determination of the stress tensor of a polarization-maintaining fiber by photoelastic tomography," *Opt. Lett.*, vol. 27, pp. 1217–1219, July 15, 2002.

[18] I. H. Shin, B. H. Kim, S. P. Veetil, W. T. Han, and D. Y. Kim, "Residual stress relaxation in cleaved fibers," *Opt. Commun.*, vol. 281, pp. 75–79, Jan. 1, 2008.

[19] P. Y. Fonjallaz, H. G. Limberger, R. P. Salathe, F. Cochet, and B. Leuenberger, "Tension increase correlated to refractive-index change in fibers containing UV-written Bragg gratings," *Opt. Lett.*, vol. 20, pp. 1346–1348, June 1, 1995.

[20] H. G. Limberger, C. Ban, R. P. Salathe, S. A. Slattery, and D. N. Nikogosyan, "Absence of UV-induced stress in Bragg gratings recorded by high-intensity 264 nm laser pulses in a hydrogenated standard telecom fiber," *Opt. Express*, vol. 15, pp. 5610–5615, Apr. 30, 2007.

[21] N. Belhadj, Y. Park, S. LaRochelle, K. Dossou, and J. Azana, "UV-induced modification of stress distribution in optical fibers and its contribution to Bragg grating birefringence," *Opt. Express*, vol. 16, pp. 8727–8741, June 9, 2008.

[22] B. H. Kim, Y. Park, T. J. Ahn, D. Y. Kim, B. H. Lee, Y. Chung, U. C. Paek, and W. T. Han, "Residual stress relaxation in the core of optical fiber by CO_2 laser irradiation," *Opt. Lett.*, vol. 26, pp. 1657–1659, Nov. 1, 2001.

[23] B. H. Kim, T. J. Ahn, D. Y. Kim, B. H. Lee, Y. Chung, U. C. Paek, and W. T. Han, "Effect of CO_2 laser irradiation on the refractive-index change in optical fibers," *Appl. Opt.*, vol. 41, pp. 3809–3815, July 1, 2002.

[24] H. S. Ryu, Y. Park, S. T. Oh, Y. J. Chung, and D. Y. Kim, "Effect of asymmetric stress relaxation on the polarization-dependent transmission characteristics of a CO_2 laser-written long-period fiber grating," *Opt. Lett.*, vol. 28, pp. 155–157, Feb. 1, 2003.

[25] F. Durr, H. G. Limberger, R. P. Salathe, F. Hindle, M. Douay, E. Fertein, and C. Przygodzki, "Tomographic measurement of femtosecond-laser induced stress changes in optical fibers," *Appl. Phys. Lett.*, vol. 84, pp. 4983–4985, June 14, 2004.

[26] F. Durr, G. Rego, P. V. S. Marques, S. L. Semjonov, E. M. Dianov, H. G. Limberger, and R. P. Salathe, "Tomographic stress profiling of arc-induced long-period fiber gratings," *J. Lightwave Technol.*, vol. 23, pp. 3947–3953, Nov. 2005.

[27] A. D. Yablon, M. F. Yan, D. J. DiGiovanni, M. E. Lines, S. L. Jones, D. N. Ridgway, G. A. Sandels, I. A. White, P. Wisk, F. V. DiMarcello, E. M. Monberg, and J. Jasapara, "Frozen-in viscoelasticity for novel beam expanders and high-power connectors," *J. Lightwave Technol.*, vol. 22, pp. 16–23, Jan. 2004.

[28] A. C. O. Chan and M. Premaratne, "Dispersion-compensating fiber Raman amplifiers with step, parabolic, and triangular refractive index profiles," *J. Lightwave Technol.*, vol. 25, pp. 1190–1197, May 2007.

[29] G. D. VanWiggeren, T. K. Gaylord, D. D. Davis, E. Anemogiannis, B. D. Garrett, M. I. Braiwish, and E. N. Glytsis, "Axial rotation dependence of resonances in curved CO_2-laser-induced long-period fibre gratings," *Electron. Lett.*, vol. 36, pp. 1354–1355, Aug. 3, 2000.

[30] G. D. VanWiggeren, T. K. Gaylord, D. D. Davis, M. I. Braiwish, E. N. Glytsis, and E. Anemogiannis, "Tuning, attenuating, and switching by controlled flexure of long-period fiber gratings," *Opt. Lett.*, vol. 26, pp. 61–63, Jan. 15, 2001.

[31] Y. P. Wang, Y. J. Rao, Z. L. Ran, T. Zhu, and A. Z. Hu, "A novel tunable gain equalizer based on a long-period fiber grating written by high-frequency CO_2 laser pulses," *IEEE Photon. Technol. Lett.*, vol. 15, pp. 251–253, Feb. 2003.

[32] M. I. Braiwish, B. L. Bachim, and T. K. Gaylord, "Prototype CO_2 laser-induced long-period fiber grating variable optical attenuators and optical tunable filters," *Appl. Opt.*, vol. 43, pp. 1789–1793, Mar. 20, 2004.

[33] Y.-J. Rao, Y.-P. Wang, Z.-L. Ran, and T. Zhu, "Novel fiber-optic sensors based on long-period fiber gratings written by high-frequency CO_2 laser pulses," *J. Lightwave Technol.*, vol. 21, pp. 1320–1327, May 2003.

[34] Y. P. Wang, D. N. Wang, W. Jin, and Y. J. Rao, "Asymmetric transverse-load characteristics and polarization dependence of long-period fiber gratings written by a focused CO_2 laser," *Appl. Opt.*, vol. 46, pp. 3079–3086, June 1, 2007.

[35] P. L. Chu and T. Whitbread, "Measurement of stresses in optical fiber and preform," *Appl. Opt.*, vol. 21, pp. 4241–4245, Dec. 1, 1982.

[36] T. Abe, Y. Mitsunaga, and H. Koga, "Photoelastic computer tomography: A novel measurement method for axial residual stress profile in optical fibers," *J. Opt. Soc. Am. A*, vol. 3, pp. 133–138, Jan. 1986.

[37] T. Colomb, F. Durr, E. Cuche, P. Marquet, H. G. Limberger, R. P. Salathe, and C. Depeursinge, "Polarization microscopy by use of digital holography: Application to optical-fiber birefringence measurements," *Appl. Opt.*, vol. 44, pp. 4461–4469, July 20, 2005.

[38] L. Bruno, L. Pagnotta, and A. Poggialini, "A full-field method for measuring residual stresses in optical fiber," *Opt. Lasers Eng.*, vol. 44, pp. 577–588, June 2006.

[39] P. Kniazewski, T. Kozacki, and M. Kujawinska, "Inspection of axial stress and refractive index distribution in polarization-maintaining fiber with tomographic methods," *Opt. Lasers Eng.*, vol. 47, pp. 259–263, Feb. 2009.

[40] B. Sevigny, F. Busque, N. Godbout, S. Lacroix, and M. Faucher, "High-resolution refractive index anisotropy measurement in optical fibers through phase retardation modulation," *Appl. Opt.*, vol. 47, pp. 1215–1222, Mar. 20, 2008.

[41] K. W. Raine, R. Feced, S. E. Kanellopoulos, and V. A. Handerek, "Measurement of axial stress at high spatial resolution in ultraviolet-exposed fibers," *Appl. Opt.*, vol. 38, pp. 1086–1095, Mar. 1, 1999.

[42] Y. Park, T.-J. Ahn, Y. H. Kim, W.-T. Han, U. C. Paek, and D. Y. Kim, "Measurement method for profiling the residual stress and the strain-optic coefficient of an optical fiber," *Appl. Opt.*, vol. 41, pp. 21–26, Jan. 1, 2002.

[43] Y. Park, S. Choi, U.-C. Paek, K. Oh, and D. Y. Kim, "Measurement method for profiling the residual stress of an optical fiber: Detailed analysis of off-focusing and beam-deflection effects," *Appl. Opt.*, vol. 42, pp. 1182–1190, Mar. 1, 2003.

[44] C. C. Montarou and T. K. Gaylord, "Two-wave-plate compensator method for single-point retardation measurements," *Appl. Opt.*, vol. 43, pp. 6580–6595, Dec. 20, 2004.

[45] C. C. Montarou, T. K. Gaylord, B. L. Bachim, A. I. Dachevski, and A. Agarwal, "Two-wave-plate compensator method for full-field retardation measurements," *Appl. Opt.*, vol. 45, pp. 271–280, Jan. 10, 2006.

[46] C. C. Montarou, T. K. Gaylord, and A. I. Dachevski, "Residual stress profiles in optical fibers determined by the two-waveplate-compensator method," *Opt. Commun.*, vol. 265, pp. 29–32, Sept. 1, 2006.

[47] N. H. Hartshorne and A. Stuart, *Crystals and the Polarising Microcope, A Handbook for Chemists and Others*. London: Edward Arnold Ltd., 1960.

[48] C. C. Montarou, *Low-Level Birefringence Measurement Methods Applied to The Characterization of Optical Fibers and Interconnects*. PhD thesis, Georgia Institute of Technology, Atlanta, GA, Apr. 2005.

[49] M. Young, "Optical fiber index profiles by the refracted-ray method (refracted near-field scanning)," *Appl. Opt.*, vol. 20, pp. 3415–3422, Oct. 1, 1981.

[50] N. H. Fontaine and M. Young, "Two-dimensional index profiling of fibers and waveguides," *Appl. Opt.*, vol. 38, pp. 6836–6844, Nov. 20, 1999.

[51] M. Ikeda, M. Tateda, and H. Yoshikiyo, "Refractive index profile of a graded index fiber: Measurement by a reflection method," *Appl. Opt.*, vol. 14, pp. 814–815, Apr. 1975.

[52] Y. Youk and D. Y. Kim, "A simple reflection-type two-dimensional refractive index profile measurement technique for optical waveguides," *Opt. Commun.*, vol. 262, pp. 206–210, June 15, 2006.

[53] Y. Youk and D. Y. Kim, "Tightly focused epimicroscope technique for submicrometer-resolved highly sensitive refractive index measurement of an optical waveguide," *Appl. Opt.*, vol. 46, pp. 2949–2953, May 20, 2007.

[54] Q. Zhong and D. Inniss, "Characterization of the lightguiding structure of optical fibers by atomic force microscopy," *J. Lightwave Technol.*, vol. 12, pp. 1517–1523, Sept. 1994.

[55] S. T. Huntington, P. Mulvaney, A. Roberts, K. A. Nugent, and M. Bazylenko, "Atomic force microscopy for the determination of refractive index profiles of optical fibers and waveguides: A quantitative study," *J. Appl. Phys.*, vol. 82, pp. 2730–2734, Sept. 15, 1997.

[56] H. M. Presby, W. Mammel, and R. M. Derosier, "Refractive index profiling of graded index optical fibers," *Rev. Sci. Instrum.*, vol. 47, pp. 348–352, Mar. 1976.

[57] H. M. Presby, D. Marcuse, and H. W. Astle, "Automatic refractive-index profiling of optical fibers," *Appl. Opt.*, vol. 17, pp. 2209–2214, July 15, 1978.

[58] L. M. Boggs, H. M. Presby, and D. Marcuse, "Rapid automatic index profiling of whole-fiber samples. I," *Bell Sys. Tech. J.*, vol. 58, pp. 867–882, Apr. 1979.

[59] H. M. Presby, D. Marcuse, H. W. Astle, and L. M. Boggs, "Rapid automatic index profiling of whole-fiber samples. II," *Bell Sys. Tech. J.*, vol. 58, pp. 883–902, Apr. 1979.

[60] B. L. Bachim and T. K. Gaylord, "Microinterferometric optical phase tomography measuring small, asymmetric refractive-index differences in the profiles of optical fibers and fiber devices," *Appl. Opt.*, vol. 44, pp. 316–327, Jan. 20, 2005.

[61] B. L. Bachim, T. K. Gaylord, and S. C. Mettler, "Refractive-index profiling of azimuthally asymmetric optical fibers by microinterferometric optical phase tomography," *Opt. Lett.*, vol. 30, pp. 1126–1128, May 25, 2005.

[62] M. Sochacka, "Optical fibers profiling by phase-stepping transverse interferometry," *J. Lightwave Technol.*, vol. 12, pp. 19–23, Jan. 1994.

[63] A. D. Yablon, "Multi-wavelength optical fiber refractive index profiling by spatially resolved Fourier transform spectroscopy," *J. Lightwave Technol.*, vol. 28, pp. 360–364, Feb. 2010.

[64] P. R. Griffiths and J. A. de Haseth, *Fourier Transform Infrared Spectroscopy.* New York: Jon Wiley and Sons, 1986.

[65] A. Barty, K. A. Nugent, D. Paganin, and A. Roberts, "Quantitative optical phase microscopy," *Opt. Lett.*, vol. 23, pp. 817–819, June 1, 1998.

[66] M. R. Teague, "Deterministic phase retrieval: A Green's function solution," *J. Opt. Soc. Am.*, vol. 73, pp. 1434–1441, Nov. 1983.

[67] A. Barty, K. A. Nugent, A. Roberts, and D. Paganin, "Quantitative phase tomography," *Opt. Commun.*, vol. 175, pp. 329–336, Mar. 1, 2000.

[68] N. M. Dragomir, G. W. Baxter, and A. Roberts, "Phase-sensitive imaging techniques applied to optical fibre characterisation," *IEE Proc. Optoelectron.*, vol. 153, pp. 217–221, Oct. 2006.

[69] N. M. Dragomir, X. M. Goh, C. L. Curl, L. M. D. Delbridge, and A. Roberts, "Quantitative polarized phase microscopy for birefringence imaging," *Opt. Express*, vol. 15, pp. 17690–17698, Dec. 24, 2007.

[70] A. M. Vengsarkar, P. J. Lemaire, J. B. Judkins, V. Bhatia, T. Erdogan, and J. E. Sipe, "Long-period fiber gratings as band-rejection filters," *J. Lightwave Technol.*, vol. 14, pp. 58–65, Jan. 1996.

[71] A. M. Vengsarkar, J. R. Pedrazzani, J. B. Judkins, P. J. Lemaire, N. S. Bergano, and C. R. Davidson, "Long-period fiber-grating-based gain equalizers," *Opt. Lett.*, vol. 21, pp. 336–338, Mar. 1, 1996.

[72] D. B. Stegall and T. Erdogan, "Dispersion control with use of long-period fiber gratings," *J. Opt. Soc. Am. A*, vol. 17, pp. 304–312, Feb. 2000.

[73] Q. Li, C. H. Lin, A. A. Au, and H. P. Lee, "Compact all-fibre on-line power monitor via core-to-cladding mode coupling," *Electron. Lett.*, vol. 38, pp. 1013–1015, Aug. 29, 2002.

[74] K. S. Chiang, "Development of long-period fiber grating coupling devices," *Appl. Opt.*, vol. 48, pp. F61–F67, Sept. 1, 2009.

[75] S. W. James and R. P. Tatam, "Optical fibre long-period grating sensors: Characteristics and application," *Meas. Sci. Technol.*, vol. 14, pp. R49–R61, May 2003.

[76] D. D. Davis, T. K. Gaylord, E. N. Glytsis, S. G. Kosinski, S. C. Mettler, and A. M. Vengsarkar, "Long-period fibre grating fabrication with focused CO_2 laser pulses," *Electron. Lett.*, vol. 34, pp. 302–303, Feb. 5, 1998.

[77] D. D. Davis, T. K. Gaylord, E. N. Glytsis, and S. C. Mettler, "Very-high-temperature stable CO_2-laser-induced long-period fibre gratings," *Electron. Lett.*, vol. 35, pp. 740–742, Apr. 29, 1999.

[78] T. Zhu, Y.-J. Rao, J.-L. Wang, and Y. Song, "A highly sensitive fiber-optic refractive index sensor based on an edge-written long-period fiber grating," *IEEE Photon. Technol. Lett.*, vol. 19, pp. 1946–1948, Dec. 15, 2007.

[79] B. L. Bachim, *Characteristics, Applications, and Properties of Carbon-Dioxide-Laser-Induced Long-Period Fiber Gratings.* PhD thesis, Georgia Institute of Technology, Atlanta, GA, June 2005.

[80] M. R. Hutsel, R. Ingle, and T. K. Gaylord, "Chemical sensing attributes of CO_2-laser-induced long-period fiber gratings," in *Frontiers in Optics*, Rochester, NY, FThE2, Oct. 23, 2008.

[81] M. R. Hutsel and T. K. Gaylord, "End-of-fiber long-period fiber grating-based sensors," in *Frontiers in Optics*, San Jose, CA, FTuE7, Oct. 13, 2009.

[82] D. D. Davis, T. K. Gaylord, E. N. Glytsis, and S. C. Mettler, "CO_2 laser-induced long-period fibre gratings: Spectral characteristics, cladding modes and polarisation independence," *Electron. Lett.*, vol. 34, pp. 1416–1417, July 9, 1998.

[83] B. L. Bachim and T. K. Gaylord, "Polarization-dependent loss and birefringence in long-period fiber gratings," *Appl. Opt.*, vol. 42, pp. 6816–6823, Dec. 1, 2003.

[84] H. M. Chan, F. Alhassen, I. V. Tomov, and H. P. Lee, "Fabrication and mode identification of compact long-period gratings written by CO_2 laser," *IEEE Photon. Technol. Lett.*, vol. 20, pp. 611–613, Apr. 15, 2008.

[85] Y. J. Li, T. Wei, J. A. Montoya, S. V. Saini, X. W. Lan, X. L. Tang, J. H. Dong, and H. Xiao, "Measurement of CO_2-laser-irradiation-induced refractive index modulation in single-mode fiber toward long-period fiber grating design and fabrication," *Appl. Opt.*, vol. 47, pp. 5296–5304, Oct. 10, 2008.

[86] T. Hirose, K. Saito, and K. Takada, "Mid-infrared spectroscopic detection of refractive index in CO_2 laser-written long-period fibre grating," *Electron. Lett.*, vol. 44, pp. 1187–1189, Sept. 25, 2008.

[87] M. R. Hutsel and T. K. Gaylord, "Concurrent, three-dimensional characterization of the refractive-index and residual-stress distributions in optical fibers," *Appl. Opt.*, (in preparation).

[88] M. R. Hutsel, R. R. Ingle, and T. K. Gaylord, "Accurate cross-sectional stress profiling of optical fibers," *Appl. Opt.*, vol. 48, pp. 4985–4995, Sept. 10, 2009.

[89] M. R. Hutsel, R. R. Ingle, and T. K. Gaylord, "Technique and apparatus for accurate cross-sectional stress profiling of optical fibers," *IEEE Trans. Instrum. Meas.*, vol. 60, pp. 971–979, Mar. 2011.

[90] M. R. Hutsel, C. C. Montarou, A. I. Dachevski, and T. K. Gaylord, "Algorithm performance in the determination of the refractive-index profile of optical fibers," *Appl. Opt.*, vol. 47, pp. 760–767, Feb. 20, 2008.

[91] M. R. Hutsel and T. K. Gaylord, "Residual stress relaxation and densification in CO_2-laser-induced long-period fiber gratings," *Appl. Opt.*, (in preparation).

[92] M. R. Hutsel and T. K. Gaylord, "Efficient, inexpensive optical fiber end-face mirror," *Opt. Commun.*, (in preparation).

[93] National Instruments Corp., Austin, Texas.

[94] H. Aben, *Photoelasticity of Glass*. Berlin: Springer-Verlag, 1993.

[95] J. Hsieh, *Computed Tomography: Principles, Design, Artifacts, and Recent Advances*. Bellingham, WA: SPIE Press, 2003.

[96] The Mathworks, Inc., Natick, Massachusetts.

[97] D. A. Viskoe and G. W. Donohoe, "Optimal computed tomography data acquisition techniques and filter selection for detection of small density variations," *IEEE Trans. Instrum. Meas.*, vol. 45, pp. 70–76, Feb. 1996.

[98] D. Paganin and K. A. Nugent, "Noninterferometric phase imaging with partially coherent light," *Phys. Rev. Lett.*, vol. 80, pp. 2586–2589, Mar. 23, 1998.

[99] A. Barty, *Quantitative Phase-Amplitude Microscopy*. PhD thesis, University of Melbourne, Parkville, Victoria, Australia, Feb. 2000.

[100] E. W. Hansen and P. L. Law, "Recursive methods for computing the Abel transform and its inverse," *J. Opt. Soc. Am. A*, vol. 2, pp. 510–520, Apr. 1985.

[101] C. J. Cremers and R. C. Birkebak, "Application of the Abel integral equation to spectrographic data," *Appl. Opt.*, vol. 5, pp. 1057–1064, June 1966.

[102] C. K. Chan and P. Lu, "On the stability of the solution of Abel's integral equation," *J. Phys. A: Math. Gen.*, vol. 14, pp. 575–578, Mar. 1981.

[103] M. Deutsch and I. Beniaminy, "Derivative-free inversion of Abel's integral equation," *Appl. Phys. Lett.*, vol. 41, pp. 27–28, July 1, 1982.

[104] R. S. Anderssen and F. R. de Hoog, "On the method of Chan and Lu for Abel's integral equation," *J. Phys. A: Math. Gen.*, vol. 14, pp. 3117–3121, Nov. 1981.

[105] K. Tatekura, "Determination of the index profile of optical fibers from transverse interferograms using Fourier theory," *Appl. Opt.*, vol. 22, pp. 460–463, Feb. 1, 1983.

[106] M. Kalal and K. A. Nugent, "Abel inversion using fast Fourier transforms," *Appl. Opt.*, vol. 27, pp. 1956–1959, May 15, 1988.

[107] P. A. Vicharelli and W. P. Lapatovich, "Iterative method for computing the inverse Abel transform," *Appl. Phys. Lett.*, vol. 50, pp. 557–559, Mar. 9, 1987.

[108] A. Roberts, E. Ampem-Lassen, A. Barty, K. A. Nugent, G. W. Baxter, N. M. Dragomir, and S. T. Huntington, "Refractive-index profiling of optical fibers with axial symmetry by use of quantitative phase microscopy," *Opt. Lett.*, vol. 27, pp. 2061–2063, Dec. 1, 2002.

[109] P.-E. Dupouy, M. Buchner, P. Paquier, G. Trenec, and J. Vigue, "Interferometric measurement of the temperature dependence of an index of refraction: Application to fused silica," *Appl. Opt.*, vol. 49, pp. 678–682, Feb. 1, 2010.

[110] D. Paganin, A. Barty, P. J. McMahon, and K. A. Nugent, "Quantitative phase-amplitude microscopy. III. The effects of noise," *J. Microsc.*, vol. 214, pp. 51–61, Apr. 2004.

[111] B. L. Bachim and T. K. Gaylord, "Automated flexure testing of axially rotated optical fiber gratings," *Rev. Sci. Instrum.*, vol. 73, pp. 3454–3457, Oct. 2002.

[112] Y. Park, U.-C. Paek, S. Han, B.-H. Kim, C.-S. Kim, and D. Y. Kim, "Inelastic frozen-in stress in optical fibers," *Opt. Commun.*, vol. 242, pp. 431–436, Dec. 8, 2004.

[113] B. H. Kim, Y. Park, D. Y. Kim, U. C. Paek, and W. T. Han, "Observation and analysis of residual stress development resulting from OH impurity in optical fibers," *Opt. Lett.*, vol. 27, pp. 806–808, May 15, 2002.

[114] W. Primak and D. Post, "Photoelastic constants of vitreous silica and its elastic coefficient of refractive index," *J. Appl. Phys.*, vol. 30, pp. 779–788, May 1959.

[115] Y.-J. Chang and T. K. Gaylord, "Birefringence characteristics of nanoscale dielectrics with cubic and tetragonal lattices," *Opt. Express*, vol. 18, pp. 809–821, Jan. 18, 2010.

[116] A. D. Yablon, M. F. Yan, P. Wisk, F. V. DiMarcello, J. W. Fleming, W. A. Reed, E. M. Monberg, D. J. DiGiovanni, J. Jasapara, and M. E. Lines, "Refractive index perturbations in optical fibers resulting from frozen-in viscoelasticity," *Appl. Phys. Lett.*, vol. 84, pp. 19–21, Jan. 5, 2004.

[117] F. Durr, H. G. Limberger, R. P. Salathe, and A. D. Yablon, "Inelastic strain birefringence in optical fibers," in *Optical Fiber Communications Conference*, Anaheim, CA, OWA2, Mar. 8, 2006.

[118] S. Yamasaki, M. Akiyama, K. Nishide, A. Wada, and R. Yamauchi, "Characteristics of long-period fiber grating utilizing periodic stress relaxation," *IEICE Trans. Electron.*, vol. E83-C, pp. 440–443, Mar. 2000.

[119] C.-S. Kim, Y. Han, B. H. Lee, W.-T. Han, U.-C. Paek, and Y. Chung, "Induction of the refractive index change in B-doped optical fibers through relaxation of the mechanical stress," *Opt. Commun.*, vol. 185, pp. 337–342, Nov. 15, 2000.

[120] Iatia Limited, Victoria, Australia, *QPI Software Development Kit Documentation*, 2007.

[121] N. M. Dragomir, *Microscopic Characterization of Photonic Devices*. PhD thesis, Victoria University of Technology, Victoria, Australia, 2004.

[122] F. Mitschke, *Fiber Optics: Physics and Technology*. Berlin: Springer, 2009.

[123] L. Drozin, P. Y. Fonjallaz, and L. Stensland, "Long-period fibre gratings written by CO_2 exposure of H_2-loaded, standard fibres," *Electron. Lett.*, vol. 36, pp. 742–744, Apr. 13, 2000.

[124] P. Helander, "Measurement of fictive temperature of silica glass optical fibers," *J. Mater. Sci.*, vol. 39, pp. 3799–3800, 2004.

[125] L. Rongved, C. R. Kurjian, and F. T. Geyling, "Mechanical tempering of optical fibers," *J. Non-Cryst. Solids*, vol. 42, pp. 579–584, 1980.

[126] A. K. Varshneya, D. Varshneya, and V. Jain, "On 'mechanical tempering of optical fibers'," *J. Non-Cryst. Solids*, vol. 93, pp. 215–216, 1987.

[127] E. Anemogiannis, E. N. Glytsis, and T. K. Gaylord, "Transmission characteristics of long-period fiber gratings having arbitrary azimuthal/radial refractive index variations," *J. Lightwave Technol.*, vol. 21, pp. 218–227, Jan. 2003.

[128] H. Hochreiner, M. Cada, and P. D. Wentzell, "Modeling the response of a long-period fiber grating to ambient refractive index change in chemical sensing applications," *J. Lightwave Technol.*, vol. 26, pp. 1986–1992, July 2008.

[129] PI (Physik Instrumente) L.P., Auburn, Massachusetts.

[130] E. D. Barone-Nugent, A. Barty, and K. A. Nugent, "Quantitative phase-amplitude microscopy I: Optical microscopy," *J. Microsc.*, vol. 206, pp. 194–203, June 2002.

[131] D. D. Davis, *Long-Period Fiber Gratings Fabricated with Focused CO_2 Laser Pulses*. PhD Thesis, Georgia Institute of Technology, Atlanta, GA, May 1999.

[132] T. Hayashi, T. Taru, O. Shimakawa, T. Sasaki, and E. Sasaoka, "Design and fabrication of ultra-low crosstalk and low-loss multi-core fiber," *Opt. Express*, vol. 19, pp. 16576–16592, Aug. 15, 2011.

[133] X.-H. Fang, M.-L. Hu, B.-W. Liu, L. Chai, C.-Y. Wang, and A. M. Zheltikov, "Generation of 150 MW, 110 fs pulses by phase-locked amplification in multicore photonic crystal fiber," *Opt. Lett.*, vol. 35, pp. 2326–2328, July 15, 2010.

[134] J. Wang, X. Yang, and L. Wang, "Fabrication and experimental observation of monolithic multi-air-core fiber array for image transmission," *Opt. Express*, vol. 16, pp. 7703–7708, May 26, 2008.

[135] G. A. Miller, C. G. Askins, and G. A. Cranch, "Interferometric interrogation of a multicore fiber, two-axis inclinometer," *Proc. SPIE*, vol. 7503, pp. 75032R-1–75032R-4, 2009.

[136] A. Fender, W. N. MacPherson, R. R. J. Maier, J. S. Barton, D. S. George, R. I. Howden, G. W. Smith, B. J. S. Jones, S. McCulloch, X. Chen, R. Suo, L. Zhang, and I. Bennion, "Two-axis temperature-insensitive accelerometer based on multicore fiber Bragg gratings," *IEEE Sensors J.*, vol. 8, pp. 1292–1298, July 2008.

[137] A. Fender, E. J. Rigg, R. R. J. Maier, W. N. MacPherson, J. S. Barton, A. J. Moore, J. D. C. Jones, D. Zhao, L. Zhang, I. Bennion, S. McCulloch, and B. J. S. Jones, "Dynamic two-axis curvature measurement using multicore fiber Bragg gratings interrogated by arrayed waveguide gratings," *Appl. Opt.*, vol. 45, pp. 9041–9048, Dec. 20, 2006.

[138] R. C. Jorgenson and S. S. Yee, "A fiber-optic chemical sensor based on surface plasmon resonance," *Sens. Actuators, B*, vol. 12, pp. 213–220, Apr. 1993.

[139] R. C. Jorgenson and S. S. Yee, "Control of the dynamic range and sensitivity of a surface plasmon resonance based fiber optic sensor," *Sens. Actuators, A*, vol. 43, pp. 44–48, May 1994.

[140] L. L. Obando and K. S. Booksh, "Tuning dynamic range and sensitivity of white-light, multimode, fiber-optic surface plasmon resonance sensors," *Anal. Chem.*, vol. 71, pp. 5116–5122, Nov. 1999.

[141] A. D. Kersey, M. A. Davis, H. J. Patrick, M. LeBlanc, K. P. Koo, C. G. Askins, M. A. Putnam, and E. J. Friebele, "Fiber grating sensors," *J. Lightwave Technol.*, vol. 15, pp. 1442–1463, Aug. 1997.

[142] B. H. Lee and J. Nishii, "Self-interference of long-period fibre grating and its application as temperature sensor," *Electron. Lett.*, vol. 34, pp. 2059–2060, Oct. 15, 1998.

[143] P. L. Swart, "Long-period grating Michelson refractometric sensor," *Meas. Sci. Technol.*, vol. 15, pp. 1576–1580, Aug 2004.

[144] M. Jiang, A. P. Zhang, Y.-C. Wang, H.-Y. Tam, and S. He, "Fabrication of a compact reflective long-period grating sensor with a cladding-mode-selective fiber end-face mirror," *Opt. Express*, vol. 17, pp. 17976–17982, Sept. 28, 2009.

[145] L. Yuan, J. Yang, Z. Liu, and J. Sun, "In-fiber integrated Michelson interferometer," *Opt. Lett.*, vol. 31, pp. 2692–2694, Sept. 15, 2006.

[146] O. Frazo, P. Caldas, F. M. Arajo, L. A. Ferreira, and J. L. Santos, "Optical flowmeter using a modal interferometer based on a single nonadiabatic fiber taper," *Opt. Lett.*, vol. 32, pp. 1974–1976, July 15, 2007.

[147] Z. B. Tian, S. S. H. Yam, and H. P. Loock, "Single-mode fiber refractive index sensor based on core-offset attenuators," *IEEE Photon. Technol. Lett.*, vol. 20, pp. 1387–1389, Aug. 15, 2008.

[148] T. Yoshino, K. Kurosawa, K. Itoh, and T. Ose, "Fiber-optic Fabry-Perot interferometer and its sensor applications," *IEEE J. Quantum Electron.*, vol. 18, pp. 1624–1633, Oct. 1982.

[149] O. Esteban, N. Diaz-Herrera, M. C. Navarrete, and A. Gonzalez-Cano, "Surface plasmon resonance sensors based on uniform-waist tapered fibers in a reflective configuration," *Appl. Opt.*, vol. 45, pp. 7294–7298, Oct. 1, 2006.

[150] S. Ishihara, Y. Mitsuhashi, M. Tagawa, and H. Yamazaki, "Simple fabrication of an optical fiber mirror," *Appl. Opt.*, vol. 25, pp. 3982–3983, Nov. 15, 1986.

VITA

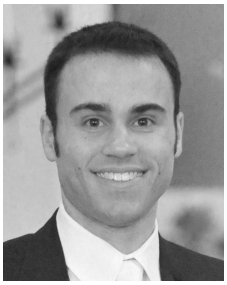

Michael R. Hutsel was born in 1982 in St. Louis, Missouri. Prior to attending the Georgia Institute of Technology, he received his Bachelor of Science in Electrical Engineering from the University of Missouri-Columbia in 2004. While at Georgia Tech, Mike was the recipient of the Presidents Fellowship and the Center for Organic Photonics and Electronics Fellowship. He is a member of the Optical Society of America, the Institute of Electrical and Electronic Engineers, and Eta Kappa Nu.

In 2008 Mike was challenged to read the book of John in God's Word, the Bible. God revealed to Mike from His Word that because of his sin, his thoughts and actions that left God out of his life, he was separated from God. God further revealed to Mike that there was nothing he could do to fix this, no matter how good he thought he was. He revealed to Mike that it is only through the life and death and resurrection of Jesus Christ that he can be free from sin and have the guarantee of everlasting life with God. Because of God's revelation from His Word, Mike put his faith in Jesus Christ for the forgiveness of his sin and everlasting life.

> *but these* [accounts in the book of John] *are written so that you may believe that Jesus is the Christ, the Son of God, and that by believing you may have life in his name.*
>
> – John 20:31 (ESV)